**Max-Planck-Institut für Metallforschung**
Stuttgart

# Reinforcement of precursor-derived Si-(B-)C-N ceramics with carbon nanotubes

Yuji Katsuda

Dissertation
an der
**Universität Stuttgart**

**Bericht Nr. 177**
**2005**

# Reinforcement of precursor-derived Si-(B-)C-N ceramics with carbon nanotubes

Dissertation

Von der Fakultät Chemie der Universität Stuttgart
zur Erlangung der Würde eines
Doktors der Naturwissenschaften (Dr. rer. nat.)
genehmigte Abhandlung

**Vorgelegt von**

**Yuji Katsuda**

**Aus Japan**

| | |
|---|---|
| Hauptberichter: | Prof. Dr. rer. nat. Fritz Aldinger |
| Mitberichter: | Prof. Dr. rer. nat. Dr. hc. mult. Günter Petzow |
| Prufungsvorsitzender: | Prof. Dr. Ir. Eric J. Mittemeijer |
| Tag der mündlichen Prüfung: | 20.12.2005 |

Institut für Nichtmetallische Anorganische Materialien der Universität Stuttgart
Max-Planck-Institut für Metallforschung, Stuttgart
Pulvermetallurgisches Laboratorium

Stuttgart 2005

**Acknowledgement**

This Ph. D. work has been carried out from August 2002 to October 2005 in the Max-Planck-Institute for Metals Research, Stuttgart and University of Stuttgart.

I would like to thank Prof. Dr. F. Aldinger for providing me this opportunity to carry out the Ph. D. work at his department. I also gratefully acknowledge him for teaching, management and encouragement to accomplish my research work.

I am grateful to Prof. Dr. G. Petzow for his kindness and being the "Mitberichter" (co-examiner) for my thesis.

I appreciate Prof. Dr. E. J. Mittemeijer, who kindly agreed to become the "Mitprüfer" for my examination.

I wish to thank Prof. Dr. R. Danzer (University of Leoben, Austria) for discussing mechanical results of this research and reviewing the part of this thesis.

I appreciate Prof. Dr. R. Raj (University of Colorado, USA) for helpful advice on the material preparation process.

My special thanks to my supervisor Dr. J. Bill, who kindly arranged the research issues and thoroughly discussed experimental results, plans and writing with me. His suggestions and leading were very helpful for me both on the research work and daily life in Stuttgart.

I highly thank Mr. P. Gerstel for his technical supports and many instructions on the material preparation and characterization.

There are many other people in MPI-PML who kindly helped, taught and supported me. Mr. J. Narayanan introduced the techniques of casting and the calculations of fracture toughness to me. Mr. R. Mager taught me the thermal loading technique very carefully and also helped to machine samples. Dr. Z. Burghard helped to examine nanoindentation profiles closely. Mr. H. Kummer helped to do TG and

dilatometer investigations. Mr. G. Kaiser and his colleagues helped to do chemical analysis. Ms. M. Thomas helped to do XRD analysis. Mr. H. Labitzke helped to do SEM observation. Mr. H. Eckstein and his colleagues helped to provide experimental tools for material preparation with full smile.
I would like to thank other colleagues in PML for their assistance and cooperation.

Thanks are also offered to Ms. S. Kühnemann and Ms. M. Kelsch, both in Prof. Rühle department, for their technical supports with the microscopic analyses by SEM and TEM.

I am grateful to NGK INSULATORS, LTD and my bosses for providing me this special opportunity with financial supports.

Finally, I wish to express my thanks to my wife, daughters, parents and parents-in-law for their encouragement. Especially I thank my wife for her efforts to make a life in Stuttgart pleasant.

Thank you very much!

Yuji Katsuda
Stuttgart, October 2005

**Abstract**

Incorporation of carbon nanotubes (CNTs) into the precursor-derived Si-(B-)C-N ceramics has been investigated for the reinforcement of the materials. Different types of CNTs consisting of multi-wall (MW) and single-wall (SW) were examined as the reinforcement of the Si-(B-)C-N ceramics to make a comparison of the effect. Mechanical properties demonstrated in the Si-(B-)C-N/CNT nanocomposites have been discussed in connection with their microstructural features characterized by scanning electron (SEM) and transmission electron microscope (TEM). Other material properties of the nanocomposites as revealed on the thermal stability and the crystallization behavior have been also considered in relation to the microstructural characteristics of the nanocomposites.

Dense Si-C-N/CNT nanocomposites containing different types of MWCNTs were successfully prepared by casting of a mixture of MWCNTs and a liquid precursor polymer followed by cross-linking and thermolysis. In these processes, the sonication for deagglomeration and dispersion of CNTs in the precursor polymer as well as the thermolysis condition for ceramization of the cross-linked precursor/CNT nanocomposites was examined to obtain homogeneously CNT distributed Si-C-N ceramics. Fracture toughness behavior of the Si-C-N/CNT nanocomposites has been evaluated by a thermal loading technique on the disc shaped materials. The results reveal a dependence of the fracture toughness on the type of the MWCNTs. The MWCNTs showing high integrity in the tube structure exhibit a remarkable increase in the fracture toughness at the CNT content of 1 – 2 mass %, whereas the other ones possessing amorphous nature exhibits no effect. The microstructural analyses at the fracture surfaces have demonstrated different features of CNTs between both nanocomposites, where pulling out and breaking of CNTs are considered to be reasons for the observed fracture toughness increase. No significant influences observed on the material properties of the Si-C-N/CNT nanocomposites besides the toughening indicates that CNTs can simply work as the reinforcement for the Si-C-N ceramics.

SWCNTs incorporation into the Si-C-N materials has revealed toughening effect with similar microstructural features to the MWCNT reinforced Si-C-N nanocomposites. In this system, it was found that the deagglomeration and debundle

of the SWCNTs are major issues to make the best use of SWCNTs as the reinforcements.

Concerning the Si-B-C-N/CNT nanocomposites, preparation processes via a casting and a warm pressing from different types of boron-containing precursors have been investigated to produce rigid MWCNT nanocomposites. The observed pulling out and breaking CNTs structure at the fracture surfaces of the Si-B-C-N/CNT nanocomposites indicate the toughening effect of CNTs similar to Si-C-N/CNT ceramics. Moreover, the interaction between CNTs and the matrix has appeared to be changed with increasing thermolysis temperature. However, the crystallization of the Si-B-C-N matrix and the deterioration of thermal stability have been disclosed in the Si-B-C-N/CNT nanocomposites. It is revealed that embedded CNTs have an effect to accelerate or to generate nucleation sites for the crystallization of Si-B-C-N matrix.

**Contents**

Acknoledgement..... 1
Abstract..... 3
Contents..... 5
List of symbols and abbreviations..... 7

1 Introduction..... 9

2 Literature review..... 11
2.1 Precursor-derived Si-(B-)C-N ceramics..... 11
2.2 Carbon nanotubes..... 15
2.3 Carbon nanotubes incorporated composite materials..... 17

3 Experimental..... 21
3.1 General comments for sample preparation..... 21
3.2 Characterization..... 21
3.2.1 Bulk density, thermal expansion and elastic properties..... 21
3.2.2 Thermal stability and X-ray diffraction analysis..... 22
3.2.3 Chemical analysis..... 22
3.2.4 Fracture toughness..... 22
3.2.5 Nano indentation..... 27
3.2.6 Microstructural analysis..... 27

4 Results and discussion..... 28
4.1 Characterization of carbon nanotubes..... 28
4.2 Si-C-N/MWCNT nanocomposites..... 31
4.2.1 Sample preparation..... 31
4.2.2 General materials properties..... 37
4.2.3 Thermal stability and chemical analysis..... 41
4.2.4 Fracture toughness behavior..... 43
4.2.5 Microstructural analysis..... 50

4.3 Si-C-N/SWCNT nanocomposites..... 55
4.3.1 Sample preparation..... 55
4.3.2 Fracture toughness behavior..... 55
4.3.3 Microstructural analysis..... 56
4.4 Si-B-C-N/MWCNT nanocomposites..... 58
4.4.1 Sample preparation..... 58
4.4.2 Crystallization behavior..... 62
4.4.3 Thermal stability and chemical analysis..... 63
4.4.4 Microstructural analysis of embedded CNTs by TEM..... 65
4.4.5 Fracture toughness behavior..... 68
4.4.6 Microstructural analysis..... 70
4.4.7 Young's modulus and hardness..... 74

5 Summary and conclusions..... 79

Appendix..... 80
References..... 86
Zusammenfassung..... 95

Curriculum Vitae

## List of symbols and abbreviations

| | |
|---|---|
| $a$ | crack length coordinate |
| $c$ | critical crack length |
| $c_0$, $c_2$, $c_4$ | time-dependent fitting parameters for the temperature distribution |
| $D_0$, $D_1$, $D_2$ | coefficients for the weight function |
| $E$ | Young's modulus |
| $h$, $i$, $j$ | fitting coefficient for length-temperature curve |
| $K_I$, $K_{IC}$ | stress intensity factor, fracture toughness |
| $l$ | length |
| $r$ | radial distance |
| $R$ | radius of the disc sample |
| $T$ | temperature |
| $t$, $t_c$ | time, time at $a=c$ |
| $V$ | voltage |
| $x$ | coordinate from the edge |
| $\alpha$ | thermal expansion coefficient |
| $\beta$ | $\beta=a/2R$ |
| $\nu$ | Poisson's ratio |
| $\rho$ | $\rho=x/a$ |
| $\sigma(x)$ | stress distribution |
| $\sigma^*$ | characteristic stress value |

| | |
|---|---|
| AD-DA | analog digital-digital analog |
| AFM | atomic force electron microscope |
| CCD | charge coupled device |
| CNT, CNTs | carbon nanotube, carbon nanotubes |
| CVD | chemical vapor deposition |
| MEMS | microelectromechanical device |
| MW | multi-wall |
| OM | optical microscope |
| OVS | oligo-vinylsilazane |
| SEM | scanning electron microscope |
| SPM | scanning probe microscope |

| | |
|---|---|
| SPS | spark plasma sintering |
| SW | single-wall |
| T2-1 | boron containing polysilazane (polyorganoborosilazane) |
| TCP | boron containing polysilazane (TMEB-ethyl-polysilazane) |
| TEM | transmission electron microscope |
| THF | tetrahydrofuran |
| TMBE | tris(methylsilylethyl)borane |
| XRD | X-ray diffraction |

## 1. Introduction

Non-oxide ceramics such as silicon nitride, silicon carbide, boron nitride and their composite materials have a great potential for the use as structural materials especially in the field of high temperature application because of their high mechanical strength and hardness, high thermal and chemical stability as well as low density characteristic [96Nar, 00Ril, 02Pet, 04Kus]. Synthesis of these ceramics is usually performed by powder technology involving powder preparation, powder compact formation and following densification. The densification of the powder compact is achieved by sintering where high temperatures and suitable gas atmospheres as well as sintering additives are generally required due to the low self-diffusion nature of such covalent bonded ceramics. The sintering additives usually induce oxide-based secondary phases in the materials, which can enhance the atomic mobility leading to the densification. However, these secondary phases possess less stability at high temperature than the non-oxide ceramics causing the degradation of their performance mechanically, thermally and chemically.

Precursor polymers and their techniques open up alternative routes to produce covalent ceramics, so-called precursor-derived ceramics [90Peu, 95Bil, 95Bir]. These processes involve the cross-linking of organometallic compounds and following thermolysis, where the networks of organometallic compounds are directly transformed into covalent bonded ceramics by heat treatment. The technology of precursor-derived ceramic has several advantages compared to the conventional powder technology that concerns the material properties and processing issues. For example, the atomic structure and microstructure of the ceramics can be designed to some extent by the molecular composition of the starting precursor polymers which can be then transformed into high purity covalent bonded ceramics without any sintering additives. In addition, the ceramic bodies attain the homogeneous chemical distribution on an atomic scale. Concerning the processing, the relatively low temperature for ceramization provides the low cost ceramic production. In addition, their unique polymer-ceramic transformation by heat treatment can provide a means to form ceramic bodies into near-net shapes, small scales or complex forms from cross-linked polymer bodies.

Si-C-N and Si-B-C-N materials are representative precursor-derived non-oxide ceramics which possess structural stability at high temperatures [00Kro, 01Bil, 02Jan]. However, these ceramics exhibit mechanically brittle nature due to their amorphous or nanosized crystalline microstructure. The incorporation of toughening agents to form composites is an approach to reinforce the brittle ceramics [98Cha]. In this architecture, fibers are the most desirable form of the toughening agents, since the fibers can increase the fracture energy of the composites by inducing fiber pulling out and bridging, interface debonding, crack deflection and pinning effects during fracturing of the composite materials. These microstructural effects result in an increase of the fracture toughness. From this point of view, carbon nanotubes (CNTs) are considered to be promising toughening agents for Si-(B-)C-N ceramics owing to their extremely high mechanical strength, nanometer sizes with high aspect ratio (length to diameter) as well as their high thermal stability natures.

The objectives of this thesis are to incorporate CNTs into the precursor-derived Si-C-N and Si-B-C-N ceramics, and to investigate the effect of CNTs on the fracture toughness behavior of the nanocomposites as well as on the thermal and microstructural behaviors. Different types of CNTs consisting of the multi-wall (MW) and single-wall (SW) were examined for making a comparison of the reinforcement effect. The results of mechanical behavior are mainly discussed in connection with their microstructural features characterized by scanning electron (SEM), transmission electron (TEM), and atomic force electron microscopy (AFM). Other material properties such as density, Young's modulus, thermal expansion, chemical composition, thermal stability and the crystalline behavior were also characterized and discussed.

# 2 Literature review

## 2.1 Precursor-derived Si-(B-)C-N ceramics

Precursor polymers, which can transform their organic units into inorganic ceramics, are very unique and ideal materials for the synthesis and design of advanced non-oxide ceramics as well as their processing. The pioneer works of this field date back to the 1960s to 1970s by Popper [67Pop], Veerbeck [73Vee] and Yajima [75Yaj] et al., where the preparation of silicon nitride- and silicon carbide-based ceramics via thermolysis of polymers has been reported. Thereafter, the material science and engineering of precursor-derived ceramics have been spread out on the trend of application of silicon nitride or silicon carbide based ceramics to the high temperature structural materials.

Fig. 2.1 describes a flow chart for the standard preparation process of precursor-derived ceramics [95Bil]. First, precursor polymers or oligomers are synthesized from monomer units. The precursors are then cross-linked in order to form organometallic pre-ceramic networks in two or three dimensions. The organometallic networks are transformed into amorphous covalent ceramics by heat

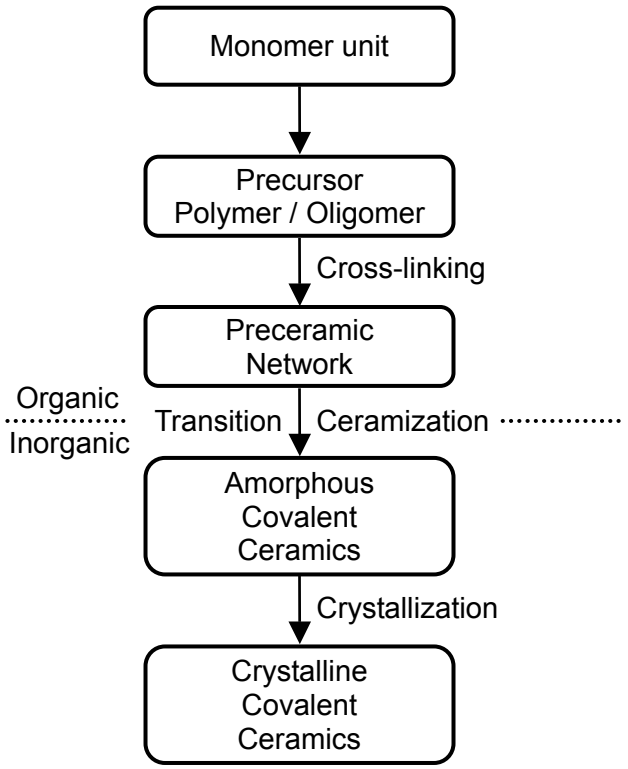


Fig. 2.1. A flow chart for the preparation of precursor-derived ceramics [95Bil].

treatment (organic/inorganic transition). Additionally, the amorphous ceramics can be crystallized by further heat treatment at high temperature.

Fig. 2.2 summarizes the representative precursor polymers for the preparation of silicon nitride- and silicon carbide-based ceramics [95Bil]. It can be seen in the diagram that the precursors possess silicon, nitrogen and carbon containing monomer units in their organic structures. Additionally, other elements such as B, Al, Ti or P can be induced in the precursors by modifying their functional groups.

Ternary Si-C-N ceramics are generally synthesized by the thermolysis of polysilazanes. These precursor polymers possess alternating silicon and nitrogen atom sequence in the backbone. The most popular precursor in this type is poly(ureamethylvinyl)silazane, Ceraset™, which is commercially produced by KiON, USA [KiON]. The chemical structure of Ceraset™ in Fig. 2.3 describes the cyclic sequence of silicon and nitrogen bonding with urea and vinyl functionality. According to the study by Li at al. [01Li], the cross-linking solidification of Ceraset™ takes place around 250 °C by hydrosilylation of vinyl groups followed by a transamination reaction between 280 and 400 °C. During the subsequent ceramization step, the major thermolysis reaction involves dehydrogeneration betweeen Si-H and N-H groups, and condensation of Si-$CH_3$ and N-H groups around 600 - 800 °C. These

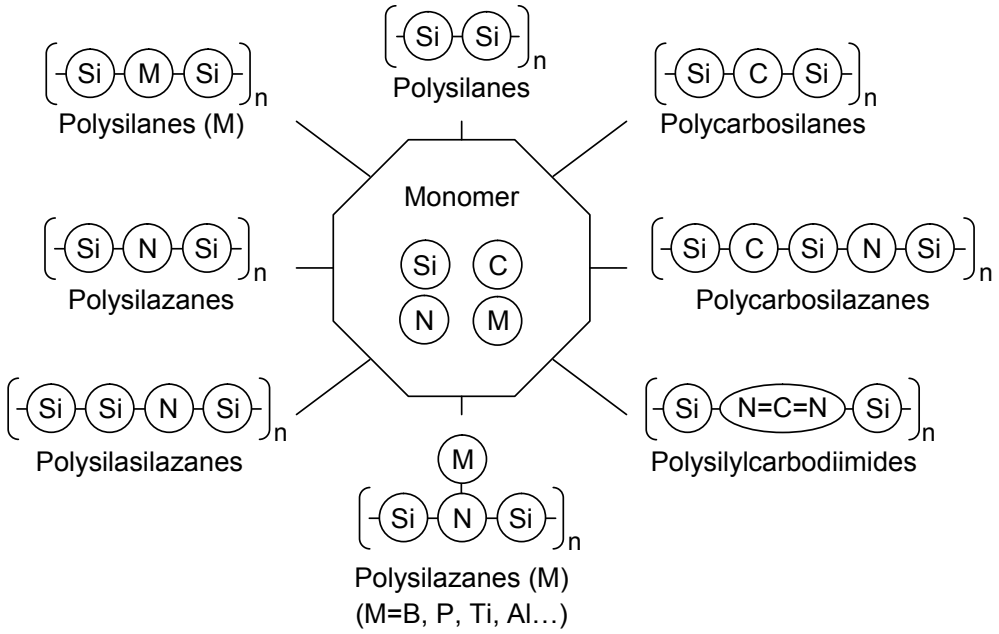


Fig. 2.2. Formation of organosilicon polymers from monomer units [95Bil].

reactions yield an amorphous Si-C-N ceramic accompanied by the formation of the gaseous by-products of hydrogen and methane. Further heat treatment at high temperature induces the Si-C-N ceramics to crystallize into nanosized silicon carbide and silicon nitride [04Schm].

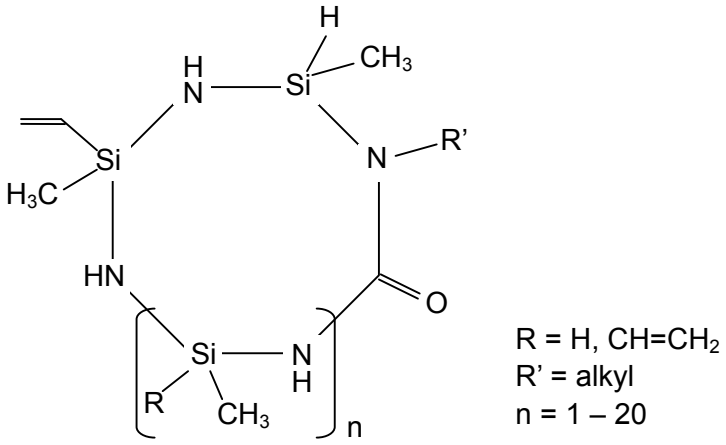


Fig. 2.3. Chemical structure of the poly(ureamethylvinyl)silazane, Ceraset$^{TM}$ [KiON].

Quaternary Si-B-C-N ceramics can be produced by boron-containing polysilazane polymers. These polymers are prepared via chemical modification of silicon-containing polymers or oligomers with boron-containing compounds, or synthesis of polymers with boron-containing monomer units [01Bil]. Fig. 2.4 and 2.5 show two routes for the synthesis of boron containing polysilazanes called "T2-1" [96Rie] and "TCP" [98Kam, 00Wei]. Both precursors were used in this study. In the former route, hydroboration of a silane at the vinyl group and following ammonolysis provides the boron-containing polysilazane with Si-C-C-B-C and Si-C-B-C bridges in the structure (T2-1). In the latter case, hydrosilylation between vinylsilazane and tris(hydridosilylethyl)borane forms Si-C-C-Si-C-B and Si-C-Si-C-B bridges in the polysilazane (TCP). The TCP precursor is very distinctive because it has no by-products during the synthetic reaction.

These precursor-derived Si-(B-)C-N ceramics exhibit excellent structural stability at high temperatures as revealed on the thermogravimetric behavior [96Rie, 00Wei, 01Bil], creep resistance [99Thu, 01Sha, 02Zim, 04Kum] and oxidation resistance [95Rie, 01But, 01Raj1, 04Bha]. Especially, Si-B-C-N ceramics possess an excellent thermal stability up to 2000 °C. These characteristics are principally due to

their covalent bonding nature and high purity. Furthermore, the liquid nature of precursors enables coating, infiltrating and casting for material processing in adittion to the conventional powder techniques. From these advantages, precursor-derived Si-C-N and Si-B-C-N ceramics are considered structural marterials for high temperature applications not only as monolythic bodies but also as coatings [96Bil], secondary phases [99Zie, 00Wei] and fiber reinforcements [99Bal] for composites. Recently, Raj et al reported the application of precursor technology to the fabrication of microelectromechanical devices (MEMS technologies), where a photopolymerization technique of Si-C-N precursor and a photolithographical patterning technique were combined to produce micro devices via a casting process [01Raj2, 02Lie, 03Lie]. They proposed several Si-C-N MEMS devices as an electrostatic actuator, a pressure sensor, a combustion chamber, a micro glow plug and other.

However, a main drawback of precursor-derived ceramics is their brittle nature leading to a deterioration of their mechanical properties.

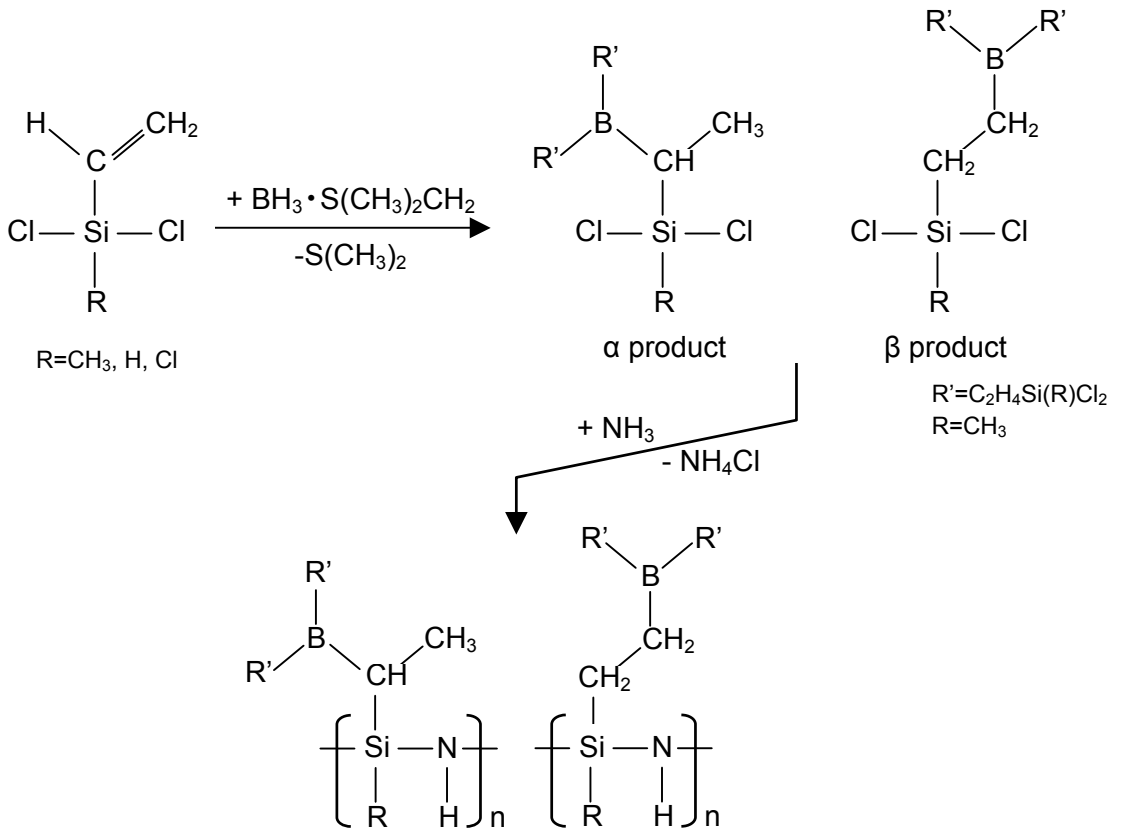


Fig. 2.4. Synthesis route for boron containing polysilazane, T2-1 [96Rie, 01Bil].

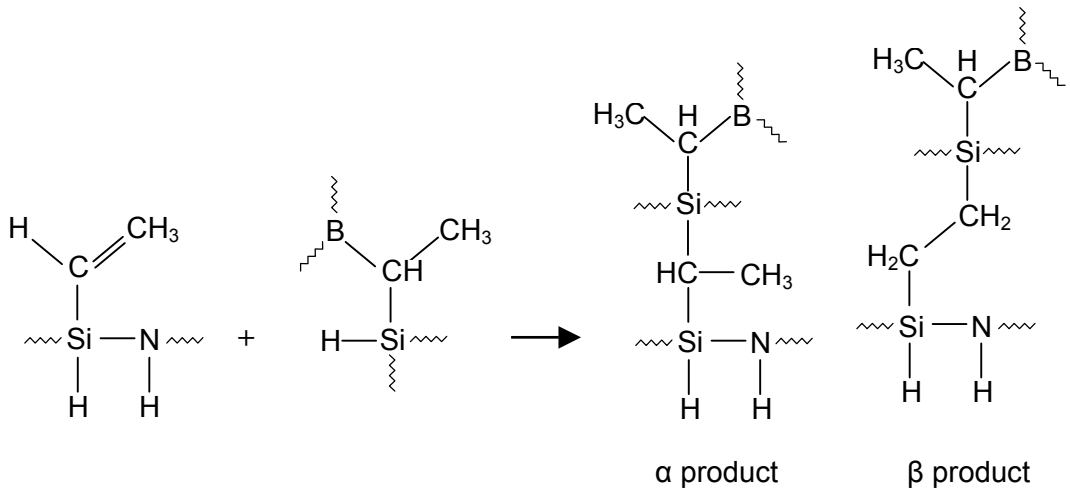


Fig. 2.5. Synthesis route for boron containing polysilazane, TCP [98Kam, 00Wei].

## 2.2 Carbon nanotubes

Carbon nanotubes (CNTs), which were discovered in 1991 by Iijima [91Iij], are seamless hollow cylinders composed of well ordered $sp^2$-graphene sheets either in form of single-walled (SW) or multi-walled (MW) configurations (Fig. 2.6 [Sma, Roc]). The dimensions of CNTs are nano scales with a high aspect ratio from the lengths of several hundred nanometers to several microns and diameters of 0.4 – 2 nm for SWCNTs and 2 – 100 nm for MWCNTs [Dre]. These CNTs can be produced by arc discharge [91iij], laser ablation [96The] or chemical vapor deposition processes [93Yac].

Much research work has been dedicated to the understanding of CNTs revealing their extraordinary characteristics in electrical, mechanical, and thermal properties as well as their unique structures. For example, SWCNTs exhibit metallic- or semi-conduction depending on their graphene rolling up directions (helicity) [92Min, 92Ham, 92Sai]. Thess et al. have measured an electrical resistivity of $< 10^{-4}$ ohm-cm at 300 K for metallic SWCNTs [96The]. Both metallic and nonmetallic properties are also observed for MWCNTs [95Deh, 05Sun]. Concerning mechanical properties, several studies have described extraordinary high Young's modulus of above 1 TPa for both SWCNTs [98Kri, 98Lou, 00Yu1] and MWCNTs [96Tre, 98Lou]. Also, tensile strength of around 30 GPa [00Yu1] or more [98Wag, 00Yu2] has been

reported. On their thermal properties, experimental results and theoretical calculations reveal that the thermal conductivity is between 1800 and 6600 W/mK at room temperature [99Hon, 99Yi, 00Ber], which is rather higher than that of diamond (~ 2000 W/mK).

Concerning the industrial applications, CNTs are expected to be used in mainly four fields due to their superior properties. 1st, CNTs are suitable as electron field emitters for microscopic probes [02Jon] or field emission displays [99Cho] because of their nanometer-sized needle like shape, high electrical conductivity, high chemical and thermal stability. 2nd, electron devices for nanometer-sized transistors, diodes and logic circuits are considered [01Bac, 04Gra]. These are expected to replace silicon device technologies in future. 3rd, the use of electrochemical function such as supercapacitors for energy storage [03Emm], hydrogen storage for fuel cell [97Dil] and various sensors [00Kon, 03Qi] is proposed. 4th, CNT incorporated composite materials are widely investigated to improve or induce structural, electrical and/or thermal functions. The last application fields are introduced in the next section.

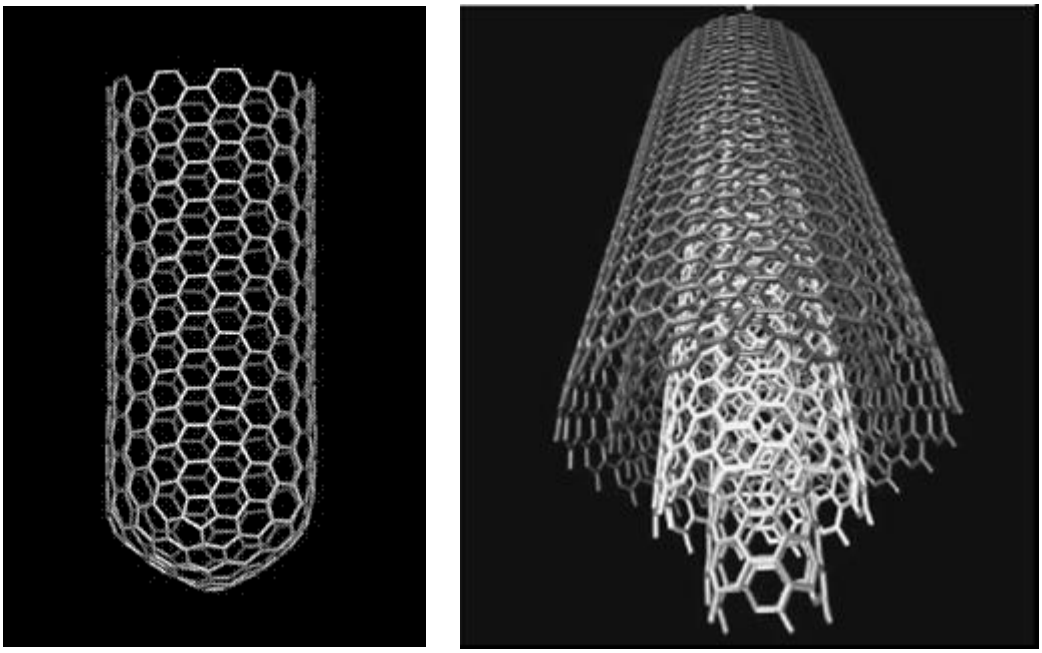

(a) (b)

Fig. 2.6. Schematic structure of carbon nanotubes, (a) Single wall CNT and (b) Multi wall CNT [Sma, Roc].

## 2.3 Carbon nanotubes incorporated composite materials

There are mainly three fields for CNTs for their use in nanocomposite materials. The first is the mechanical reinforcement of matrix by CNTs because of their high strength. The second is the improvement of thermal conductivity by introducing high thermal conductive CNTs. The third is the introduction of electrical conduction by the percolation of CNTs in the matrix. In these applications, a low weight nature of CNTs as well as their high aspect ratio provides further advantages for their use as filler materials. So far CNTs have been intensively applied for not only polymer-based composites but also metal and ceramic matrix systems.

In the case of polymer based CNTs nanocomposites, there exist two advantages for material processing. One is the dispersion of CNTs into the polymers, that is, liquid polymers can facilitate the deagglomeration and dispersion of CNTs greatly by sonication. The other advantage is the lower heat treatment temperature for the solidification of polymers, which prevents the CNTs from being structurally damaged during processing. In addition to these processing advantages, the big differences in their material properties between CNTs and polymers such as mechanical strength, thermal conductivity and electrical conductivity can provide large gain on their characteristics in polymer/CNT nanocomposites. Sandler et al. [99San, 03San] prepared epoxy/MWCNT composites by shear-intensive mechanical stirring of the mixture and following solidification by hardener at 140 °C for 8 h. They measured electrical conductivity of the epoxy/MWCNT composites by an AC impedance spectroscopy and observed the electrical percolation threshold to be below 0.005 wt % of CNT content with a conductivity increase of $10^6$ S/cm. Their comparative materials of epoxy/carbon black composites reveal the percolation threshold to be 1.0 wt %, which defines the effect of CNTs clear for electrical functionalization. Biercuk et al. [02Bie] and Choi et al. [03Cho] respectively described the increase of thermal conductivity by 125 % with 1 wt% SWCNTs and by 300 % with 3 wt% SWCNTs in the epoxy/SWCNTs nanocomposites compared to the pure epoxy material. Concerning mechanical properties, Gojny et al. [04Goj] investigated the fracture toughness behavior of similar composite and obtained the increase by ca. 25 % with the incorporation of 1 vol. % double-walled CNTs. Qian et al. also reported an improved mechanical strength and modulus of polyethylene with 1 wt% MWCNT incorporation [00Qia]. On the other side, Lau et al. [02Lau] observed enlarging holes at the interfaces between MWCNTs and the epoxy matrix during fracturing (Fig. 2.7).

In their composite materials, no benefit of CNTs on the mechanical performance was obtained because embedded CNTs were easily pulled out from the matrix. Consequently, they pointed out that the interfacial bonding between CNTs and the matrix is quite important and to be a critical issue for the mechanical reinforcement of the materials.

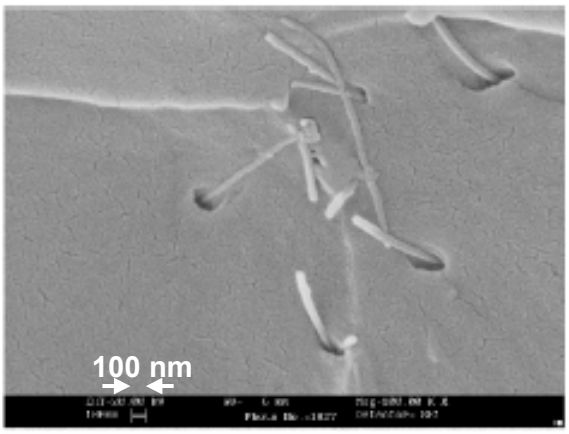


Fig. 2.7. SEM image of the fracture surface of epoxy/CNT composite containing 2 wt% MWCNTs [02Lau]. The holes at the interface reveal weak bonding of MWCNTs to the epoxy matrix.

Composites materials consisting of metal matrix with CNT fillers have been also investigated for the improvement of mechanical properties of metals. Kuzumaki et al. [98kuz] prepared Al/MWCNT (5 vol %) composites by hot-pressing and hot-extrusion methods at 500 – 600 °C from the powder mixtures. They observed the porosity in the consolidated nanocomposites as revealed by relative density of 94 %. However the composite revealed non-degradation nature on the tensile stress after annealing at 600 °C for 50 h, which can not be obtained in the pure aluminum or aluminum/carbon fiber composite materials. Their TEM study identified the suppression of the formation of carbide phase at the interface between aluminum and CNTs, which was the reason for the observed long term stability of the CNT incorporated aluminum composites. In another case, tribological application of copper-matrix CNT composites has been also proposed by Chen et al. [03Che]. They fabricated the composites by a powder metallurgy technique at 800 °C and obtained

the improved wear rates and friction coefficients with 12 vol % CNT incorporation. However, similar to the Al/MWCNT composites studied by Kuzumaki et al [98Kuz], the porosity increase with increasing the amount of CNTs was observed in the Cu/MWCNT composites. It is considered that the avoidance of pore formation in the metal/CNT composites is quite difficult issue for their preparation by the powder metallurgy technique.

Concerning ceramic materials, the incorporation of CNTs into the ceramics is also expected to induce or improve several functions [98Ma, 01Sie, 05Hua]. However, their conventional powder technological techniques including powder mixing and high temperature sintering might cause CNTs to lose their integrity which is necessary to fulfill their function in the matrix. That is, the material design of ceramic-matrix CNT composites is more challenging than that of polymer and metal systems. Zahn et al. [03Zah] adopted a spark plasma sintering (SPS) technique and nanosized alumina powders for the preparation of 5 – 10 vol % MWCNTs incorporated alumina composites. They obtained fully dense composites by SPS technique at 1150 °C for only 3 min. Their sintering condition is much softer than the other alumina sintering processes, which contributes CNTs for preserve their original nature during alumina densification. As a result, they achieved significantly high fracture toughness (9.7 $MPam^{1/2}$) in the alumina/CNT composites containing 10 vol % CNTs, which is three times as tough as their monolithic alumina material (3.3 $MPam^{1/2}$). A novel approach for the preparation of ceramic-matrix CNT nanocomposites has been made by Peigny et al [98Pei, 00Pei, 00Fla]. They have synthesized nanocomposite powders containing CNTs, metals and ceramic (metal: Fe, Co, Ni and their alloy, ceramic: $Al_2O_3$, $MgAl_2O_4$ and MgO) by an in situ catalysis method. In their processes, partially Fe, Co and/or Ni ion exchanged oxide powders were reduced in a $H_2$-$CH_4$ atmosphere at 1050 °C generating metal particles (Fe, Co and Ni) for the in situ nucleation and growth of CNTs on the oxide powders. The obtained composite powders possessed good quality of CNTs (SW and MW mixture) with highly distributed state, however, the consolidated composites by hot pressing at 1470 °C revealed no reinforcement effect on the fracture strength and toughness in spite of the presence of CNTs bundle in the composites. They conclude that the degradation of CNTs during the sintering might be a main reason for the undesired mechanical performance. Other preparation techniques such as sol-gel or hydrothermal reaction have been applied for the synthsis of ceramic-CNT powder

composites, which also enables highly CNTs dispersed powder mixtures [02See, 04Lup].

Ceramic synthesis via precursor polymer routes has a big advantage for the preparation of CNTs incorporated ceramic composites because of relatively easier CNT dispersion into the liquid precursor compared to the powder processes. Moreover, the precursor process can achieve the densification of the composites at relatively low temperature by means of the controlled thermolysis condition. Further advantage of CNT addition in combination with precursor-derived Si-C-N ceramics is that carbon is in thermodynamic equilibrium with equilibrium phases of Si-C-N ceramics indicating no reactions to be suspected between CNTs and Si-C-N matrix. According to these viewpoints, An et al. [04An] recently synthesized CNTs incorporated Si-C-N ceramics by catalytic cross-linking and pressure assisted thermolysis from the mixtures of a poly(ureamethylvinyl)silazane precursor and MWCNTs. They evaluated the mechanical properties by a nano indentation technique and revealed increases in the Young's modulus (120 GPa) and hardness (13 GPa) of Si-C-N/CNT composite containing 6.4 vol % CNT compared to pure material (73 GPa and 9.4 GPa, respectively). However, the effect of CNTs on the fracture toughness behavior has not been clarified. Moreover, the SEM image by the authors reveals highly dense web like CNT structure on the fracture surface with relatively large scale (Fig. 2.8), which gives rise to questions on the homogeneous distribution and debundle nature of CNTs during preparation.

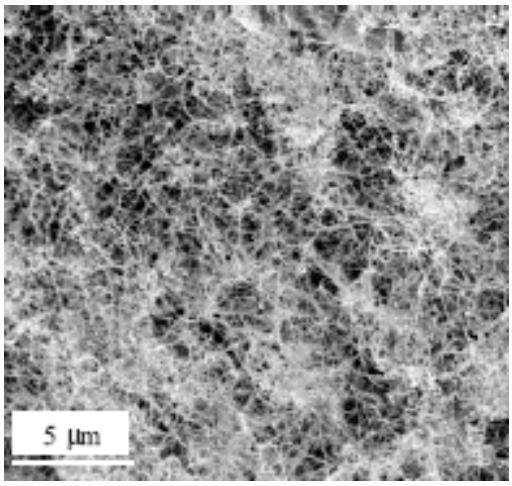


Fig. 2.8. SEM micrograph of the fracture surface of Si-C-N/CNT composites containing 6.4 vol % MWCNTs [04An].

# 3. Experimental

## 3.1. General comments for sample preparation

A commercial liquid poly(ureamethylvinyl)silazane (Ceraset™, see Fig. 2.3, [Kio]) was used for the preparation of Si-C-N ceramics. For Si-B-C-N ceramics, two types of boron-containing polysilazane, T2-1 and TCP (see Fig. 2.4 and 2.5, respectively), were prepared. Two types of commercially available MWCNTs (NanoLab, USA and Nanocs Inc., USA) and one type of SWCNTs (Carbon Nanotechnology Inc., USA) were used for the reinforcement of the precursor derived Si-(B-)C-N materials,.

The liquid precursors and their mixtures with CNTs were carefully handled by the standard Schlenk techniques. High purity argon and nitrogen gases, distilled tetrahydrofuran (THF) and toluene were applied for the preparation processes. Especially, in the case of Si-B-C-N ceramics, a nitrogen filled glove box was used to prevent the oxidation of the liquid and cross-linked solid precursors. Furthermore, CNTs were dried by vacuum heating at 160 – 180 °C for 2 h to remove adsorbed moisture. The contents of CNTs in the Si-(B-)C-N nanocomposites were adjusted from 0 to 2 mass %, which approximately corresponds to the volume content (vol. %) because of the similar density between CNTs (1.3 - 2.6 g/cm$^3$) [98Gao, 98Lu] and Si-(B-)C-N ceramics (2.0 – 2.2 g/cm$^3$).

## 3.2 Characterization

### 3.2.1 Bulk density, thermal expansion and elastic properties

Bulk density of the Si-(B-)C-N/CNT nanocomposites was measured by using a conventional Archimedes' principle in distilled water [02Kin]. The thermal expansion behavior was characterized by a differential dilatometer (Type 802, Baehr) with rectangular samples having a length of 10.0 mm, a width of 3 mm and a thickness of 0.4 mm. The measurement was carried out in an argon atmosphere with a heating rate of 5 °C/h. The elastic properties such as Young's modulus, E, and Poisson's ratio, ν, were measured by using a resonant frequency and damping analyzer (Integrated Material Control Engineering n.V.) [Imc]. For these measurements, disc shaped samples of 12 mm in diameter and 0.3 mm in thickness with fully polished surfaces were prepared.

### 3.2.2 Thermal stability and X-ray diffraction analysis

The thermal stability of the Si-(B-)C-N/CNT nanocomposites was analyzed by a high temperature thermogravimeter (STA 501, Baehr), where a heating rate of 10 °C /min up to 1400 °C and 2 °C /min from 1400 °C to 2200 °C was applied under a flowing argon atmosphere. X-ray diffraction analysis was carried out with a diffractometer (D5000, Siemens) using Cu-Kα radiation in the 2θ range of 10 – 80 °.

### 3.2.3 Chemical analysis

The chemical composition of the Si-(B-)C-N/CNT nanocomposites was analyzed by a combination of different analysis techniques. Silicon and boron were determined by an atomic emission spectroscopy with inductively coupled plasma excitation (JY70 Plus, ISA JOBIN YVON). Carbon, nitrogen and hydrogen were analyzed by a combustion method (Vario El, Elementar Americas). Oxygen was detected by a carrier gas hot extraction analysis (TC-436 DR, Leco).

### 3.2.4 Fracture toughness

Fracture toughness behavior of the Si-C-N/CNT nanocomposites was investigated by using the thermal loading technique developed by Petzow et al [91Sch, 93Mar] in combination with the weight function approach established by Brueckner et al [70Bru]. Disc shaped samples with and without a notch were used for the determination of thermal stress and fracture toughness behavior. A picture of the thermal loading apparatus and the illustration of measuring system are shown in Fig. 3.1.

***Thermal loading and measurement of the temperature distribution***

A circular disk sample with fully polished surface, which dimension is 12 mm in a diameter and 0.2 – 0.3 mm in a thickness, is placed on the sample holder with two zirconia pins. The disk sample is heated by irradiation of a tungsten lamp (Max. 150W) which produces a concentric temperature distribution in the sample. In order to apply the desired temperature distribution, the applied voltage of the lamp is precisely controlled at the rate of 1 V/130 sec by a power supplier (Konstanter, Gossen) via signals of an AD-DA converter (III3, Microlink) from a personal computer. The temperatures of the sample measured by a pyrometer (Dr. Georg Maurer GmbH) are stored in the personal computer as the dynamic temperature-time relations. By

moving the pyrometer position in step-by-step along the horizontal axis, ((x,y)=(-5, 0), (-4, 0), …, (0, 0), …, (+4, 0), (+5,0), unit in mm), the temperature distribution of the sample is gathered as a function of time and the lamp voltages.

(a)

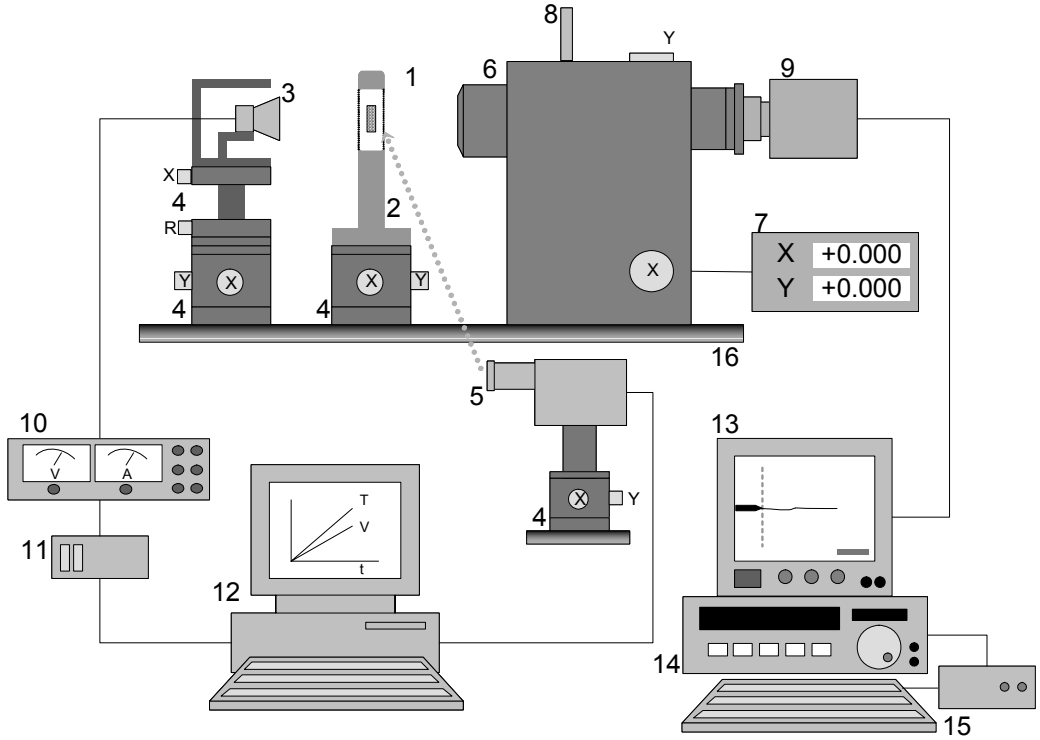


1. Sample. 2. Sample holder. 3. Halogen lamp. 4. Stages (X-Y or X-R controlled). 5. Pyrometer. 6. Optical microscope with X-Y positioning stage. 7. X-Y position display. 8. Electric light. 9. CCD camera. 10. Power supplier. 11. AD-DA converter. 12. Personal computer. 13. Video monitor. 14. Digital video recorder. 15. Text/Time generator. 16. Common rails

(b)

Fig. 3.1. A picture of the thermal loading apparatus (a) and the illustration of the measuring system (b).

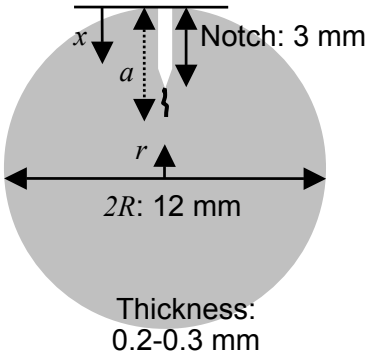


Fig. 3.2. Geometry of the notched sample for fracture toughness measurement.

***Approximation of the measured temperature distribution***

The measured temperature-time relations at each radius position are converted to the temperature distribution as a function of radius at different lamp voltages. This profile gives an axial symmetric temperature distribution of the specimen. The temperature distribution at each applied voltage is fitted by the forth order polynomial described in Eq. (3.1) by using a least-squares method [91Sch, 93Mar]:

$$T(r,t) = c_0(t) + c_2(t)r^2 + c_4(t)r^4, \tag{3.1}$$

where $r$ is the radial distance, $t$ is the time and $c_o(t)$, $c_2(t)$ and $c_4(t)$ are time-dependent fitting parameters.

***Calculation of the stress intensity factor and the fracture toughness***

The induced higher temperature at the center of the sample generates the tensile hoop stresses at the edge and tangential and radial compressive stresses in the center. To evaluate the fracture toughness behavior of the materials, a radially oriented single notch was induced in the sample as shown in Fig. 3.2, where a crack propagates from the edge to the center. That is, the tensile stress perpendicular to the crack face near the crack tip (Mode I) and their stress intensity factors were considered.

For the determination of stress intensity factor, $K_I$, the weight function

theory developed by Bruckner [70Bru] as in Eq. (3.2) can be available:

$$K_I = \sigma^* \sqrt{a} Y = \int_0^a h(x,a)\sigma(x)dx\,, \tag{3.2}$$

where $\sigma^*$ is a characteristic value of the stress distribution, $a$ is the crack length, $Y$ is the geometric function, $x$ is the distance from the edge, $h(x,a)$ is the weight function and $\sigma(x)$ is the stress distribution of the sample. According to this theory, the stress intensity factor is correlated with any given stress distribution and its weight function. Since the weight function is peculiar to the sample geometry and the crack types, several studies have been discussed for the solution of the weight function parameter for an edge-cracked disk sample [73Roo, 89Gre, 89Sch, 97Fet]. In this study, the solution derived by Fett [97Fet] in Eq. (3.3) is applied because of its reliability and facility for computation:

$$h(x,a) = \sqrt{\frac{2}{\pi a}}\left[\frac{\rho}{\sqrt{1-\rho}} + D_0\sqrt{1-\rho} + D_1(1-\rho)^{3/2} + D_2(1-\rho)^{5/2}\right], \tag{3.3}$$

where $\rho = x/a$, $D_0$, $D_1$ and $D_2$ are coefficient functions derived by the crack length as follows:

$$\begin{aligned} D_0 &= \left(1.5721 + 2.4109\beta - 0.8968\beta^2 - 1.4311\beta^3\right)/(1-\beta)^{3/2} \\ D_1 &= \left(0.4621 + 0.5972\beta + 0.7466\beta^2 + 2.2131\beta^3\right)/(1-\beta)^{3/2} \\ D_2 &= \left(-0.2537 + 0.4353\beta - 0.2851\beta^2 - 0.5853\beta^3\right)/(1-\beta)^{3/2} \\ \beta &= a/(2R), \quad R: \text{Radius of the disk.} \end{aligned} \tag{3.4}$$

The stress distribution, $\sigma(r)$, produced in the tangential direction of a circular disk with temperature distribution, $T(r)$, was defined by Boley [85Bol]:

$$\sigma(r) = \alpha E\left[\frac{1}{R^2}\int_0^R T(r)rdr + \frac{1}{r^2}\int_0^r T(r)rdr - T(r)\right], \tag{3.5}$$

where $\alpha$ is the coefficient of thermal expansion, $E$ is the Young's modulus and $R$ is the radius of the disc sample. The coordinate in the radius, $r$, has a relation to $x$ by

$x=R-r$. In this study, the temperature dependence of the thermal expansion coefficient, $\alpha(T)$, is taken into account in the Eq. (3.5) giving the following stress distribution:

$$\sigma(r)=\alpha(T)E\left[\frac{1}{R^2}\int_0^R T(r)rdr+\frac{1}{r^2}\int_0^r T(r)rdr-T(r)\right]. \tag{3.6}$$

By substituting Eq. (3.1) for $T(r)$, $\alpha(r, t)$ for $\alpha(T)$ in Eq. (3.6), the final equation of the stress intensity factor is described as follows:

$$K_I=\int_0^a h(x,a)\sigma(x)dx$$

$$=E\int_0^a\left[h(x,a)\alpha(x,t)\left[\frac{1}{R^2}\int_0^R T(x,t)xdx+\frac{1}{r^2}\int_0^r T(x,t)xdx-T(x,t)\right]\right]dx\,. \tag{3.7}$$

If the crack length, $c$, and the time, $t_c$, are known, the fracture toughness at the crack tip can be determined by substituting of $c$ and $t_c$ for $a$ and $t$ in Eq. (3.7).

***Trace of the crack propagation and the calculation of fracture toughness***

The notched sample (Fig. 3.2) was firstly placed on the sample holders as the notch perpendicular to the horizontal axis at the top. To induce a short crack in the sample, the edge of the notch was heated by lamp irradiation. After moving the lamp back to the center position, the thermal stress was induced into the sample with the same heating condition to the measurement of temperature distribution. During the lamp irradiation, crack propagation occurs when the thermal stress at the crack tip reaches its critical value. The crack propagation is traced by an optical microscope (QM-100, Questar) combined with a CCD camera (3CCD, Hitachi) and a color video monitor (BT-H1450Y, Panasonic), and recorded by a digital video recorder (DHR-1000VC, Sony). This system attains the maximum magnification of ca. 1000 times on the 14 inches monitor. The crack tip position and crack length can be determined by reading the position of optical microscope which is gauged with the X-Y positioning stage in a micrometer unit (Quester). The heating time of the sample is displayed on the monitor via a text generator (VTG-8, Deininger) so that the picture of crack propagation can be recorded on a digital video tape together with

time and the X-Y position of the microscope.

Finally, the stress intensity factor and fracture toughness as well as the thermal stress are calculated on a Maple (Ver. 7, Waterloo Maple) software programmed by Narayanan [See Appendix 1].

### 3.2.5 Nano indentation

Hardness and Young's modulus of the Si-B-C-N/CNT nanocomposites were measured by a scanning nanoindenter (TriboScope$^{R}$, Hysitron Inc., USA) in combination with a scanning probe microscope (SPM). A three sided diamond tip with a cube corner was loaded to the fully polished surfaces of the samples with maximum load of 12 mN. Measurement and calculation were performed for different 10 positions at each sample.

### 3.2.6 Microstructural analysis

Microstructural analysis of CNTs and Si-(B-)C-N/CNT nanocomposites was carried out with a scanning electron microscope (SEM; JSM-6300F, JEOL or DSM982, Zeiss) and a transmission electron microscope (TEM; CM200, Philips). Concerning the sample preparation, pure CNTs were dispersed in an organic solvent by sonication and the suspension was dropped on a metal holder. As for TEM analysis of the nanocomposites, the samples with a thickness of ca. 100 μm and a diameter of less than 3 mm were dimpled and polished to the thickness of 20 - 30 μm by a dimple grinder (Model 656, Gatan Inc.) with diamond particles. After fixing the dimpled sample onto a copper ring holder with glue, the dimple was ion-milled by irradiation of $Ar^{+}$ (Model 691, Gatan Inc.) to obtain thin parts of nanocomposites. The power of ion guns was controlled to be 3 kV and the dimple was monitored by an optical microscope (DMRM, Leica) equipped with a video camera (TK-1070E, JVC) and a monitor during ion-milling.

## 4. Results and discussion

### 4.1 Characterization of carbon nanotubes

The characteristics of two types of MWCNTs (named type A and B) and one type of SWCNTs are summarized in Table 4.1 based on the suppliers' data. All types of CNTs have been purified by the suppliers so that the impurities such as catalytic metals are quite small.

SEM and TEM micrographs of the MWCNTs are shown in Fig. 4.1 and Fig. 4.2, respectively. It can be seen in Fig. 4.1 that the type A-CNTs are smaller in diameter and relatively longer than the type B ones, which indicates the high aspect ratio of type A-CNTs (length to radius). TEM micrographs of type A-CNTs (Fig. 4.2 a and b) reveal characteristic hollow structures of CNTs as well as several stacked graphene walls. In contrast, type B-CNTs mostly show the stuffed inside structure with no distinctive graphene walls indicating the amorphous carbon nature in majority. In both MWCNTs, the existence of metal particles is not obvious on the microscopic analyses, which is coincidence with the high purity nature described in the suppliers' data.

Fig. 4.3 shows SEM and TEM micrographs of SWCNTs. As can be seen, the SWCNTs have a smaller diameter and relatively agglomerated feature compared to both MWCNTs. In addition, the SWCNTs reveal bundled structure which may be composed of several tens of nanotubes.

Table 4.1. Characteristics of CNTs provided by the suppliers.

| Type | MWCNTs Type A | MWCNTs Type B | SWCNTs |
|---|---|---|---|
| Supplier | NanoLab Inc., USA | Nanocs Inc., USA | Carbon Nanotechnologies, Inc., USA |
| Grade/Name | Research grade | High purity MWNTs | HIPco$^{R}$ P |
| Method | CVD | CVD | Laser vaporization |
| Purity | > 95 % | ca. 90 % | > 80 % |
| Residuals | Fe, Co, Ni | Not disclosed | Fe < 15 %, C (non-SWCNTs) < 5 % |
| Diameter | 20 ~ 50 nm | 10 ~ 50 nm Ave. 25 nm | ~ 1 nm |
| Length | 1 ~ 5 μm | 1 ~ 50 μm | 0.3 ~ 1 μm |
| Remark | Hollow structure | - | Bundle structure |

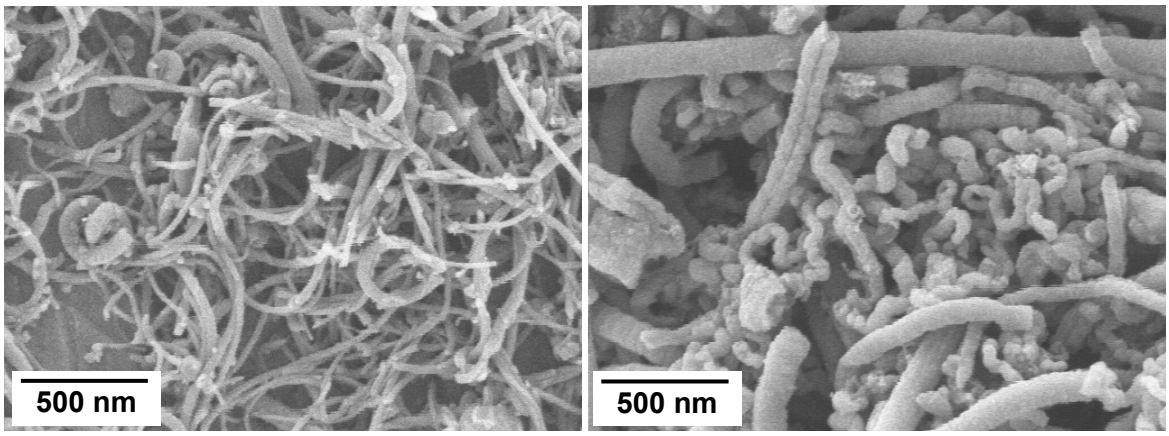


(a) (b)

Fig. 4.1. SEM micrographs showing the morphology of MWCNTs, (a) type A; high aspect ratio and (b) type B; low aspect ratio.

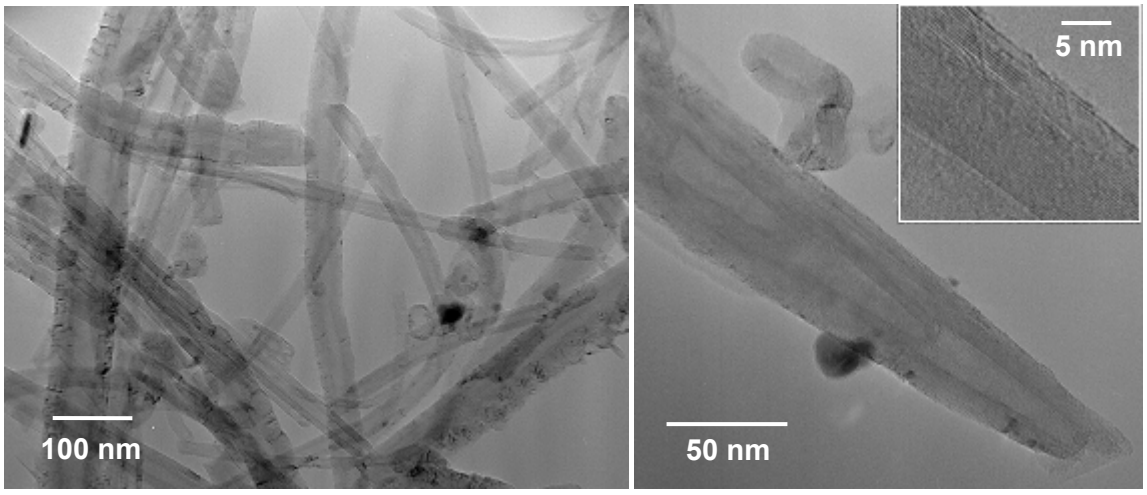


(a) (b)

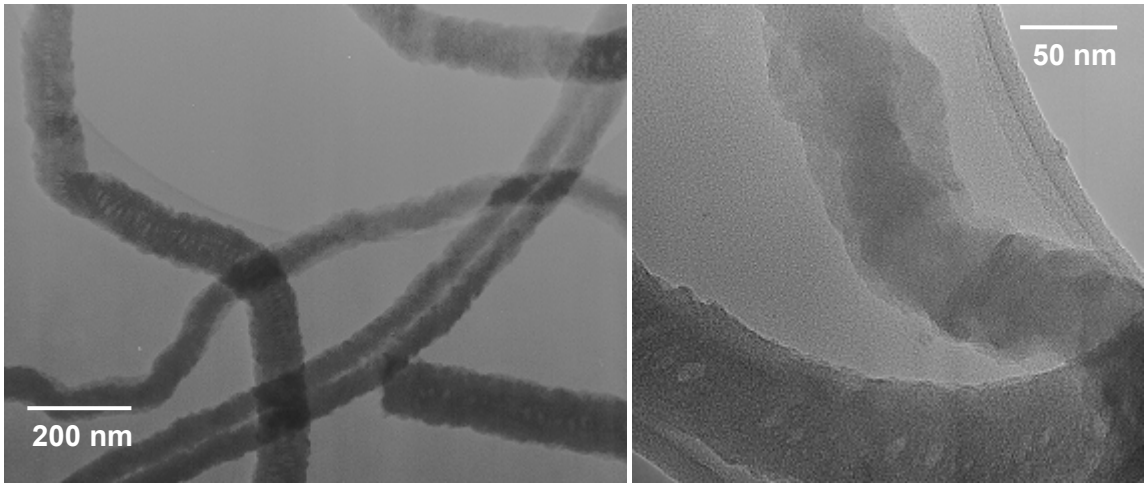


(c) (d)

Fig. 4.2. TEM micrographs showing the morphology of MWCNTs, type A (a and b) and type B (c and d). Characteristic hollow structure and the outer graphene walls are typically identified in the type A-MWCNTs.

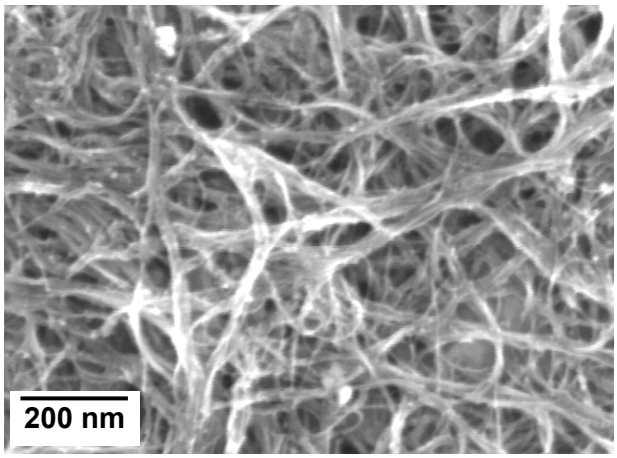


(a)

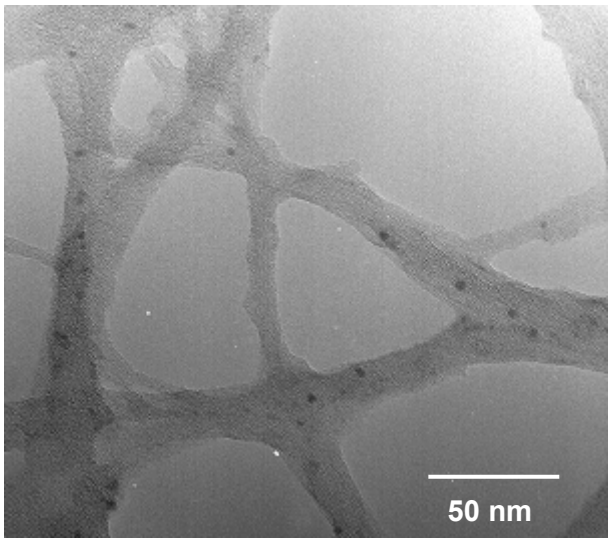


(b)

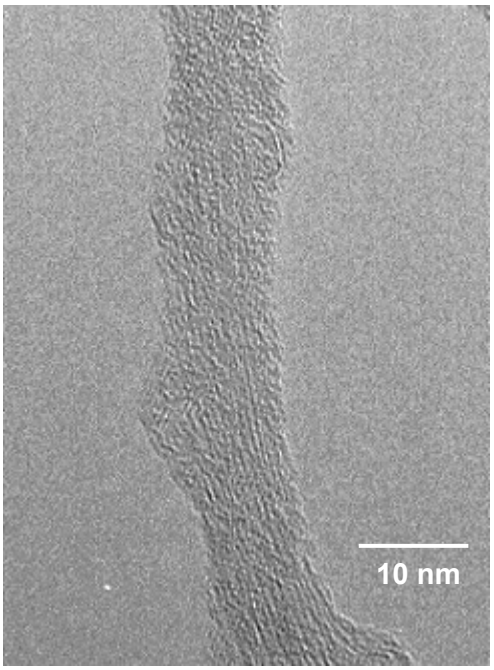


(c)

Fig. 4.3. Micrographs of the SWCNTs by SEM (a) and TEM (b, c). The bundled SWCNT structure is shown.

## 4.2 Si-C-N/MWCNT nanocomposites

### 4.2.1 Sample preparation

The overall preparation process for CNTs incorporated Si-C-N nanocomposites is shown in Fig. 4.4 as a flow chart. The process was modified and tailored for this study based on the casting process developed a former research [05Nar]. In the following sections, two critical processing parameters, the deagglomeration of CNTs and the heating rate for thermolysis of cross-linked materials, which control the quality of final Si-C-N/CNT nanocomposites will be stated. The casting mold designed for the preparation of cross-linked Si-C-N materials is introduced as well.

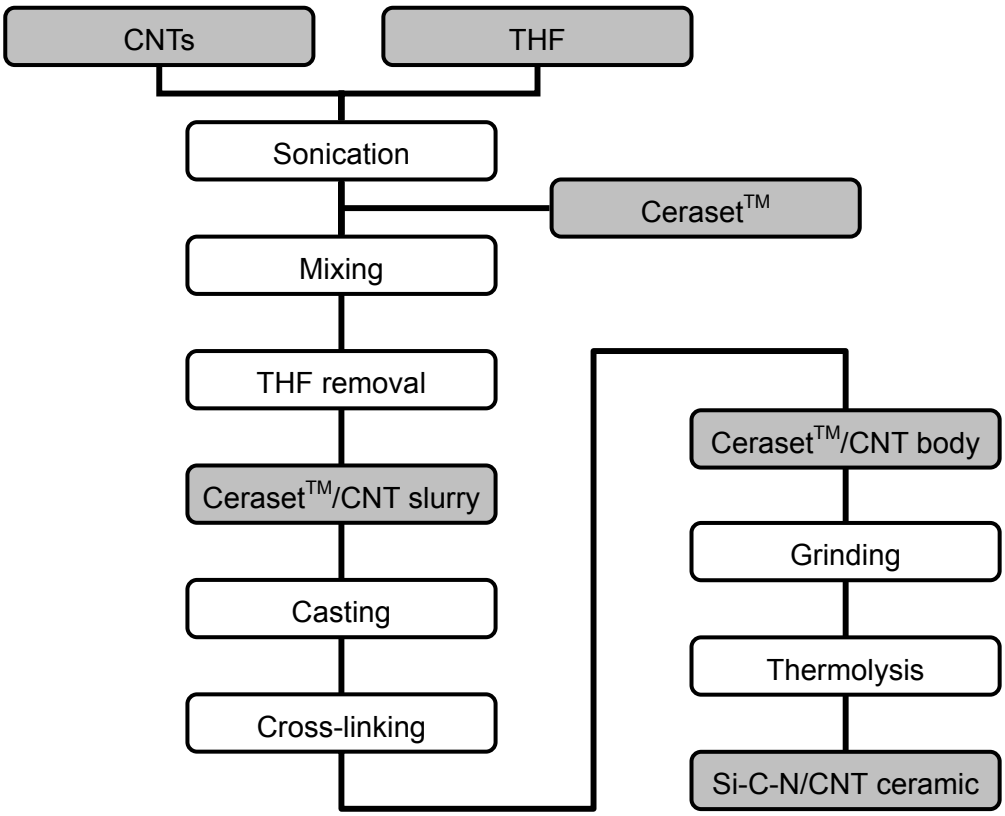


Fig. 4.4. Preparation process for the Si-C-N/CNT nanocomposites.

***Deagglomeration process: Effect of the sonication methods for the dispersion of CNTs***

CNTs are essentially agglomerated and the degrees are mostly depending on the production process and the dimension. The deagglomeration of CNTs is the most important process to achieve the homogeneously CNT distributed structure in the composites. At first, two different sonication methods by an ultrasonic bath (SONOREX RK 52H, 140 W, BANDELIN electronic) and an ultrasonic probe (SONOPULS HD2200, 200W, BANDELIN electronic) were examined to deagglomerate the CNTs within the Tetrahydrofulan (THF) solvent. In both methods, the duration time of sonication was fixed for 1 h. The processes except for the sonication of CNTs such as cross-linking and thermolysis were the same as the optimized condition described below. Fig. 4.5 shows SEM micrographs on the fracture surfaces of thermolysed Si-C-N/MWCNT nanocomposites containing 2 mass % of type A-CNTs. It can be seen that the CNTs dispersed by the ultrasonic bath are still agglomerated in the Si-C-N matrix. On the other hand, the material sonicated by the ultrasonic probe reveals homogeneously distributed CNTs in the matrix. Consequently, the sonication process by the ultrasonic probe was adopted to deagglomerate and disperse CNTs in the solvent.

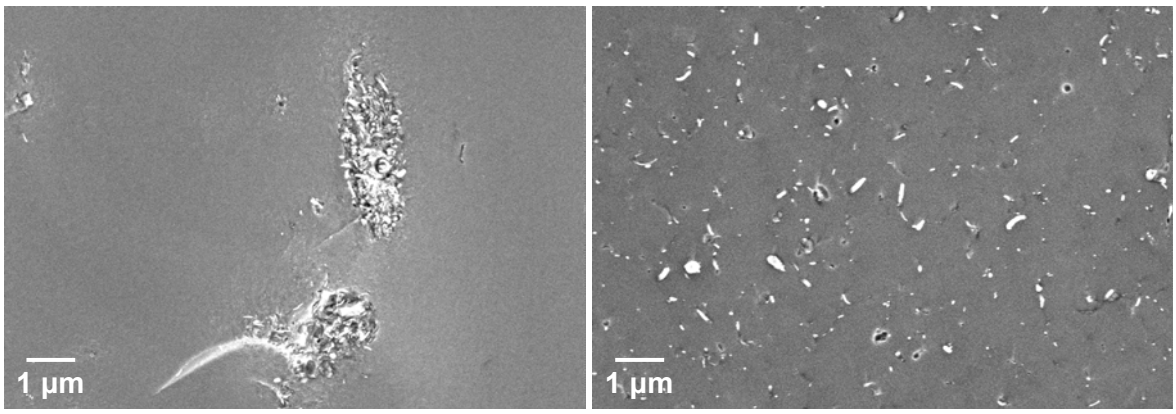


(a) (b)

Fig. 4.5. SEM micrographs of the fracture surface of the Si-C-N/CNT nanocomposites containing 2 mass % type A-CNTs prepared by different sonication methods, (a) an ultrasonic bath and (b) an ultrasonic probe. The homogeneously distributed CNTs in the Si-C-N matrix can be achieved by using the ultrasonic probe (b).

***Shaping process: Mixing, casting and cross-linking***

The CNTs suspension in THF after sonication was mixed with a liquid poly(ureamethylvinyl)silazane precursor by a magnetic stirrer for 1 h under an argon atmosphere. THF was then removed by evacuating, which gives a viscous mixture of CNTs and the precursor. The viscosity of the mixtures had a tendency to increase with the amount of CNTs in both cases. The obtained mixture was then cast into a Teflon mold (18mm in diameter and 1 mm in thickness) by a pipette and the mold was tightly covered by a metal die. Fig. 4.6 shows the picture of the Teflon mold and metal dies (a) with the dimensions (b). Three sets of metal dies were positioned in a glass vessel and the inside was filled with argon after removing air by evacuating. The cross-linking of mixtures was performed at 360 °C for 6 h with the maximum heating rate of the electric furnace (Heraeus) under an argon atmosphere. Fig. 4.7 shows a picture of the cross-linked materials produced by the above processes. The transparent body is derived from the pure precursor and the other black one is from the mixture of precursor with 2 mass % of type A-CNTs.

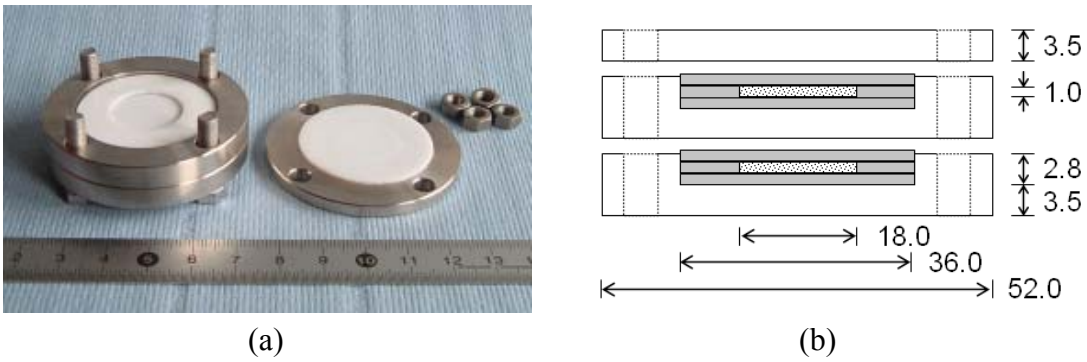


Fig. 4.6. Set of casting molds (a) and corresponding dimensions in mm (b).

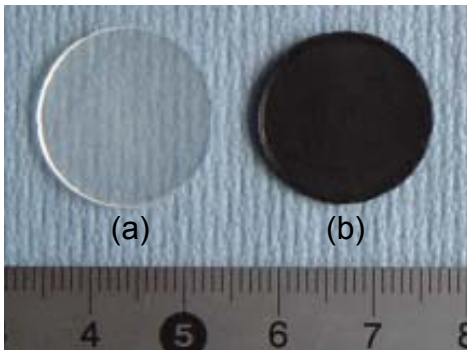


Fig. 4.7. Cross-linked materials from the pure Si-C-N precursor (a) and the CNT mixture containing 2 mass % type A-CNTs (b). Both were cross-linked at 360 °C for 6h.

***Microstructure of the cross-linked Si-C-N precursor/CNT nanocomposites***

Representative microstructures at the fracture surfaces of cross-linked materials are shown in Fig. 4.8. The pure Si-C-N precursor (Fig. 4.8 a) shows a featureless surface depart from the some steps which trace back to the cleavage of the material. Consistent with the transparent nature in Fig. 4.7, the pure cross-linked material appears to be dense and pore-free on the fracture surface. In the precursor nanocomposites containing 2 mass% CNTs (Fig. 4.8 b and c), both types of CNTs are confirmed as pulled out structure with uniform distribution in the cross-linked matrix. Furthermore, there are no holes identified at the interfaces between CNTs and the cross-linked matrix indicating the existence of strong bonding nature of CNTs to the cross-linked matrix. This interfacial feature is in contrast to the fracture surface of epoxy/CNT composites reported by Lau et al. [02Lau, See Fig. 2.7].

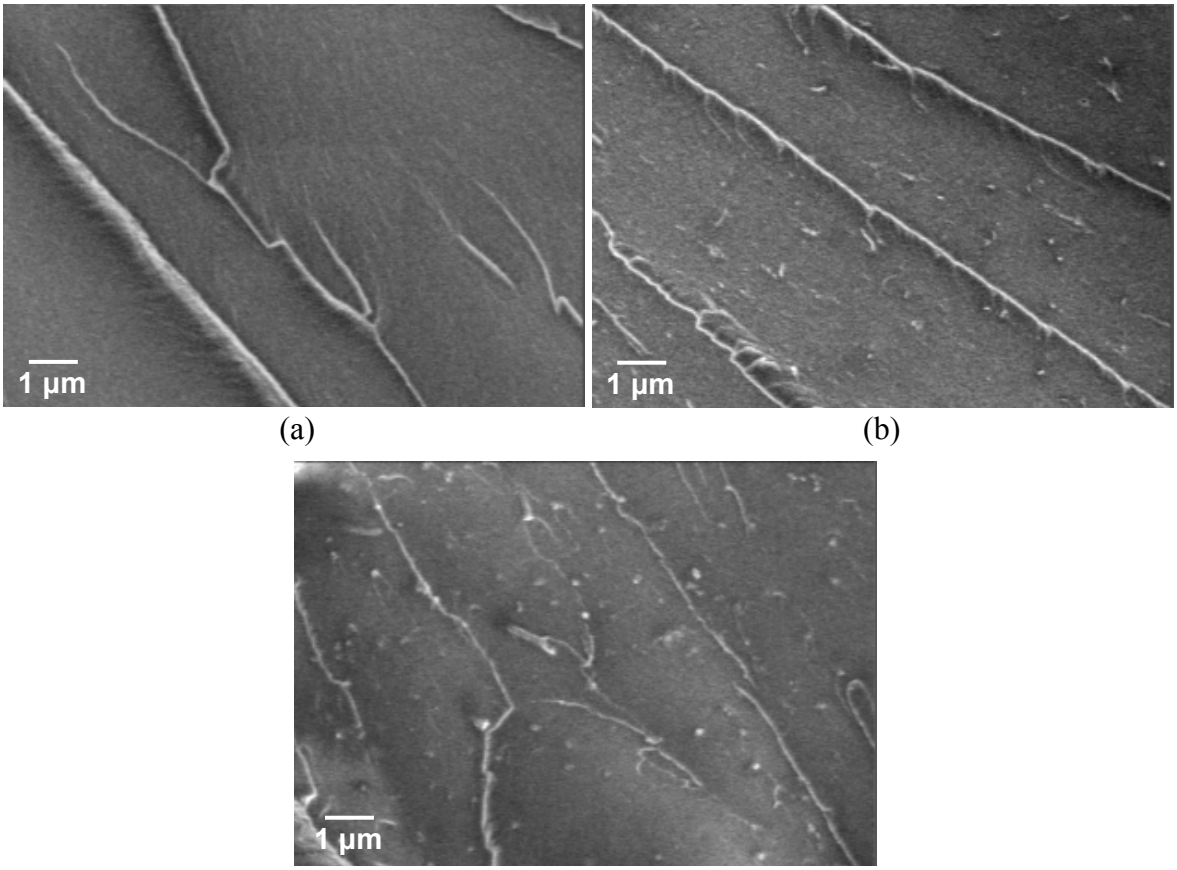


(a) (b)

(c)

Fig. 4.8. SEM micrographs of the fracture surfaces of cross-linked materials, (a) pure Si-C-N precursor, (b) 2 mass % type A-CNTs nanocomposite and (c) 2 mass % type B-CNTs nanocomposite. All materials were cross-linked at 360 °C for 6h.

***Ceramization process: Effect of the heating rates on the thermolysis of cross-linked materials***

After grinding the cross-linked materials to the thickness of 0.6 – 0.7 mm with sand papers (# 800 and 1200), the materials were placed between two graphite mats and stacked in an alumina crucible. The thermolysis was carried out in a quartz tube at 1000 °C for 1 h under a flowing argon atmosphere, where the heating rates of 100 °C/h and 25 °C/h were examined in order to obtain crack free Si-C-N/CNT nanocomposites. Fig. 4.9 shows the polished surfaces of the thermolysed materials by diamond particles (1/4 μm). It can be seen that the heating rate of 100 °C/h, which is standard condition for the thermolysis of pure Si-C-N materials, leads to the formation of cracks if the content of MWCNT increases above 1 mass % in type A-CNTs incorporated nanocomposites. On the other hand in the case of the slower heating rate of 25 °C/h, there are no cracks observed on the polished surfaces of the nanocomposites even containing 1 mass % type A- or 2 mass % type B-MWCNT as well as no micro pores. It is considered that the MWCNTs embedded in the cross-linked materials give a kind of pinning effect against the shrinkage (20 % in a linear shrinkage) and weight loss (25 %) of the cross-linked matrix during thermolysis. Therefore, the higher thermolysis rate induced by the faster heating generates large thermal stress in the nanocomposites resulting in cracking. The heating rate of 25 °C/h was adopted for the thermolysis of all Si-C-N/MWCNT materials.

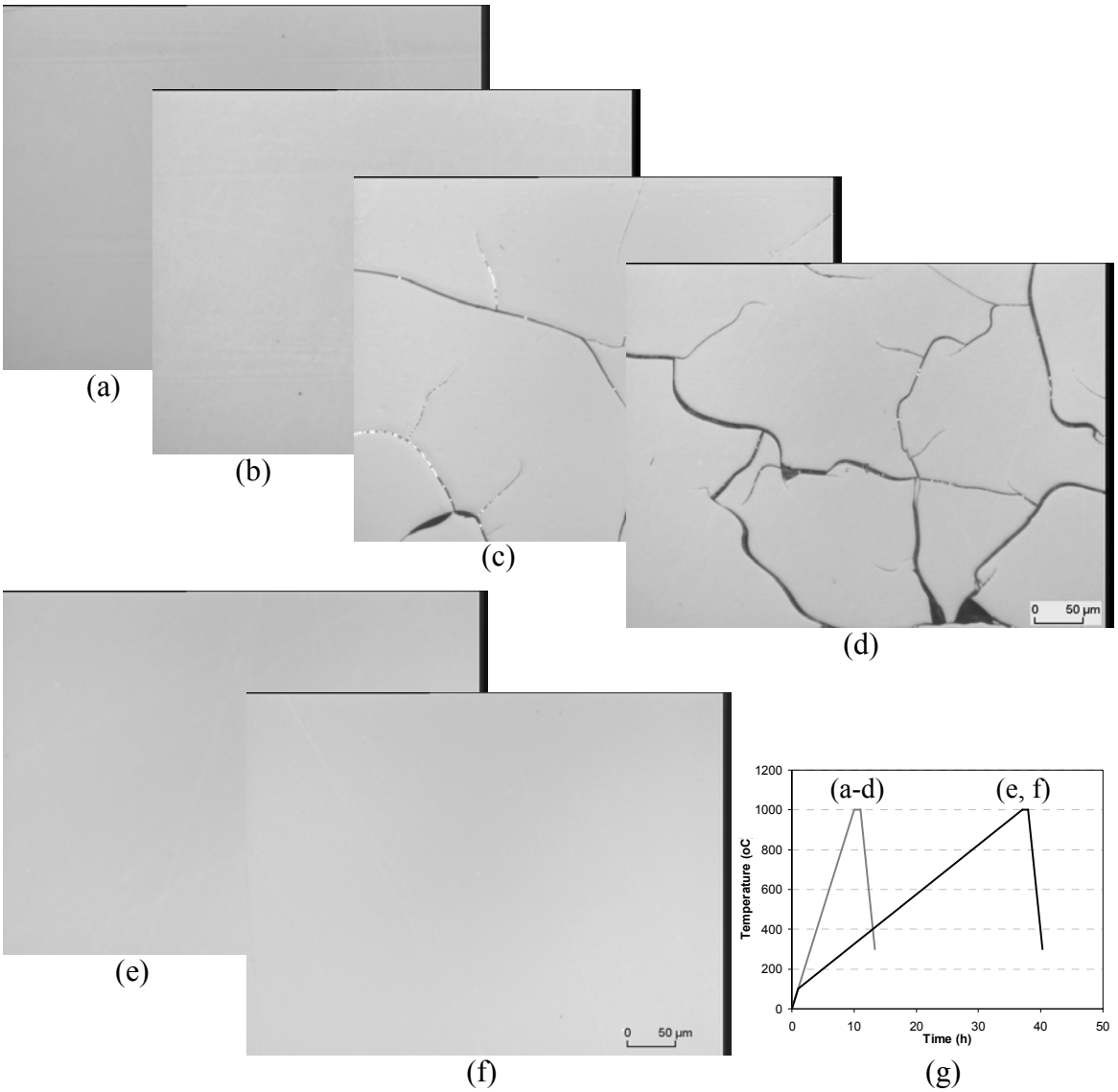


Fig. 4.9. Polished surfaces of the Si-C-N/CNT nanocomposites thermolysed with different heating rates. Heating rate of 100 $^{o}$C/h: (a) Pure Si-C-N, Si-C-N/CNT nanocomposites containing (b) 0.5 mass % type A-, (c) 1 mass % type A- and (d) 2 mass % type B-CNTs. 25$^{o}$C/h: Si-C-N/CNT nanocomposites containing (e) 1 mass % type A- and (f) 2 mass % type B-CNTs. The corresponding heating program is shown in (g).

### 4.2.2 General material properties of Si-C-N/MWCNT nanocomposites

***X-ray profiles***

Fig. 4.10 is the X-ray diffraction profiles of the materials thermolysed at 1000 °C for 1 h, in which the pure Si-C-N and the CNT composites containing 2 mass % CNTs are representatively shown. As can be seen, all materials reveal the X-ray amorphous nature with similar peak intensities. It is assumed that the addition of MWCNTs into the Si-C-N material has no influence on the formation of amorphous Si-C-N matrices drastically during thermolysis.

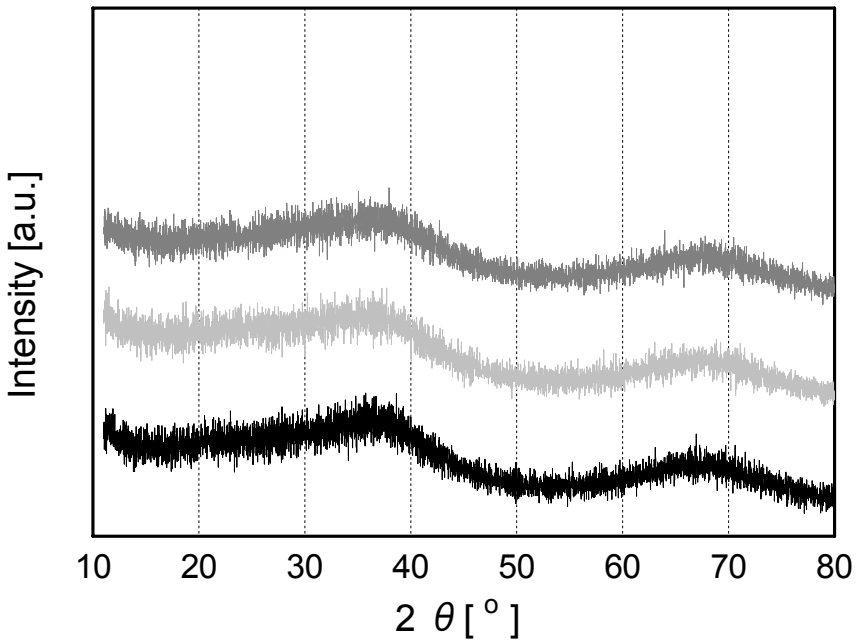


Fig. 4.10. X-ray diffraction profiles of the Si-C-N/CNT nanocomposites.
——— : Pure Si-C-N,
——— : Si-C-N/CNT nanocomposite containing 2 mass % type A-CNTs,
——— : Si-C-N/CNT nanocomposite containing 2 mass % type B-CNTs.

***Density***

The apparent density of the thermolysed materials at 1000 °C for 1 h is shown in Fig. 4.11 as a function of the amount of CNTs. The density of the pure Si-C-N material of this study is 2.15 g/cm$^3$ in average which is higher than that of the reported value of 2.00 g/cm$^3$ in the former study (thermolysis at 1000 °C for 1 h, heating rate of 100 °C/h) [05Nar]. The obtained higher density of this study is considered to be due to the effect of slower heating rate for thermolysis, where the materials can achieve large shrinkage with eliminating the micro pores during the

slower polymer to ceramic transformation. In the case of type A-CNTs nanocomposites, the density slightly tends to increase with the amount of MWCNTs. This tendency basically follows the "rule of mixtures" behavior of the density of composite materials. However, the calculated density of 2 mass % MWCNT incorporated Si-C-N material is a bit higher (2.21 g/cm$^3$) than that of the measured one (2.16 g/cm$^3$). The reason for this difference is still unclear since no difference is observed in the crystallinity by conventional XRD analysis (Fig. 4.10) as well as the pore distribution by microscopic analysis (Fig. 4.9). On the other hand in the density of type B-CNT nanocomposites, there is no tendency observed among the examined CNT contents. It is considered that the amorphous nature of type B-CNTs gives rise to the lower density of CNT than type A one resulting in the different density behaviors.

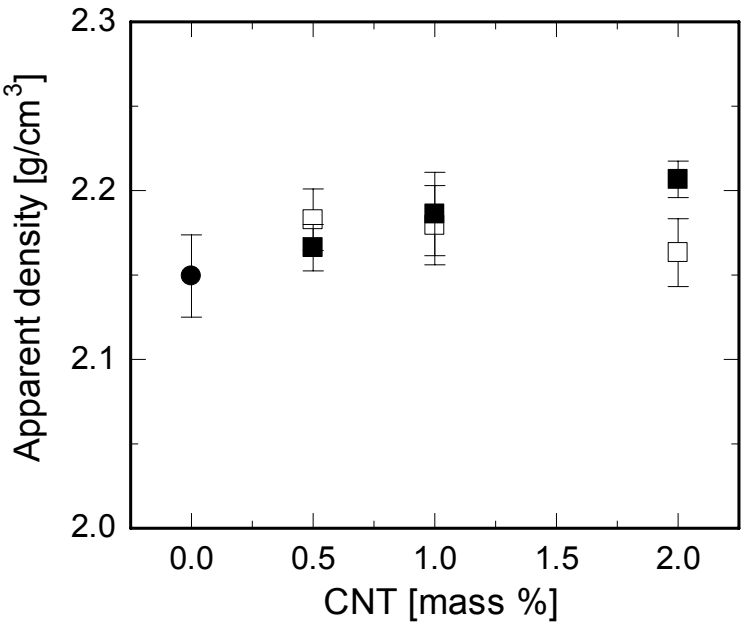


Fig. 4.11. Apparent density of the Si-C-N/CNT nanocomposites as a function of the amount of CNTs. ●: Pure Si-C-N, ■: Si-C-N/CNT nanocomposites containing type A-CNT, □: Si-C-N/CNT nanocomposites containing type B-CNT.

***Young's modulus, Poisson's ratio and thermal expansion***

The Young's modulus and Poisson's ratio of the thermolysed materials are respectively shown in Fig. 4.12 and 4.13 as a function of the amount of CNTs. In both properties, there is no striking tendency observed among the nanocomposites with different types of CNTs. These behaviors are considered to be due to the small amounts of CNT addition within the examined materials. Similar results were obtained from the behavior of thermal expansion coefficient as in Fig. 4.14.

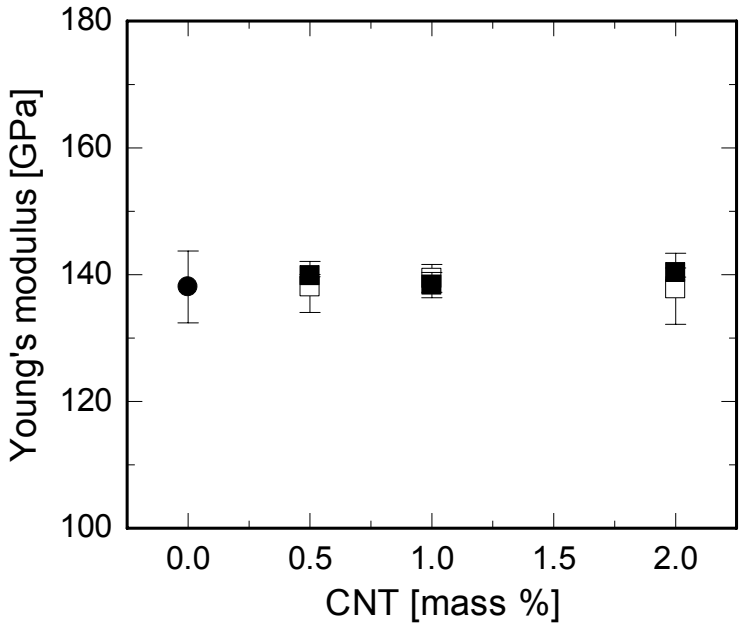


Fig. 4.12. Young's modulus of the Si-C-N/CNT nanocomposites as a function of the amount of CNTs. ●: Pure Si-C-N, ■: Si-C-N/CNT nanocomposites containing type A-CNT, □: Si-C-N/CNT nanocomposites containing type B-CNT.

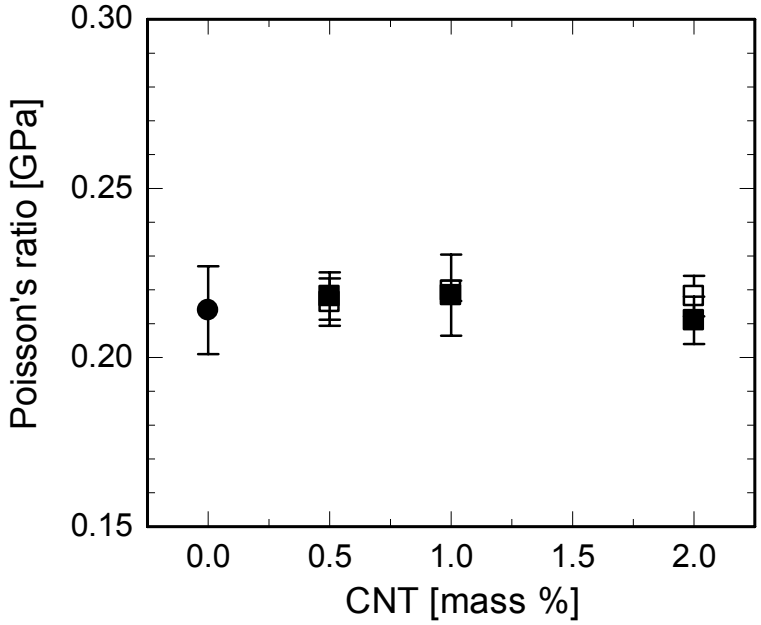


Fig. 4.13. Poisson's ratio of the Si-C-N/CNT nanocomposites as a function of the amount of CNTs. ●: Pure Si-C-N, ■: Si-C-N/CNT nanocomposites containing type A-CNTs, □: Si-C-N/CNT nanocomposites containing type B-CNTs.

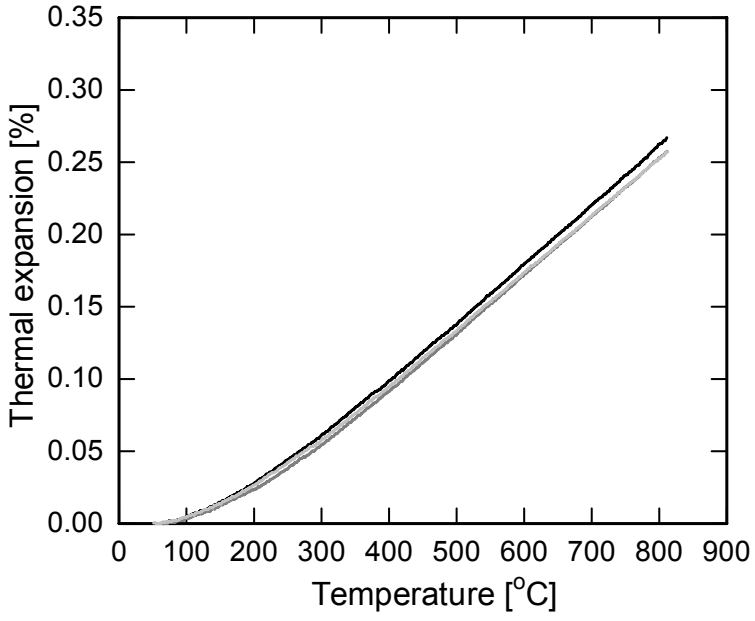


Fig. 4.14. Thermal expansion behaviors of the Si-C-N/CNT nanocomposites ($l_0$=50 °C). ——: Pure Si-C-N, ——: Si-C-N/CNT nanocomposites containing 2 mass % type A-CNTs, ——: Si-C-N/CNT nanocomposites containing 2 mass % type B-CNTs.

### 4.2.3 Thermal stability and chemical analysis

The thermogravimetric behavior of the Si-C-N nanocomposites containing 2 mass % type A- or type B-CNT as well as of the pure Si-C-N material are shown in Fig. 4.15. As can be seen in the diagram, all materials show similar weight loss behaviors around 1400 - 1600 °C. Table 4.2 exhibits the chemical compositions of the pure Si-C-N material and the nanocomposites containing 2 mass % CNT. It can be confirmed that no significant deviation of the chemical composition occurred among the materials except a slight increase of carbon content for the nanocomposites. According to the thermodynamic calculations of Si-C-N materials by Seifert et al [99Sei, 01Sei, 02Sei], the following two reactions related with silicon nitride are responsible for the weight loss behaviors of the Si-C-N materials:

$$Si_3N_4(s) + 3C(s) \xrightarrow{1484^oC,\ P_{N_2}=1bar} 3SiC(s) + 2N_2(g) \qquad (4.1)$$

$$Si_3N_4(s) \xrightarrow{1841^oC,\ P_{N_2}=1bar} 3Si(l) + 2N_2(g) \qquad (4.2)$$

One is the reaction of silicon nitride with carbon to give silicon carbide and nitrogen gas above 1484 °C (Eq. 4.1). The other is the decomposition of silicon nitride into liquid silicon and nitrogen above 1841 °C (Eq. 4.2). That is, the content of nitrogen is mainly corresponding to the weight loss of the materials. In the examined materials, the nitrogen contents are analyzed to be ca. 20 mass %, which is not so far from the observed weight loss of ca. 25 mass %. Moreover, thinking the content of hydrogen and oxygen in the materials (ca. 3 mass %) which might be volatile or give volatile compounds, the observed weight loss behaviors are quite reasonable for the Si-C-N/CNT materials. Consequently, it is revealed that the incorporation of CNTs into the Si-C-N ceramics does not affect the matrix ceramization and the structure fundamentally.

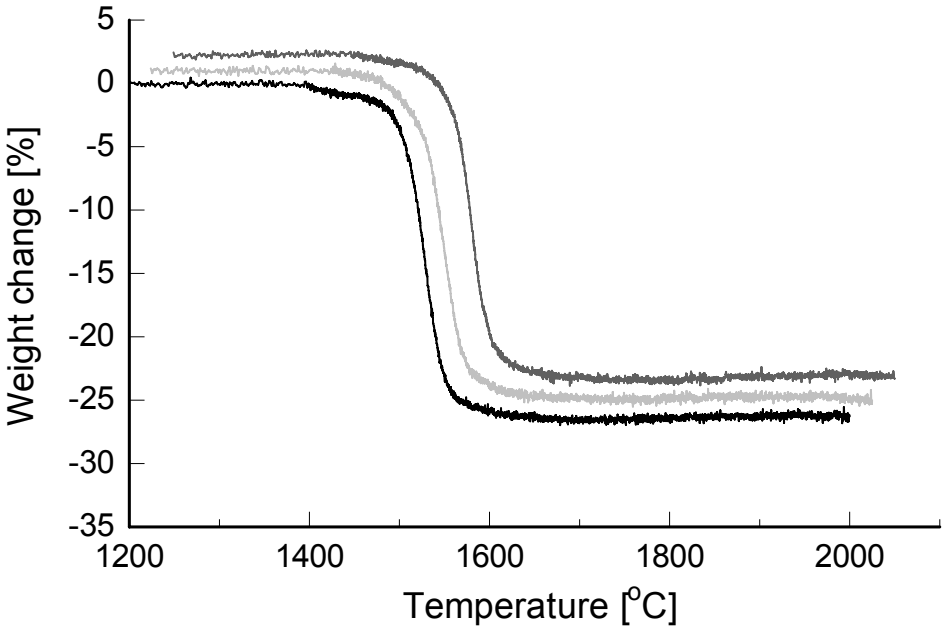


Fig. 4.15. Thermal gravimetric behavior of the Si-C-N/CNT nanocomposites.
: Pure Si-C-N, : Si-C-N/CNT type A (2 mass %),
: Si-C-N/CNT type B (2 mass %).

Table 4.2. Analyzed chemical compositions of the Si-C-N/CNT nanocomposites in mass %.

| Elements | Pure Si-C-N | Si-C-N/CNT 2 mass % type A | Si-C-N/CNT 2 mass % type B |
|---|---|---|---|
| Si | 56.6 | 56.5 | 54.6 |
| C | 20.5 | 21.2 | 21.9 |
| N | 19.4 | 19.8 | 20.3 |
| O | 2.0 | 1.3 | 1.6 |
| H | 1.3 | 0.9 | 0.9 |
| Sum | 99.8 | 99.7 | 99.3 |

### 4.2.4 Fracture toughness behavior

***Temperature function***

An example of the dynamic temperature-time distribution during thermal loading is shown in Fig. 4.16 at different sample positions along the horizontal axis. These measured temperature distribution is converted to the axial temperature distribution as in Fig. 4.17 by correlating the temperature data with the radial distances and lamp voltages. It can be seen that the measured temperature data (closed circles) are reasonably fitted by the forth order polynomials (solid lines) at each lamp voltage. The followings are examples of the fitted temperature functions at the lamp voltages of 2.6, 3.0 and 3.4. [See Appendix 2 for all data]:

V=2.6 V (t=338 sec.): $T_{V=2.6}(r) = 222.8624 - 4919874r^2 + 6.853\times10^{10} r^4$ (4.3)

V=3.0 V (t=390 sec.): $T_{V=3.0}(r) = 289.7006 - 5514911r^2 + 5.781\times10^{10} r^4$ (4.4)

V=3.4 V (t=442 sec.): $T_{V=3.4}(r) = 349.9105 - 6167039r^2 + 5.739\times10^{10} r^4$ (4.5)

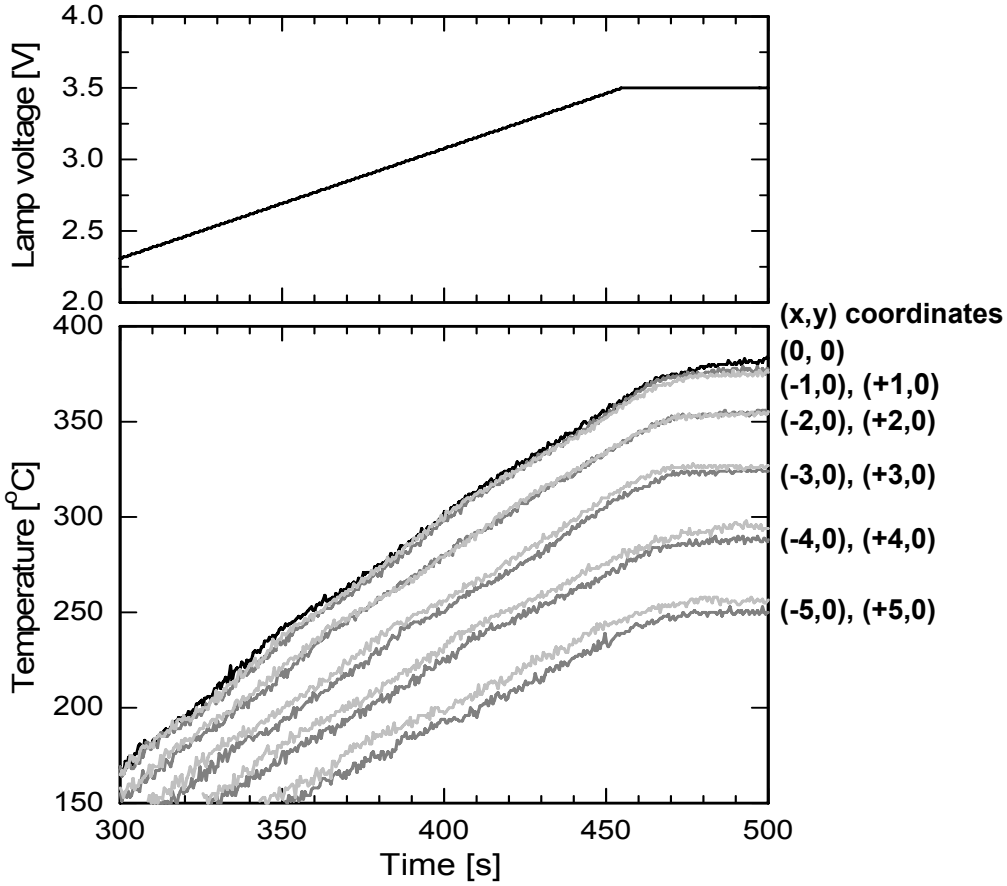


Fig. 4.16. Dynamic temperature distribution of the pure Si-C-N material at different sample positions: (x, y)=(-5, 0)…(0, 0)…(+5, 0). The upper figure shows the lamp voltage-time relation.

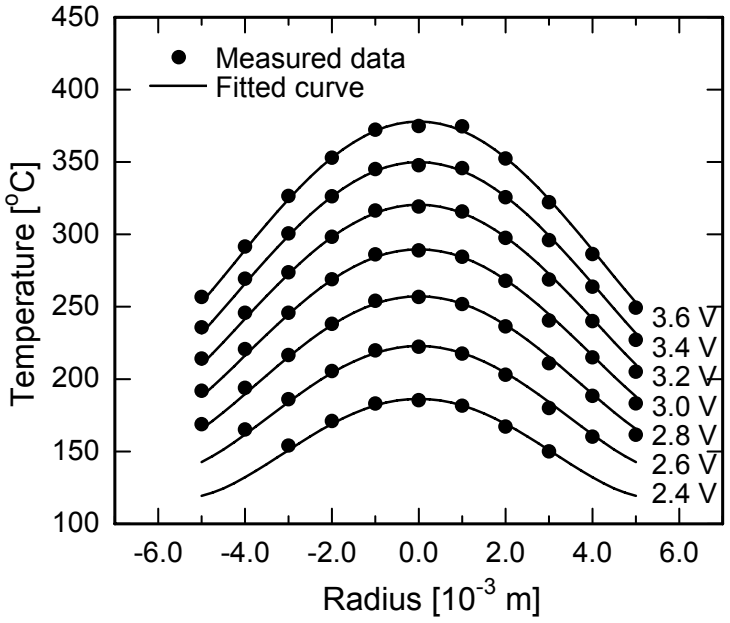


Fig. 4.17. Axial temperature distribution of the pure Si-C-N material at different lamp voltages resulted from the temperature-time relation in Fig. 4.16. Measured data (●) and the fitted curves by the forth order polynomial ( —— ) are shown. Radius=0.0 represents the center of the disc shaped sample.

***CTE function***

The linear coefficient of thermal expansion (CTE), $\alpha$, is generally defined as in Eq. (4.6) [76Kin]:

$$\alpha = \left(\frac{dl}{dT}\right)\frac{1}{l} \quad , \tag{4.6}$$

where $l$ is the length of the sample and T is the temperature. To facilitate the calculation of $\alpha$, the measured length-temperature cueves were fitted by an allometric function as in Eq. (4.7):

$$l = h + iT^{j} , \tag{4.7}$$

where $h$, $i$ and $j$ are the fitting coefficients. The derivation, $dl/dT$, of Eq. 4.7 and the subsequent insertion into Eq. 4.6 yields $\alpha$ relation as in Eq. (4.8):

$$\alpha = \frac{ij \cdot T^{(j-1)}}{l} \quad . \tag{4.8}$$

Fig. 4.18 shows a measured $l$-$T$ profile and the corresponding fitted curve for the pure Si-C-N material. From the fitted function Eq. (4.9) and the derivation Eq. (4.8), the $\alpha$ value at each temperature can be mathematically calculated as shown in Fig. 4.19. Finally, the temperature dependence of $\alpha$ is reasonably fitted by a cubic polynomial to

facilitate the calculation hereafter as Eq. (4.10) for the pure Si-C-N material.

$$l(T) = 10000.23296 + 4.9 \times 10^{-4} \times T^{1.6587} \quad (4.9)$$

$$\alpha(T) = 4.0653 \times 10^{-7} + 1.4549 \times 10^{-8} T - 1.9815 \times 10^{-11} T^2 + 1.8058 \times 10^{-14} T^3 \quad (4.10)$$

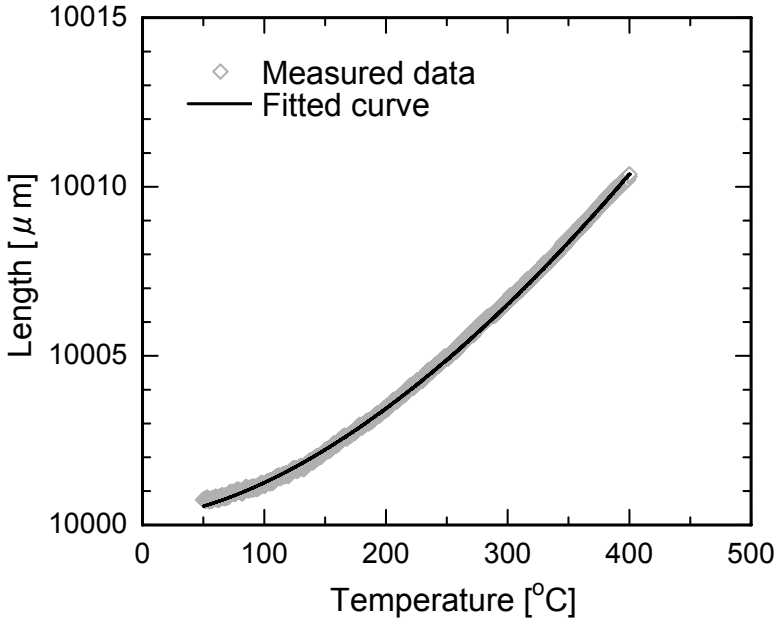


Fig. 4.18. Thermal expansion behavior of the pure Si-C-N material. Measured length data (◇) and the fitted curve by an allometric function (——) are shown

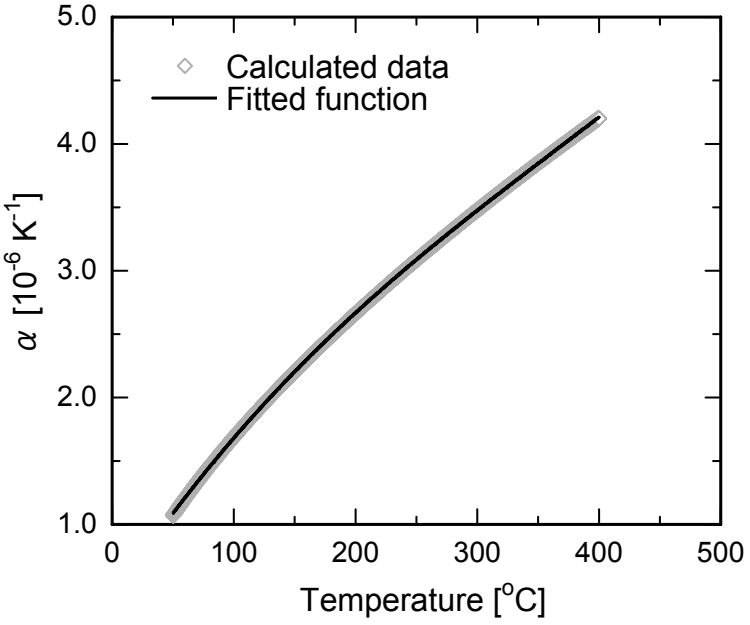


Fig. 4.19. Thermal expansion coefficient, $\alpha$, of the pure Si-C-N material. Calculated data from the Eq. 4.9 (◇) and the fitted curve by an allometric function (——) are shown

***Stress intensity factor***

The stress intensity factor, $K_I$, depending on time (lamp voltages) and crack lengths is calculated from the measured Young's modulus, the $\alpha$ function (Eq. 4.10) and the weight function method stated in the experimental section (3.2.4). The results of the stress intensity factor for the pure Si-C-N materials are shown in Fig. 4.20 as a function of the crack length at the different voltages. The Young's modulus of 138 GPa and $\alpha$ function of Eq. (4.10) were used for the calculation. Concerning other materials, the coefficients of each function as the temperature distribution and thermal expansion coefficient are described in Appendix 2 and 3.

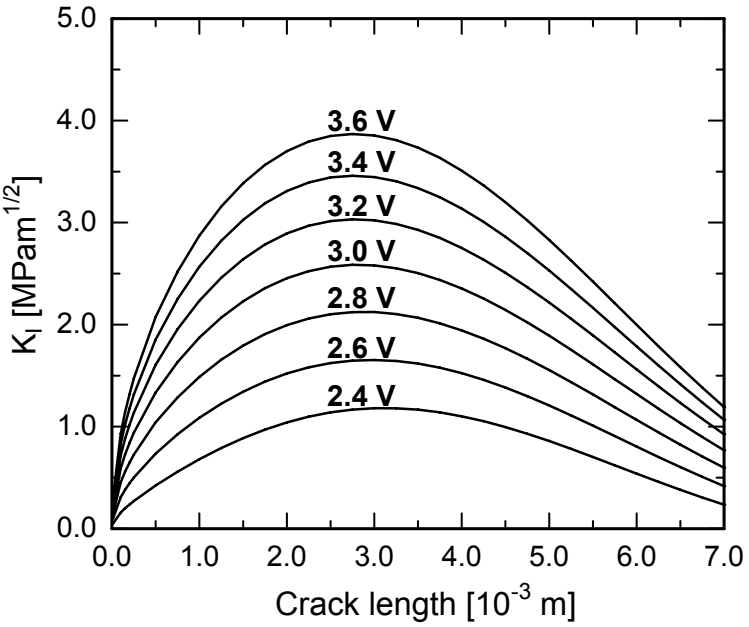


Fig. 4.20. Stress intensity factor, $K_I$, as a function of the crack length for the pure Si-C-N material calculated from the temperature distribution of Fig. 4.17.

***Crack propagation and fracture toughness***

Fig. 4.21 shows examples of the observed crack propagation on the video monitor for the Si-C-N/CNT nanocomposite containing 2 mass % type A-CNTs. At each picture, the crack tips are indicated by arrows and the corresponding heating time is located as well. In these pictures, it can be seen that the crack propagation is controlled to be slow for the evaluation of the fracture toughness, where the calculated crack velocity is ca. 21 μm/sec on an average. Fig. 4.22 demonstrates the fracture toughness behavior of the pure Si-C-N material determined by Eq. (3.6). The result reveals that the fracture toughness is nearly constant during the crack propagation under thermal loading. The similar measurements and calculations were

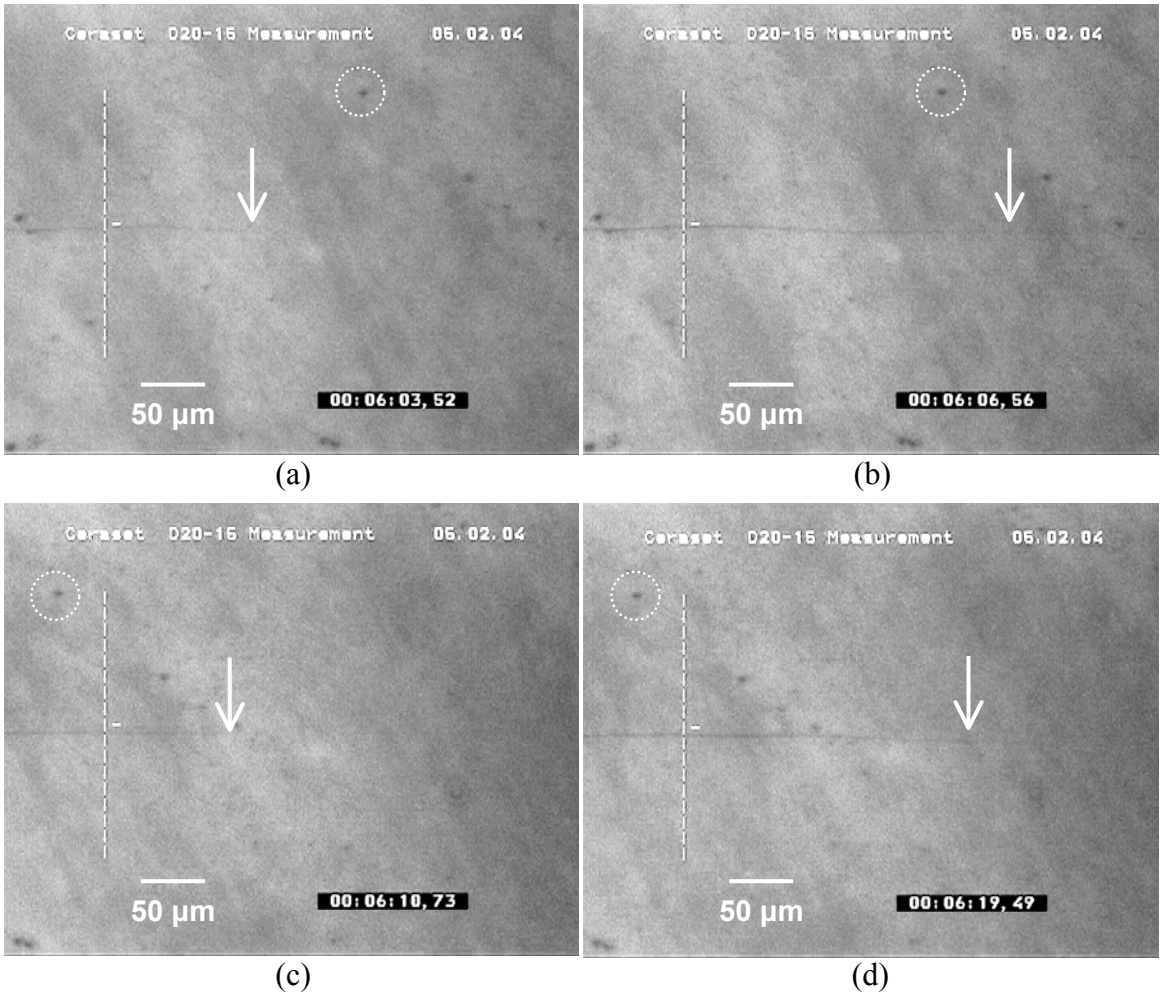


Fig. 4.21. Pictures showing the crack propagation during thermal loading. The arrows indicate the crack tips and the circles are corresponding to the same places. These pictures are obtained from the Si-C-N/CNT nanocomposite containing 2 mass % type A-CNTs.

performed to the other materials giving the fracture toughness behaviors as in Fig. 4.23. It can be seen that the Si-C-N/CNT nanocomposites also show nearly constant fracture toughness during crack propagation but their magnitudes are much different among the materials. Fig. 4.24 reveals the relationships between the averaged fracture toughness values and the amount of CNT in both types of the nanocomposites. As can be seen from the diagram, the incorporation of type A-CNTs significantly increases the fracture toughness of Si-C-N ceramics even at the content as low as 1 mass %. Moreover, the fracture toughness of the nanocomposite containing 2 mass % type A-CNTs reaches 1.80 $MPam^{1/2}$, which corresponds to an increase of more than 70 % compared to the pure Si-C-N material (1.04 $MPam^{1/2}$). On the other hand, the addition of type B-CNTs has no effect on the fracture toughness as revealed by the behavior similar to the pure Si-C-N.

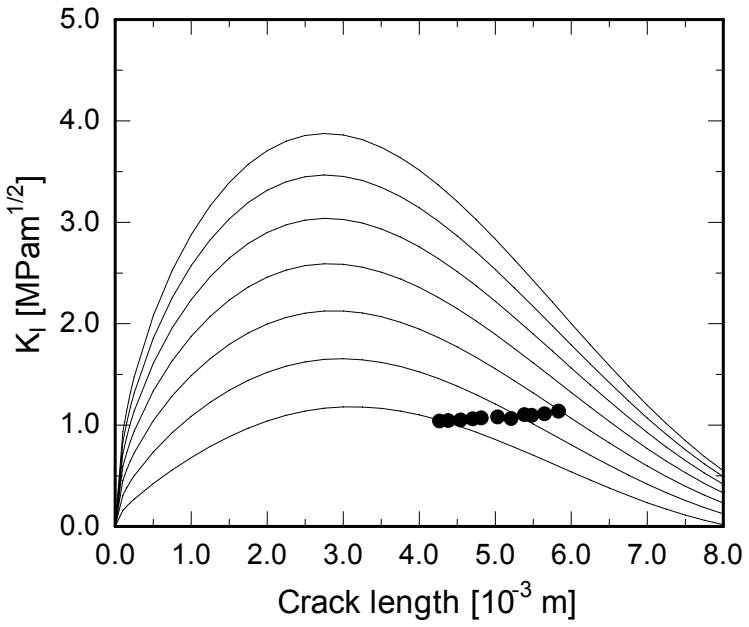


Fig. 4.22. Fracture toughness (●) of the pure Si-C-N material during the crack propagation. The lines are corresponding to the stress intensity factors resulted from Fig. 4.20.

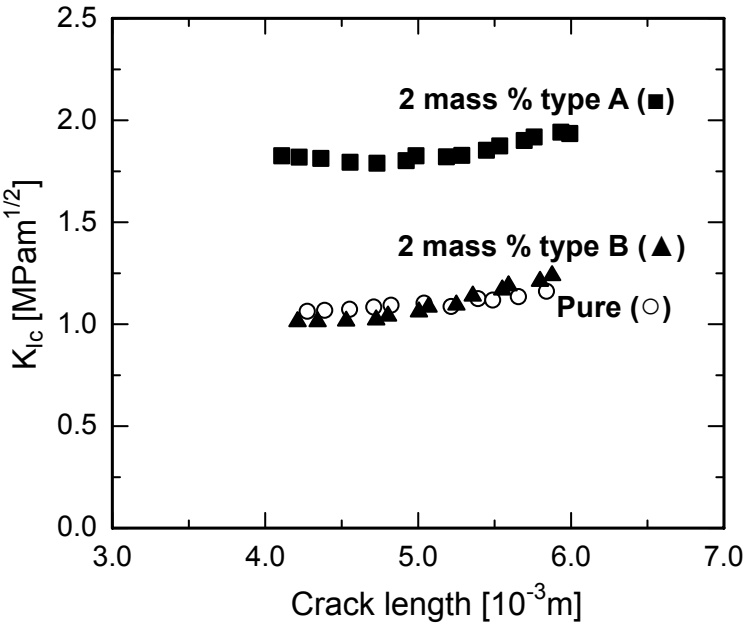


Fig. 4.23. Fracture toughness behavior of the pure Si-C-N and Si-C-N/CNT nanocomposites containing 2 mass % CNTs as a function of the crack length.

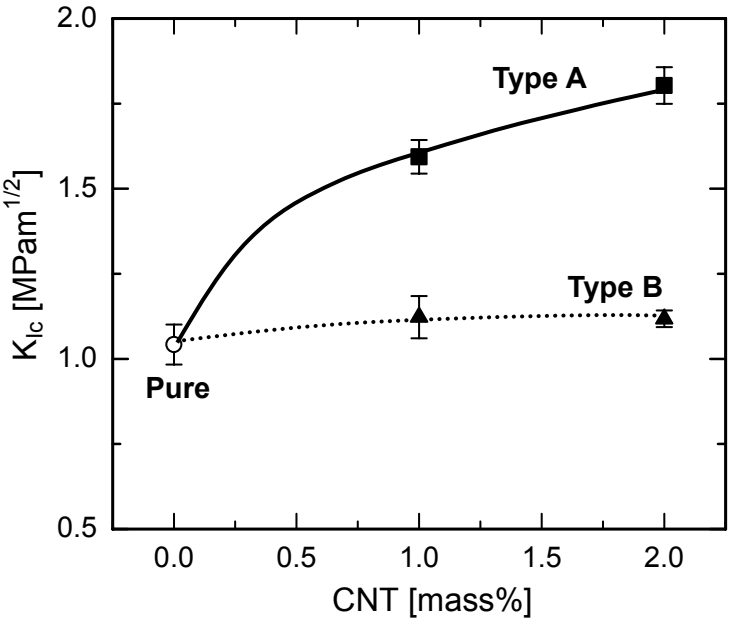


Fig. 4.24. Fracture toughness behavior of the pure Si-C-N and Si-C-N/CNT nanocomposites as a function of the CNT content.

### 4.2.5 Microstructural analysis

Microstructures at the crack faces of Si-C-N/CNT nanocomposites after fracture toughness measurement were investigated by a SEM. The pure Si-C-N material exhibited only a flat featureless structure in accordance with the amorphous nature of the material. Concerning the CNT nanocomposites, there is a big difference observed between both nanocomposites containing 2 mass % of different CNTs as shown in Fig. 4.25. In the type A nanocomposite (Fig. 4.25a), CNTs appear to be pulled out and bridged structures at the crack faces, whereas no CNTs are observed in the type B case (Fig. 4.25b) similar to the pure Si-C-N material. Further analyses were performed on the matching fracture surfaces created during fracture toughness measurement. Fig. 4.26a reveals a typical amorphous feature of the pure Si-C-N material. In the type A-CNT nanocomposites shown in Fig. 4.26b and c, besides some CNTs pulled out from the matrix (marked X), the corresponding holes (marked X′) are also observed at the opposite face. Furthermore, a few broken CNTs can be determined in pairs (Y and Y′) at the both surfaces. That is, two CNT features of pulled out and broken are identified on the fracture surface of the type A-CNT nanocomposites. On the other hand in the case of the other nanocomposite shown in Fig. 4.26d and e, only highly distributed dark parts are observed instead of pulled out CNTs. These are considered as the parts of broken CNTs, which indicate a deterioration of the defined CNTs structure in the matrix during thermolysis.

Fig. 4.27 shows a TEM micrograph of the Si-C-N/CNT nanocomposite containing 2 mass % type A-CNT. It can be seen that the embedded CNTs in the matrix clearly reveal their multi-walled structure as in the initial state (see also Fig. 4.2b). This feature indicates the preservation of their mechanical nature in the nanocomposites after thermolysis. Moreover, no crevices can be observed at the interface between CNTs and the matrix revealing the existence of the well-bonded nature at the interface. Further TEM analysis was performed on the pulled out CNTs after fracture toughness measurement. The results shown in Fig. 4.28 typically reveal that there exists three types of pulled out CNTs at the fracture surface, that is, bare CNTs with preserving their original forms (Fig. 4.28a), torn up CNTs in their outer tubes (Fig. 4.28b) and CNTs adhered with the matrix layer (Fig. 4.28c). These different features are in accordance with the high strength of the embedded CNTs in combination with the well-bonded interface between CNTs and the matrix, as revealed by the presence of both pulled out and broken nanotubes. That is, both

strength of CNTs themselves and of interfacial bonding between CNTs and the matrix, which are important parameters for fiber-reinforced composites, are well-balanced in the type A-CNTs incorporated Si-C-N nanocomposites. Consequently, it is considered that the thermal stress induced in the nanocomposites is effectively transferred from the matrix to the CNTs via the matrix/CNT interface, which increases the fracture energy by the generation of interfacial debonding, CNT pulling out, bridging and breaking as well as the crack deflection and pinning effects at the embedded CNTs. On the other hand in the type B nanocomposites, the existence of CNTs and their boundary could not be clearly identified by TEM as well as SEM analysis. These features indicate the degeneration of CNTs nature in the matrix during thermolysis, which may be trace back to the amorphous nature of the type B-CNTs.

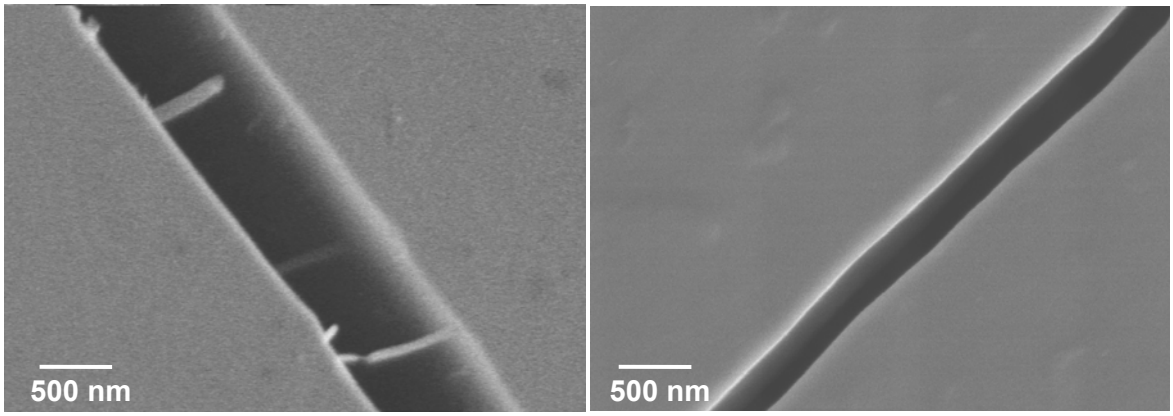


(a) (b)

Fig. 4.25. SEM micrographs at the crack face of the Si-C-N/CNT nanocomposites after fracture toughness measurement, (a) 2 mass % type A- and (b) 2 mass % type B-CNTs are incorporated.

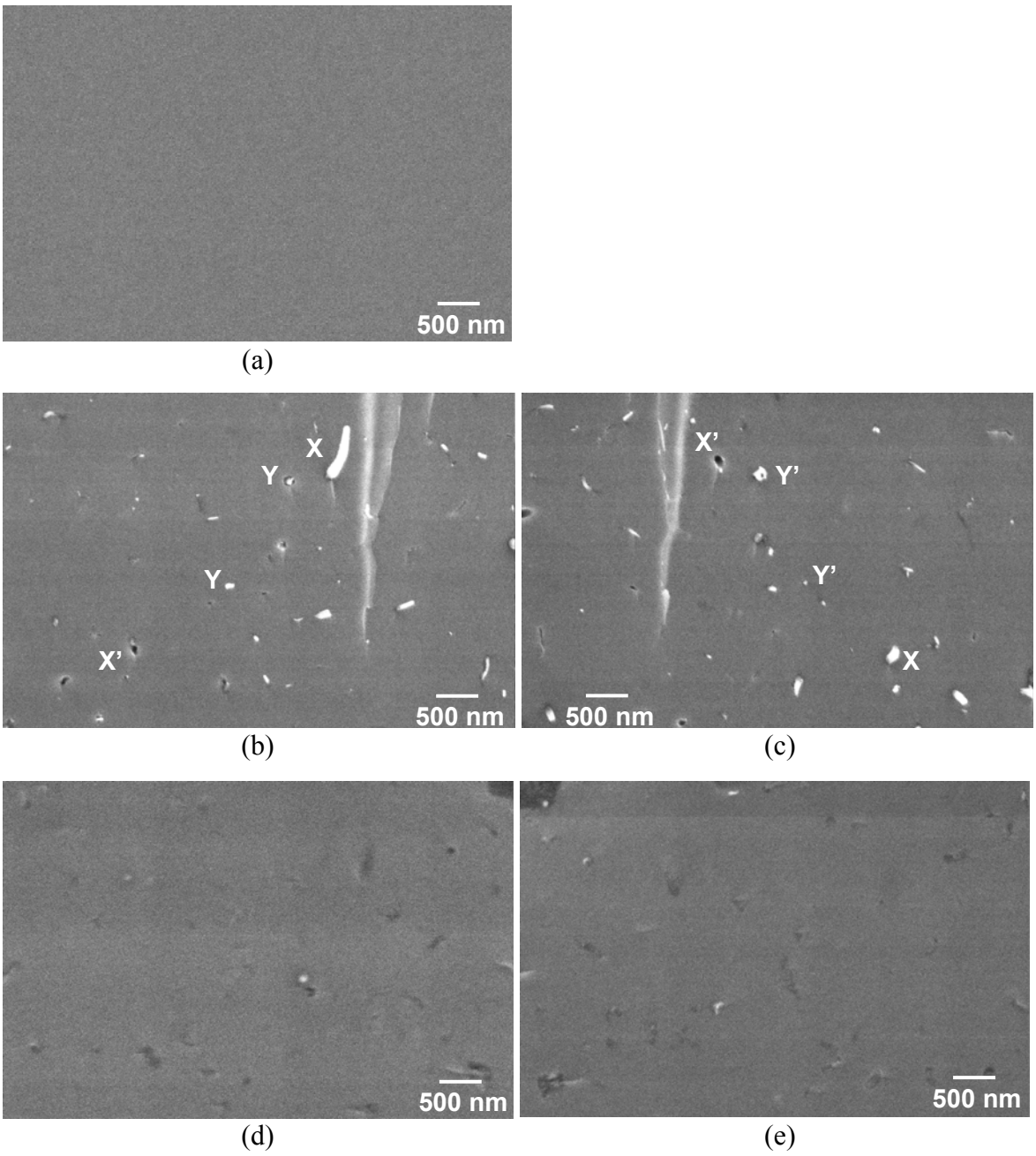


Fig. 4.26. SEM micrographs of the matching fracture faces of the Si-C-N/CNT nanocomposites after fracture toughness measurement, (a) pure Si-C-N material, (b and c) 2 mass % type A- and (d and e) 2 mass % type B-CNTs incorporated nanocomposite. The notes X-X' and Y-Y' are examples of a pulled out CNT and the corresponding hole and broken CNT pairs at both fracture surfaces, respectively.

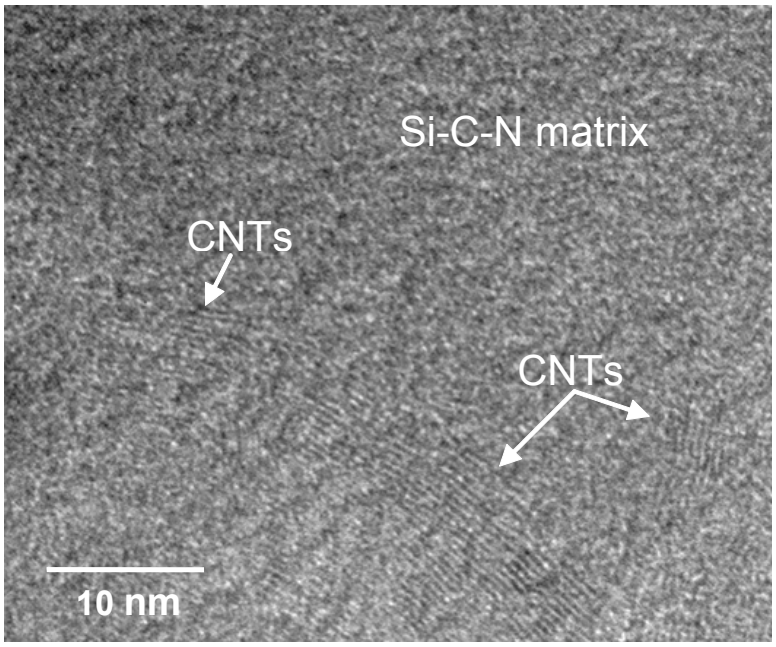


Fig. 4.27. TEM micrographs of the Si-C-N/CNT nanocomposite containing 2 mass % type A-CNTs. Arrows indicate embedded CNTs and the boundaries to the Si-C-N matrix.

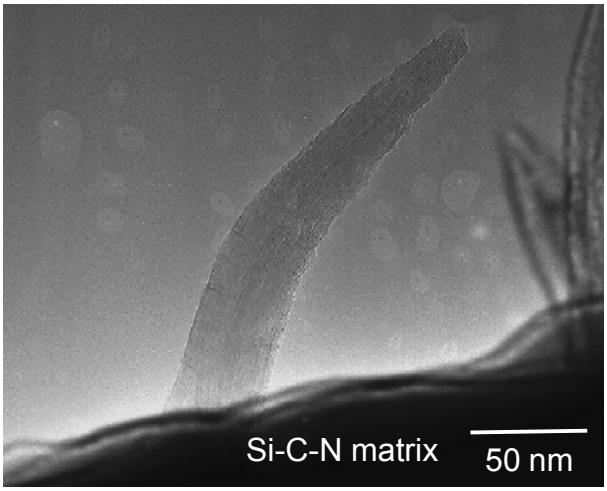


(a)

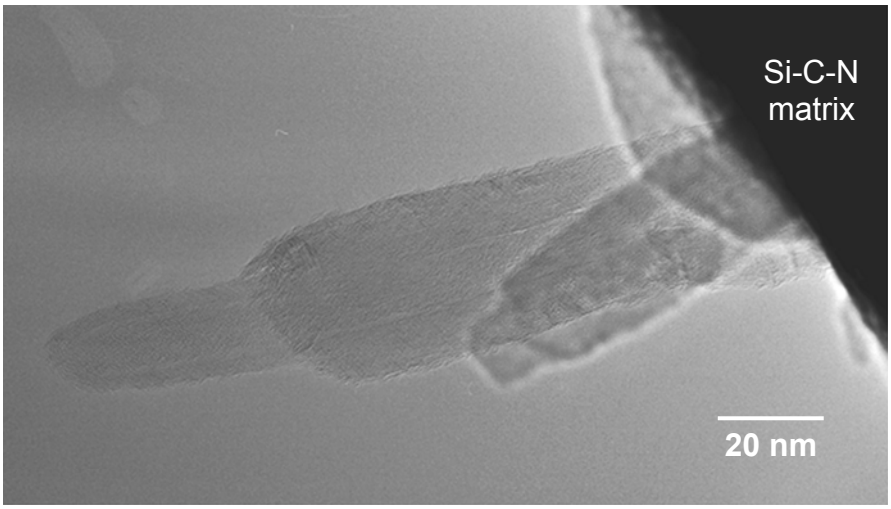


(b)

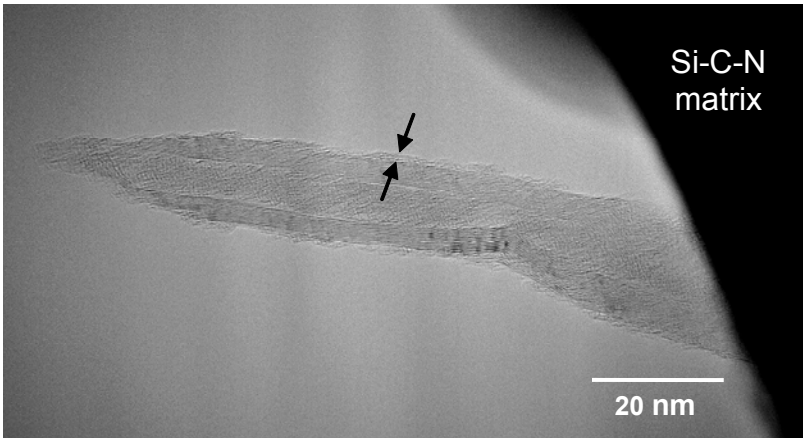


(c)

Fig. 4.28. TEM micrographs of the pulled out CNTs after the fracture toughness measurement of the Si-C-N/CNT nanocomposite containing 2 mass % type A-CNT. (a) a bare CNT, (b) torn up CNTs in the outer tubes and (c) a broken CNT adhered with the matrix layer are shown. Black arrows in (c) indicate the adhered matrix layer to the pulled out CNT.

## 4.3 Si-C-N/SWCNT nanocomposites

### 4.3.1 Sample preparation

The preparation process for single-wall CNT (SWCNT) incorporated Si-C-N nanocomposites is basically the same as the one applied for multi-wall CNT nanocomposites described in the section 4.2.1. In the following paragraphs, parameters which restrict on the preparation for SWCNTs incorporated Si-C-N nanocomposites are stated.

***Amount of CNTs on the casting process***

In the mixtures of MWCNTs and the Si-C-N precursor, an increase of the viscosity was observed with increasing the amount of CNTs. This phenomenon was revealed to be more remarkable for SWCNTs system. That is, the addition of 2 mass % SWCNTs into the precursor made the mixture pasty which could not be cast into a disk. Therefore, the amount of SWCNTs was reduced to 0.2 mass % which corresponded to one tenth of MWCNTs' case. Nevertheless, the viscosity of the mixture was similar to that of the precursor containing 2 mass % MWCNTs. The extreme viscosity increase of the SWCNT precursor mixture is considered to be due to the increase of interaction between precursor and CNTs, in which the larger specific surface area of SWCNTs (619 $m^2/g$) compared to MWCNTs (240 $m^2/g$) [04Li2] as well as the volume increase due to the density differences causes the significant effects on their viscosity behavior.

***Ceramization process: Effect of the heating rate on the thermolysis of the cross-linked materials***

In the case of Si-C-N/MWCNT materials, a slower heating rate of 25 °C/h for thermolysis was applied to prevent the nanocomposites from cracking. However, this condition still induced many cracks in the Si-C-N/SWCNT materials even with the CNT content of 0.2 mass %. Therefore, the heating rate was decreased to 10 °C /h. It can be mentioned that the necessity of slower heating rate also relates with the larger interaction between SWCNTs and Si-C-N precursor.

### 4.3.2 Fracture toughness behavior

The fracture toughness behavior of the SWCNTs incorporated Si-C-N nanocomposites was also measured by the thermal loading method [See Appendix 2 and 3 for the detail coefficients for their functions]. The calculated values of the

fracture toughness are shown in Fig. 4.29 in combination with the corresponding data obtained from the Si-C-N/MWCNT nanocomposites. It can be seen that the similar improvement of the fracture toughness can be obtained by the incorporation of SWCNTs into Si-C-N ceramics.

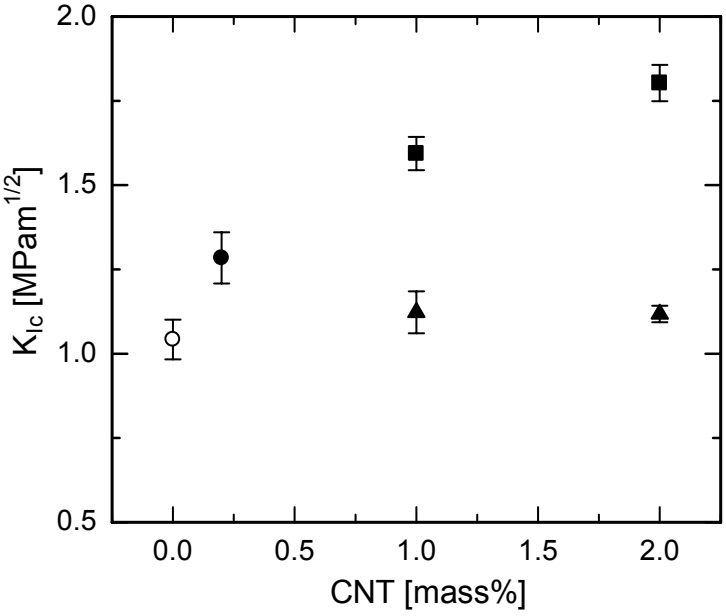


Fig. 4.29. Fracture toughness behavior of the Si-C-N/CNT nanocomposite containing 0.2 mass % SWCNTs (●). The other data are from the pure Si-C-N and the nanocomposites containing MWCNTs (○: pure, ■: type A, ▲:type B).

### 4.3.2 Microstructural analysis

SEM micrographs of the crack faces and fracture surfaces of the nanocomposites after fracture toughness measurement are shown in Fig. 4.30 and 4.31, respectively. As shown in the microstructure of MWCNT incorporated Si-C-N nanocomposites (Fig. 4.25), SWCNTs also lead to the formation of pulled out CNT structure at the fracture surfaces. It is considered again that these CNTs are responsible for the fracture toughness increase by the effect of fracture energy increase mentioned before (see section 4.2.5). However, as can be seen in Fig. 4.30, the distribution of SWCNTs in the matrix is not so homogeneous and, moreover, their large size in the diameter shown in Fig. 4.30 and 4.31 indicate the retention of their

bundled and deagglomerated structure in the matrix. Therefore, the sliding of bundles, which are bonded by weak van der Waals force, could be occurred instead of CNT breaking during crack propagation. This may cause the smaller gain of SWCNTs for the toughening effect. To obtain benefit of SWCNTs fully as reinforcements, debundle and deagglomeration of SWCNTs are important points to notice.

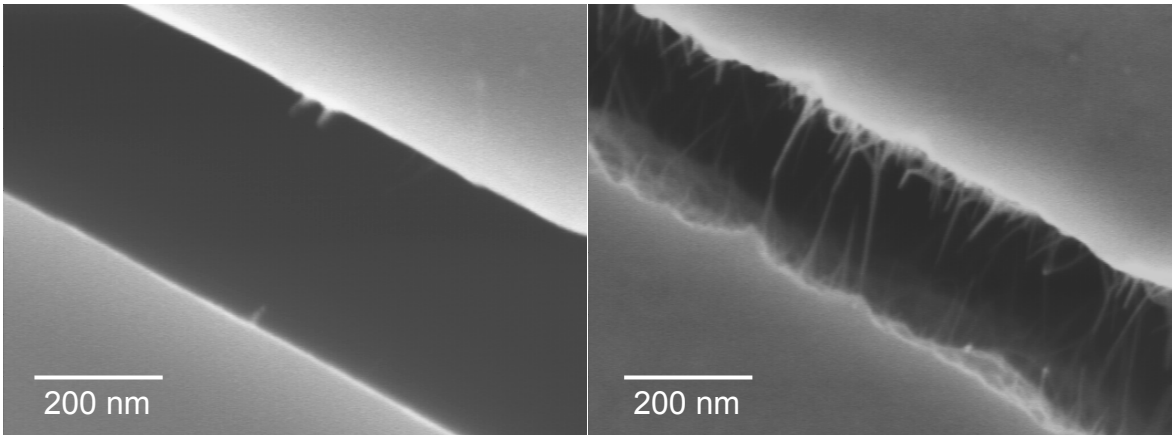


(a) (b)

Fig. 4.30. SEM micrographs at the crack faces of the Si-C-N/CNT nanocomposites containing 0.2 mass % SWCNT. Less CNTs (a) and agglomerated CNTs (b) can be seen in the matrix.

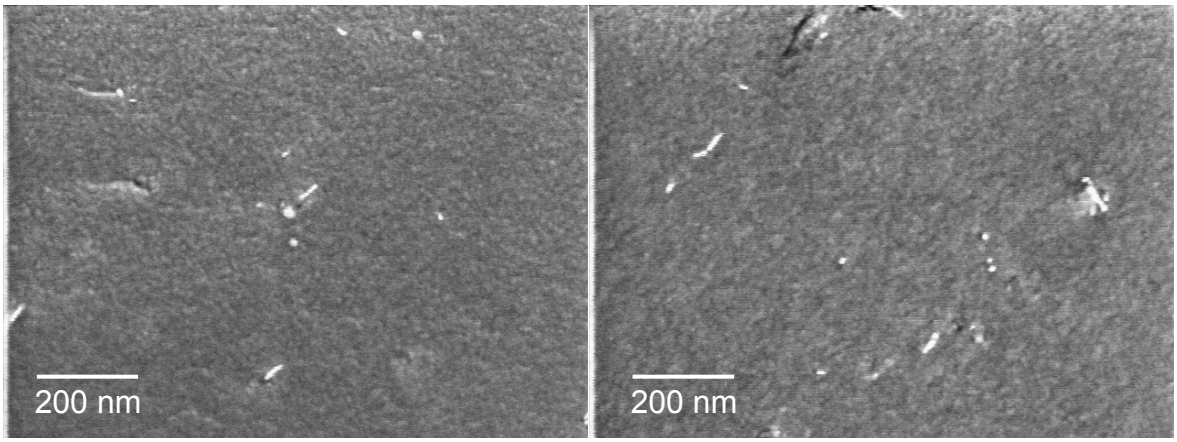


(a) (b)

Fig. 4.31. SEM micrographs of the fracture surfaces of Si-C-N/CNT nanocomposites containing 0.2 mass % SWCNTs.

## 4.4 Si-B-C-N/MWCNT nanocomposites

### 4.4.1 Sample preparation

At first, a casting process from the mixuture of oligo-vinylsilazane (OVS) and tris(methylsilylethyl)borane (TMBE) [See Fig. 2.5, 98Kam, 01Bil] was examined for the preparation of cross-linked Si-B-C-N precursor bodies. In this process, boron containing polysilazane is synthesized and solidified simultaneously during the hydrosilylation reaction of borane and silazane. To obtain rigid cross-linked bodies in disc shapes, several parameters for cross-linking such as heat temperature (120 - 250 °C), time (1 - 40 h), mold types (open, closed) and their materials (Teflon, polyethylene and polished graphite) were investigated. Fig. 4.32 shows the representative cross-linked bodies produced in an open mold (a) and a closed mold (b). The material (a) consisting of pure Si-B-C-N precursor, where the cross-linking was performed at 180 °C for 5 h in a Teflon mold, was very soft but seemed to be pore free indicated by its high translucency. However, besides the deformation of the sample during cooling, a weight loss of ca. 40 mass % was observed after cross-linking. The loss is considered to be due to the evaporation of raw materials, in which the deviation of the chemical composition from the designed Si-B-C-N ceramics was observed. On the other hand, the cross-linking in the closed metal mold suppressed the evaporation of mixture to ca. 2 mass % in CNTs incorporated precursor (Fig. 4.32b, cross-linked at 210 °C for 20 h in the combination of inner Teflon and outer metal mold). However, the cross-linked body appeared to possess many cracks, which

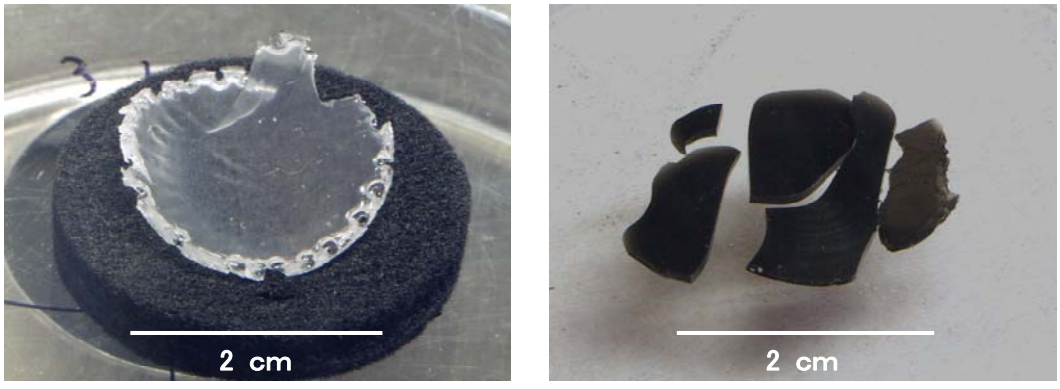


(a) (b)

Fig. 4.32. Representative cross-linked bodies of the Si-B-C-N precursors derived from the casting process, (a) pure Si-B-C-N precursor cross-linked at 180 °C for 5 h in an open mold and (b) Si-B-C-N/CNT (2 mass %) precursor cross-linked at 210 °C for 20 h in a closed metal mold.

also led the body into pieces during detaching from the Teflon mold. In addition, the brittle nature of the cross-linked Si-B-C-N precursor as well as the strong adherent nature to the Teflon mold turned out to be serious problems for the preparation of rigid cross-linked samples with designed shapes.

Therefore, a boron-containing polysilazane, so-called T2-1 [See Fig. 2.4, 96Rie], and the process involving a cross-linked powder preparation and a warm pressing were applied to the preparation of disc shaped cross-linked samples. Fig. 4.33 shows the overall preparation process for T2-1 derived Si-B-C-N/CNTs nanocomposites. MWCNTs of type A and the amount of 2 mass % were representatively adopted for the reinforcement of Si-B-C-N materials because of their effectiveness realized on the fracture toughness behavior of Si-C-N/CNT nanocomposites. Characterization of the pure Si-B-C-N material was also performed to make a comparative study.

***Deagglomeration process: Effect of the solvents on the dispersion of CNTs***

The T2-1 precursor for Si-B-C-N ceramics can be produced in a solution of toluene or THF [Rie96]. Prior to mix CNTs with the T2-1 precursor solution, effectiveness of the solvents on the deagglomeration and dispersion of CNTs was investigated. Fig. 4.34 shows the CNT suspension in toluene and THF solvents settled 24 h after sonication by the ultrasonic probe for 20 min. It is obvious from the picture that the precipitation of CNTs occurred in toluene but not in THF. These phenomena are considered to be due to the difference in the polarity between THF and toluene. That is, CNTs are stable in the solvent possessing high polarity (THF) as dispersed state. Therefore, THF was used as the solvent for both CNTs suspension and T2-1 precursor.

***Mixing and cross-linking***

After the sonication of CNTs in THF for 20 min by the ultrasonic probe under argon flowing atmosphere, the suspension was mixed with T2-1 THF solution and stirred by a magnetic stirrer in an argon atmosphere. The solvent of THF was then removed by evacuating and heating up to ~ 5 Pa and ~ 80 °C in an oil bath under stirring. The obtained CNTs dispersed T2-1 solid was cross-linked at 250 °C for 1h in an argon flowing atmosphere and followed by 350 °C for 5 h under evacuating in order to complete cross-linking and remove low molecular species. Fig. 4.35 shows the

pictures of T2-1/CNT mixture in THF (a) and the corresponding cross-linked materials of T2-1/CNT (b).

***Milling, warm pressing and thermolysis***

The obtained mixture of cross-linked T2-1/CNT solids was pulverized by a tungsten carbide mortar (Analysette, Fritsch) and sieved with a mesh sieve (80 μm open size). To form green bodies in a disc shape, the powder mixtures were placed in a graphite mold and warm-pressed at 400 °C for 1h in a vacuum under a uniaxial pressing of 50 MPa. Fig. 4.36 shows photographs of the warm pressing furnace and the graphite mold, where the heat is directly applied to the mold by alternative electrical current. Finally, the green bodies were embedded in silicon nitride powders in an alumina crucible and thermolyzed in an argon flowing atmosphere at temperature up to 1400 °C with a heating rate of 25 °C/h up to 800 °C and 60 °C/h above it. The samples were held for 2 h at the maximum temperature and cooled down with a rate of 300 °C/h.

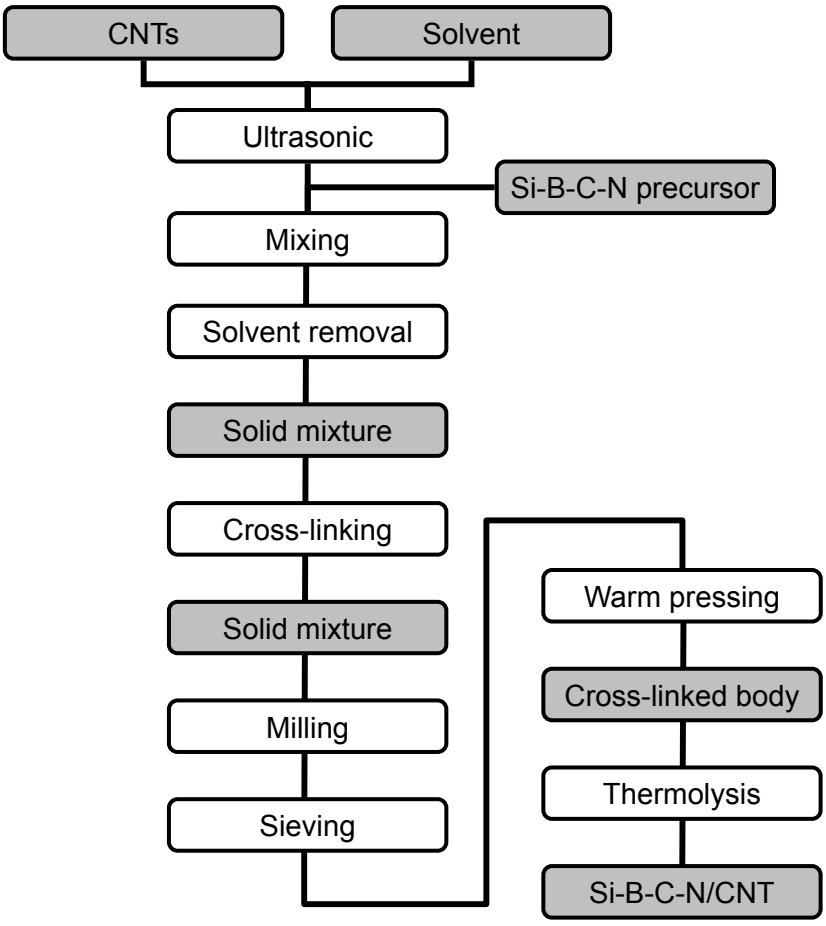


Fig. 4.33. Preparation process for the Si-B-C-N/CNT nanocomposites.

(a) (b)

Fig. 4.34. A photograph of the CNT suspensions in (a) toluene and (b) THF. Both suspensions were settled 24 h after ultrasonic dispersion.

(a) (b)

Fig. 4.35. Photographs of the T2-1/CNT mixture in THF (a) and the corresponding cross-linked material (b) (black colored). A white material in (b) is the pure Si-B-C-N

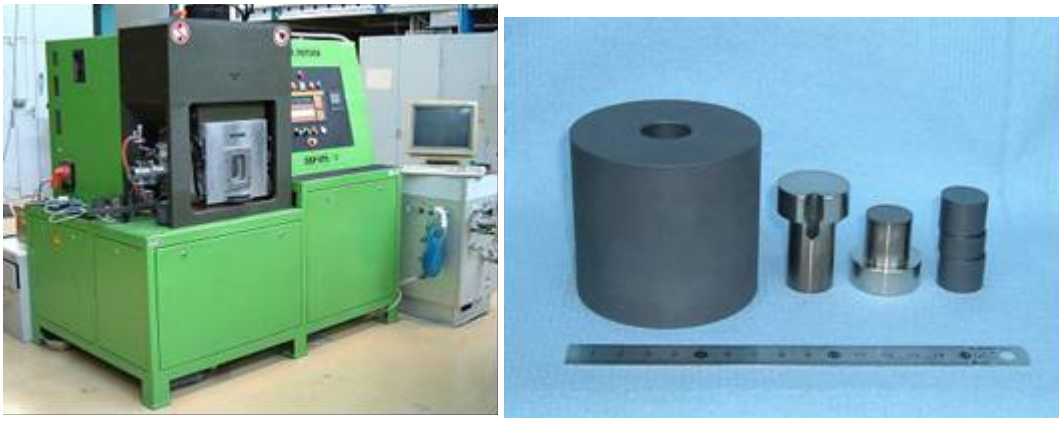

(a) (b)

Fig. 4.36. Photographs of the warm pressing furnace (a), and the graphite mold and spacers with metal punches (b).

### 4.4.2 Crystallization behavior

The X-ray diffraction profiles of the thermolysed materials at 1000, 1200, 1300 and 1400 °C are shown in Fig. 4.37. The pure Si-B-C-N material thermolyzed at 1000 °C is nearly amorphous and the materials gradually exhibit silicon carbide peaks (noted ●) with increasing thermolysis temperature. Besides the silicon carbide peaks, a broad peak around 2 θ = 25 ° (○) is observed. This peak is considered to be a multiple peak consisting of graphite (d=3.37563 Å, 2 θ = 26.4 °, JCPDS No. 41-1487), boron nitride (d=3.32813 Å, 2θ = 26.8 °, JCPDS No.34-421) and their turbostratic phase (B-C-N). In the case of 2 mass % CNT incorporated Si-B-C-N materials, silicon carbide peaks already appear at the thermolysis temperature of 1000 °C. The peak intensity becomes much stronger than the pure Si-B-C-N materials with increasing thermolysis temperatures. In addition, a multiple peak observed in the pure Si-B-C-N materials (2 θ = 25 °) also appears at slightly shifted position of 2 θ = 26 ° with higher intensity than the pure materials. As the results, it is found that the CNTs have effects to promote crystallization of the Si-B-C-N matrix to silicon carbide and of the graphite and boron nitride related phases.

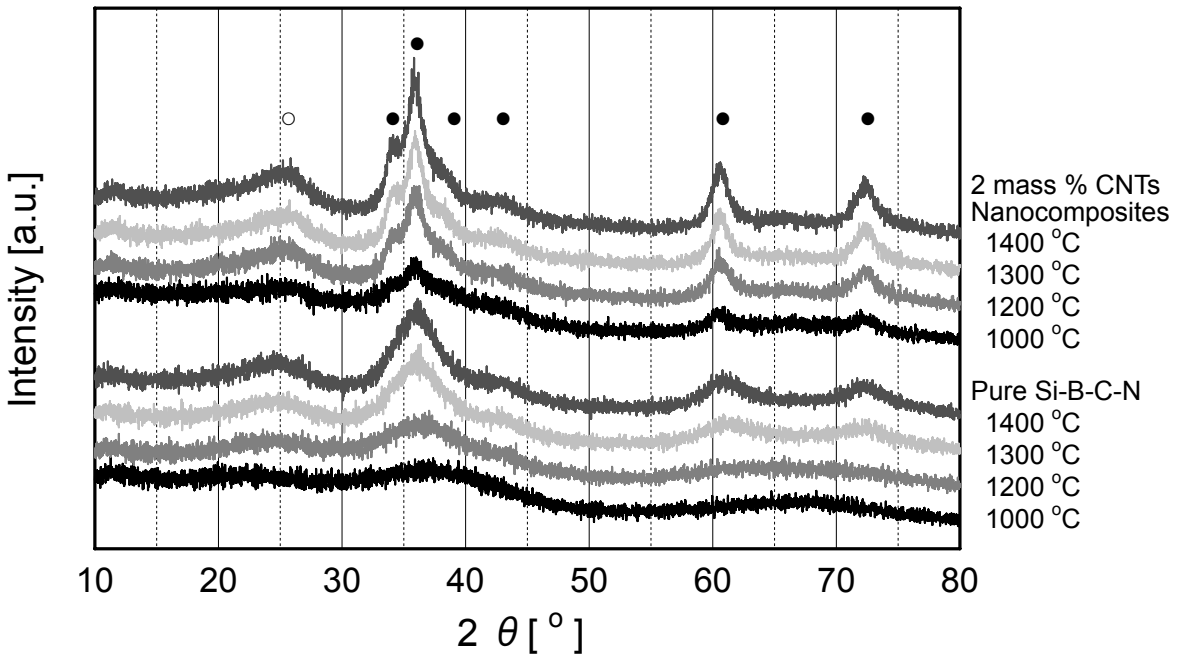


Fig. 4.37. X-ray diffraction profiles of the pure Si-B-C-N and 2 mass % CNT incorporated Si-B-C-N materials with different thermolysis temperatures. Indications are corresponding to silicon carbide peaks (●) and a multiple peak consisting of graphite, boron nitride and boron-carbon-nitride (B-C-N) phases (○).

### 4.4.3 Thermal stability and chemical analysis

The thermogravimetric behavior of Si-B-C-N and Si-B-C-N/CNT nanocomposites thermolysed at different temperatures (1000, 1300 and 1400 °C) is shown in Fig. 4.38. In this diagram, the weight loss behavior can be divided into two groups. The better group which is in accordance with the pure Si-B-C-N materials gives small weight losses of ca. 4 – 6 mass % around 1500 – 1600 °C but possess high thermal stability up to 2000 °C as can be seen on their plateaus within 1600 – 2000 °C. The other group of Si-B-C-N/CNT nanocomposites exhibits gradual weight decrease above 1500 °C, where the total losses become ca. 13 – 18 mass % at 2000 °C. Consequently, it is found that the thermal stability of the Si-B-C-N/CNT nanocomposites becomes worse than that of pure Si-B-C-N materials.

The chemical compositions of Si-B-C-N materials thermolyzed at 1000 °C and 1400 °C are summarized in Table 4.4. Besides the increase of carbon contents in the Si-B-C-N/CNT nanocomposites, there can be slight deviation of oxygen and nitrogen contents observed in the both nanocomposites compared to the pure Si-B-C-N. Concerning the oxygen increase, non-desorbed oxygen and/or moisture of CNTs during vacuum heating are considered to be a reason for it. Moreover, the moisture carrying by THF solvent might be occurred during the sonication of CNTs under a flowing argon atmosphere. However, both deviations of oxygen and nitrogen contents are quite small in contrast with the difference in the observed thermal stability behaviors. Therefore, it can be mentioned that the deterioration of the thermal stability of Si-B-C-N/CNT nanocomposites is not due to their chemical compositions but their microstructures. This is the essential issue for the Si-B-C-N/CNT nanocomposites which should be solved so as to obtain full performance of both CNTs and Si-B-C-N characteristics.

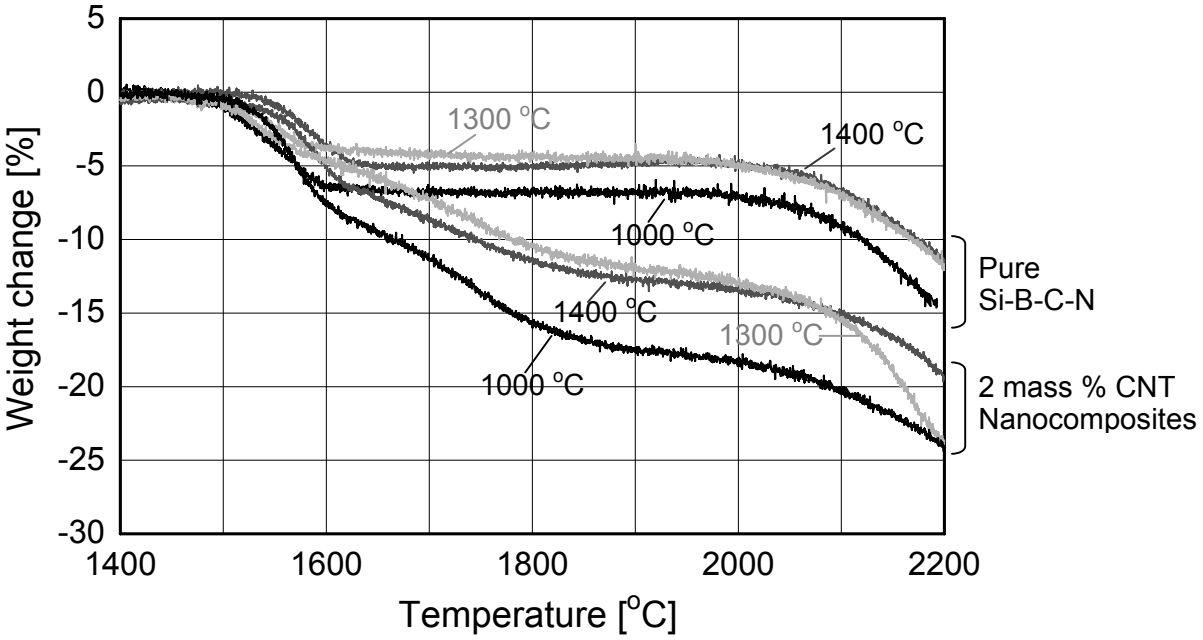


Fig. 4.38. Thermogravimetric behavior of the pure Si-B-C-N and 2 mass % CNT incorporated Si-B-C-N materials with different thermolysis temperatures.

Table 4.4. Analyzed chemical composition of Si-B-C-N materials and their estimated phase compositions (mass %).

| Elements | Pure Si-B-C-N | | Si-B-C-N/CNTs 2 mass % | |
|---|---|---|---|---|
| | 1000 °C | 1400 °C | 1000 °C | 1400 °C |
| Si | 44.8 | 44.2 | 44.0 | 43.0 |
| B | 5.40 | 5.40 | 5.06 | 5.50 |
| C | 31.1 | 31.1 | 31.9 | 31.9 |
| N | 17.8 | 17.9 | 16.6 | 16.3 |
| O | 0.75 | 0.80 | 1.34 | 1.80 |
| H | 1.00 | 0.60 | 0.84 | 0.50 |

### 4.4.4 Microstructural analysis of embedded CNTs by TEM

TEM micrographs of the Si-B-C-N/CNT nanocomposites thermolyzed at 1000 °C are shown in Fig. 4.39. In these micrographs, two different areas corresponding to an amorphous area (Fig. 4.39a) and a crystallized one (Fig. 4.39b and c) are shown. From these analyses, it can be realized that the amorphous area of the CNTs nanocomposites tends to possess no or less embedded CNTs in the matrix. On the other hand, the crystallized area which was confirmed to include a silicon carbide phase by an electron diffraction analysis involves many embedded CNTs in the matrix. These local differences in the matrix crystallinity and the relation to CNTs give further proof of the acceleration effect of CNT for the crystallization of Si-B-C-N matrix (See the XRD behavior in Fig. 4.37). Consequently, it is considered that the CNTs possess the effects to act as templates and/or to generate nucleation sites for the crystallization of the Si-B-C-N matrix. These kind of templating or nucleating effects of CNTs on the matrix crystallization have been widely reported on the polymer-based CNTs nanocomposites such as polypropylene, polyvinyl alcohol, ethylene-vinyl acetate copolymer systems and so on [03Val, 04Pro, 04Li1, 01Cze]. The detailed microstructural analysis performed by Czerw et al [01Cze] demonstrated a structural relationship between CNT and the surrounding polymer structure in the poly(propionylethylenimine-co-ethylenimine)/SWCNT system, where the crystalline state of the polymer were directly determined by the underlying CNT's chirarity like epitaxicial growth. The exact mechanism for the Si-B-C-N/CNT nanocomposites is still unclear but the high surface area nature of CNTs and their interaction with the matrix will contribute to the acceleration of crystallization for the Si-B-C-N matrix.

Microstructural studies on the Si-B-C-N materials annealed at 1800 °C for 50 h [96Jal, 01Sei, 01Bil] revealed their characteristic morphologies which explain the mechanism for the extraordinary thermal stability of Si-B-C-N materials at high temperature. According to their studies, the generation of the turbostratic B-C-N layers in the matrix has two roles for the stabilization of silicon nitride component at high temperature. One is the reduction of the carbon activity against the reaction with silicon nitride by involving carbon atoms into the boron nitride layers (B-C-N layers). The other is the encapsulation of the silicon nitride component by the B-C-N layers which provide barriers for the nitrogen diffusion leading to the increase of internal nitrogen partial pressure for silicon nitride. Judging from the observed deterioration in the thermal stability of Si-B-C-N/CNT nanocomposites, it can be

mentioned that the encapsulation of the silicon nitride component by the B-C-N layers has not grown in the nanocomposites. Furthermore, the XRD intensity increase observed at 2 θ = 26 ° (Fig. 4.37) which corresponds to the multiple peak of graphite, boron nitride and their turbostratic B-C-N phase in the pure materials (2 θ = 25 ° ) suggests that the separation and crystallization of graphite and boron nitride may partially proceed in the Si-B-C-N matrix. Therefore, the graphite component will give rise to reaction with silicon nitride generating nitrogen gas (Eq.4.1) followed by collapse of the structure. It can be concluded that the incorporation of CNTs into Si-B-C-N materials accelerates the crystallization of the matrix into silicon carbide, boron nitride and graphite phases accompanied by the suppression of their characteristic B-C-N morphology formation in the matrix.

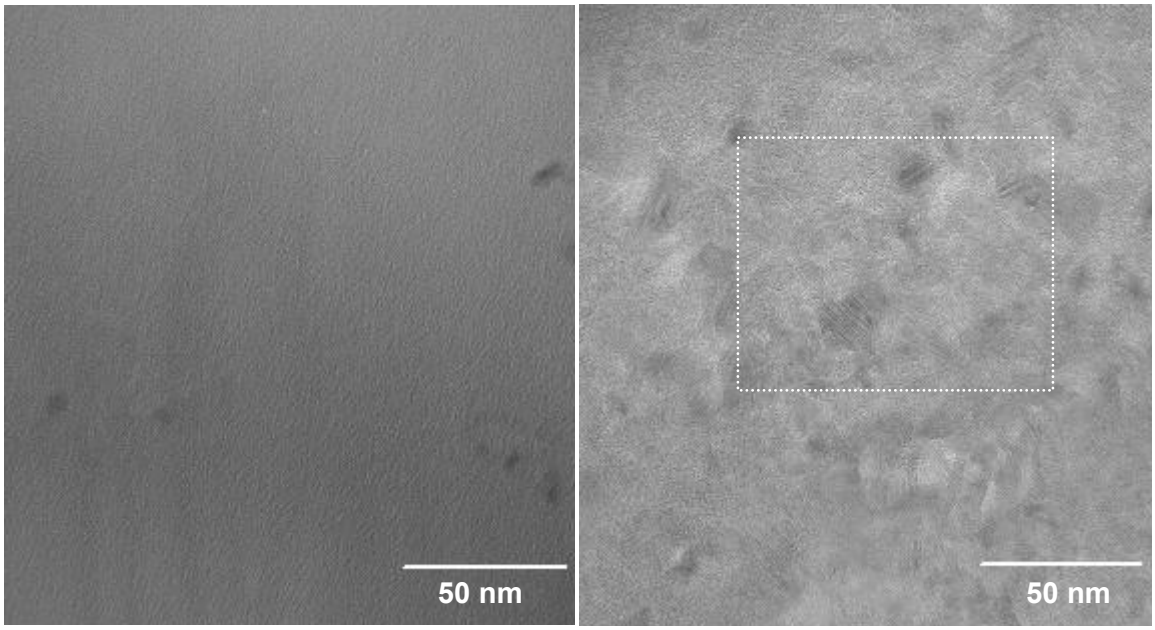


(a) (b)

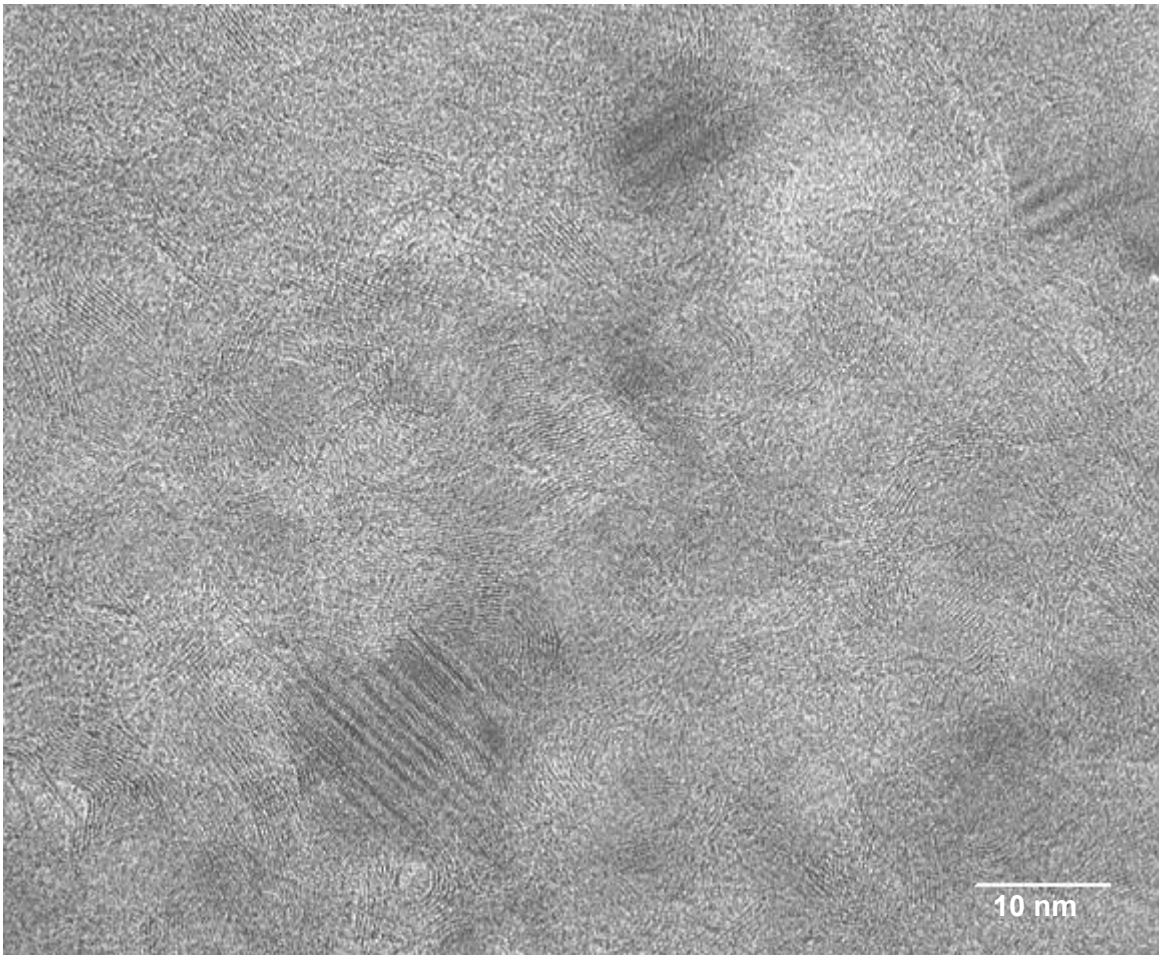


(c)

Fig. 4.39. TEM micrographs of the Si-B-C-N/CNT nanocomposite corresponding to the amorphous area (a) and the crystallized one (b). An enclosed part of (b) is magnified on (c). The embedded CNTs can be identified at the crystallized matrix area (b and c).

### 4.4.5 Fracture toughness behavior

Before proceeding to the fracture toughness behavior of the Si-B-C-N materials, the optical microscopic images of the polished surfaces of pure Si-B-C-N and nanocomposites containing 2 mass % CNTs both thermolysed at 1000 °C are representatively shown in Fig. 4.40 (a) and (b). As can be seen in the pictures, there exists some crescent shape pores and cracks in both materials. These defects will be caused by an imperfect warm pressing of cross-linked powders and/or low molecular weight species of the precursor which evaporate or decompose at lower temperature during thermolysis. Moreover, it was observed that these defects sometimes cause cracking during the polishing process as well.

Owing to these defects, the measurement of the fracture toughness becomes more difficult with respect to a quantitative evaluation. Indeed, some samples could not be induced a crack by thermal loading method, where the stress relaxation by micro cracking would be occurred. Fig. 4.41 reveals the obtained fracture toughness behavior of the pure Si-B-C-N material (a) and the nanocomposite containing 2 mass % CNT (b) both thermolysed at 1000 °C. As can be seen in the diagrams, each material possesses nearly constant fracture toughness during crack propagation. However, different CNT nanocomposites (noted # 1 and # 2) in Fig. 4.41b reveal a rather big deviation in their fracture toughness, where the averaged values are 1.3 and 1.6 $MPam^{1/2}$, respectively. Moreover, the crack propagation of the sample # 2 is not steady as can be seen in the missing data at the crack length of ca. 4.0 – 4.4 x $10^{-3}$ m and above 5.1 x $10^{-3}$ m. In these regions, the crack arrest by the surrounding

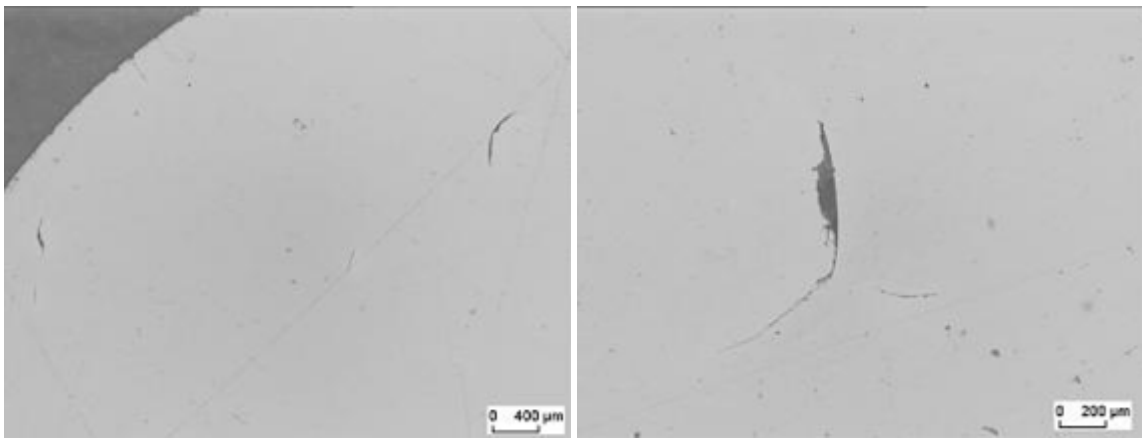


(a) (b)

Fig. 4.40. Polished surfaces of the pure Si-B-C-N material (a) and Si-B-C-N/CNT nanocomposite containing 2 mass % CNT (b) showing some defects in the materials.

defects would be occurred. Therefore, it is concluded that the quality of examined Si-B-C-N materials is not sufficient for the measurement of fracture toughness by the thermal loading technique.

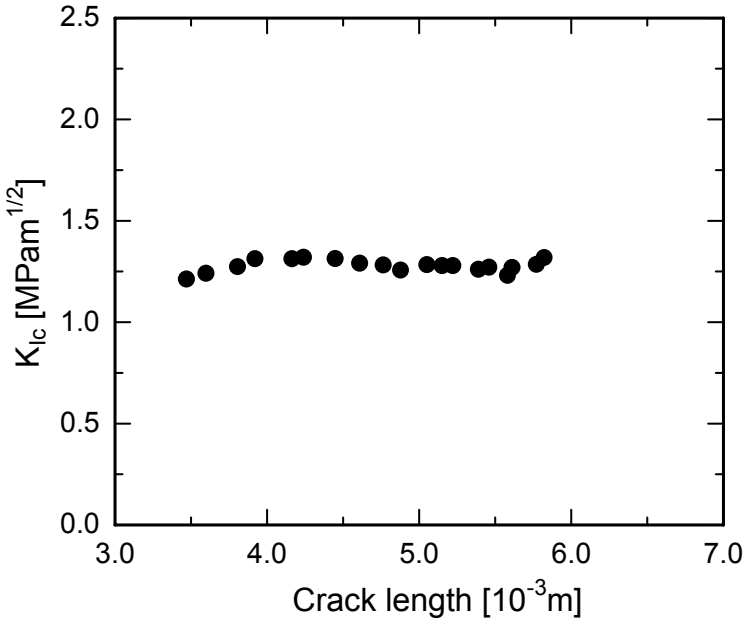


(a)

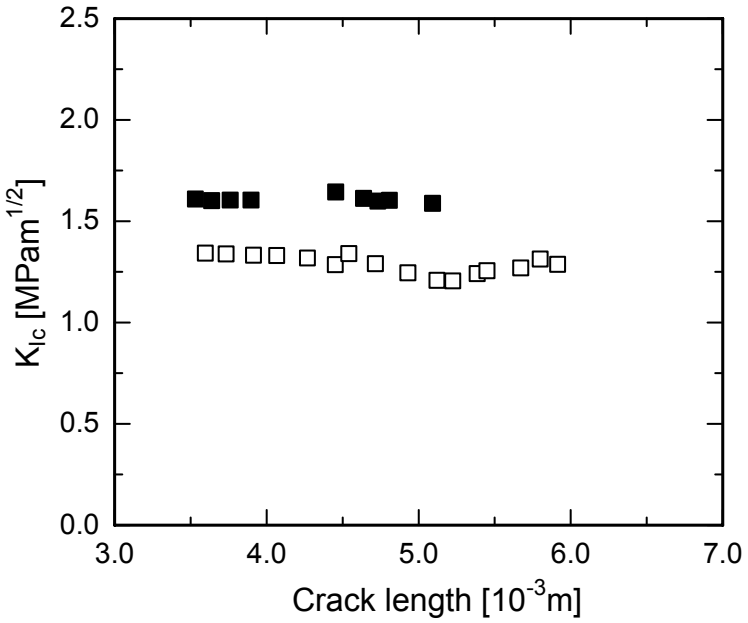


(b)

Fig. 4.41. Fracture toughness behavior of pure Si-B-C-N material (a) and Si-B-C-N/CNT nanocomposites containing 2 mass % CNTs (b) measured by the thermal loading technique. The notes, # 1 and # 2, in (b) indicate the data from different samples.

### 4.4.6 Microstructural analysis

Microstructural analyses on the pure S-B-C-N and the nanocomposites containing 2 mass % CNT were performed at the crack faces (Fig. 4.43) and the fracture surfaces (Fig. 4.44) created during fracture toughness measurement. It can be seen that some CNTs are pulled out and bridged up at the crack faces of the CNT nanocomposite (Fig. 4.43b). The pulled out CNTs are also observed at the fracture surfaces of the nanocomposite with some holes which would be generated by pulled out CNTs (Fig. 4.44b). These microstructural features are quite similar to the Si-C-N/CNT nanocomposites possessing toughening effect. Therefore, it is considered that the Si-B-C-N materials can be essentially reinforced by the CNT incorporation.

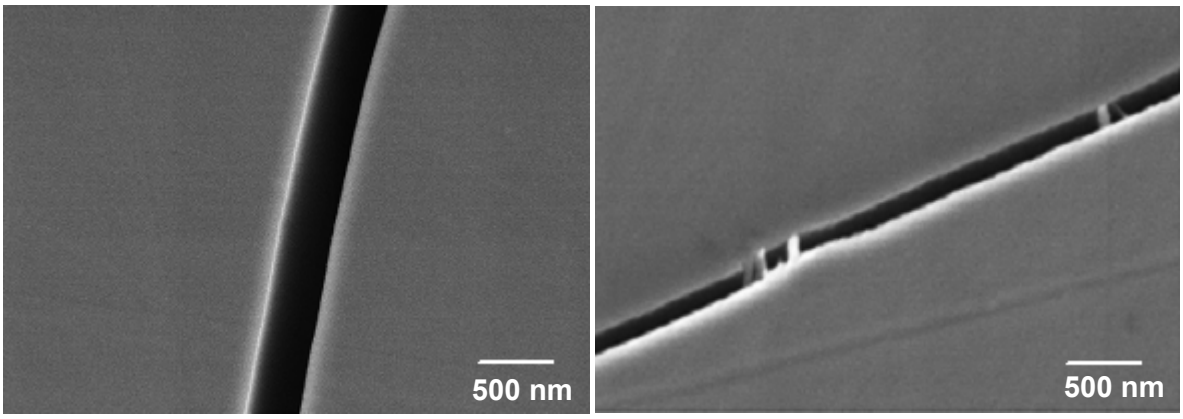


(a) (b)

Fig. 4.43. SEM micrographs at the crack faces created during fracture toughness measurement, (a) pure Si-B-C-N material and (b) Si-B-C-N/CNT nanocomposite containing 2 mass % CNT. Both materials were thermolysed at 1000 °C.

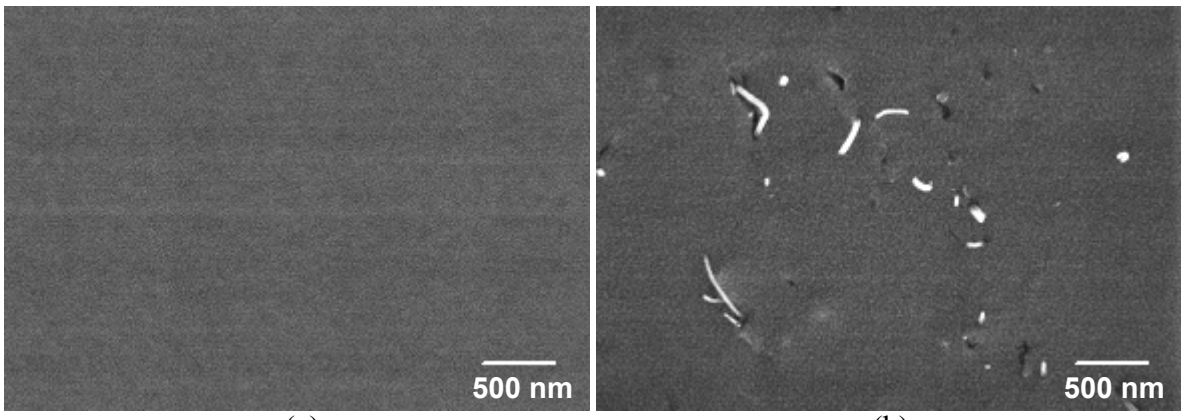


(a) (b)

Fig. 4.44. SEM micrographs at the fracture surfaces created during fracture toughness measurement, (a) pure Si-B-C-N material and (b) Si-B-C-N/CNT nanocomposite containing 2 mass % CNT. Both materials were thermolysed at 1000 °C.

Fig. 4.45 shows SEM micrographs at the fracture surfaces of the pure Si-B-C-N materials and the CNTs nanocomposites with different thermolysis temperatures at 1200, 1300 and 1400 °C. In these micrographs, the matrix roughening due to the crystallization can be observed with increasing thermolysis temperature. This tendency is more remarkable in the CNTs nanocomposites because of their accelerative crystallization effect on the Si-B-C-N matrix. Concerning the CNT's features at the fracture surfaces, a transition of their fracture form from pulled out (1000 °C, Fig 4.44b) to broken (1400 °C, Fig. 4.45f) is observed with increasing thermolysis temperature. Fig. 4.46 is the further microstructural features obtained by TEM analysis at the fracture surfaces of the nanocomposites thermolyzed at 1000 °C and 1400 °C. In the nanocomposites thermolyzed at 1000 °C, long pulled out CNTs with relatively definite structure can be observed. On the other hand, CNTs appear to be heavily torn up forms with very short pulled out in the nanocomposite thermolyzed at 1400 °C. According to these microstructures, the fracture behavior of the embedded CNTs in the matrix are schematically considered in Fig. 4.47 based on the relative strength of embedded CNTs ($S_{CNT}$) to the interfacial bonding between CNTs and the matrix ($S_{IB}$). Fig. 4.47a shows the case where the strength of the embedded CNTs are much higher than that of the interfacial bonding, $S_{CNT} >> S_{IB}$. In this case, the stress induced in the matrix can not be transferred to the embedded CNTs because of low interfacial bonding leading to the pulled out CNT structure without fracturing in their tube. If the both strength is comparable, $S_{CNT} \approx S_{IB}$, both pulled out and broken CNTs will appear on the fracture surfaces as in Fig. 4.47b. This case is considered to be the best condition for the nanocomposites because the stress in the matrix can be effectively transferred to the CNTs via the interface. In case of the higher interfacial strength to the CNTs, $S_{CNT} << S_{IB}$, the broken CNTs without pulling out will be in majority as in Fig. 4.47c. In the last case, the most probable reason for the lowered CNT strength is due to the excess interfacial reaction occurred between CNTs and the matrix during material preparation, in which CNTs will be damaged and lost their integrity. In the case of the observed CNTs' morphologies of Si-B-C-N/CNT nanocomposites (Fig. 4.44 and 4.45), it can be mentioned that the thermolysis temperature of 1400 °C is too high for CNTs to preserve their strength in the matrix. Also, the CNT nanocomposite thermolysed at 1000 °C seems to possess room for strengthening the interfacial bonding further. Therefore, it is considered that the optimum thermolysis temperature for toughening

will be in their intermediate, for instance, 1100 – 1300 °C for the Si-B-C-N/CNT nanocomposites in this system.

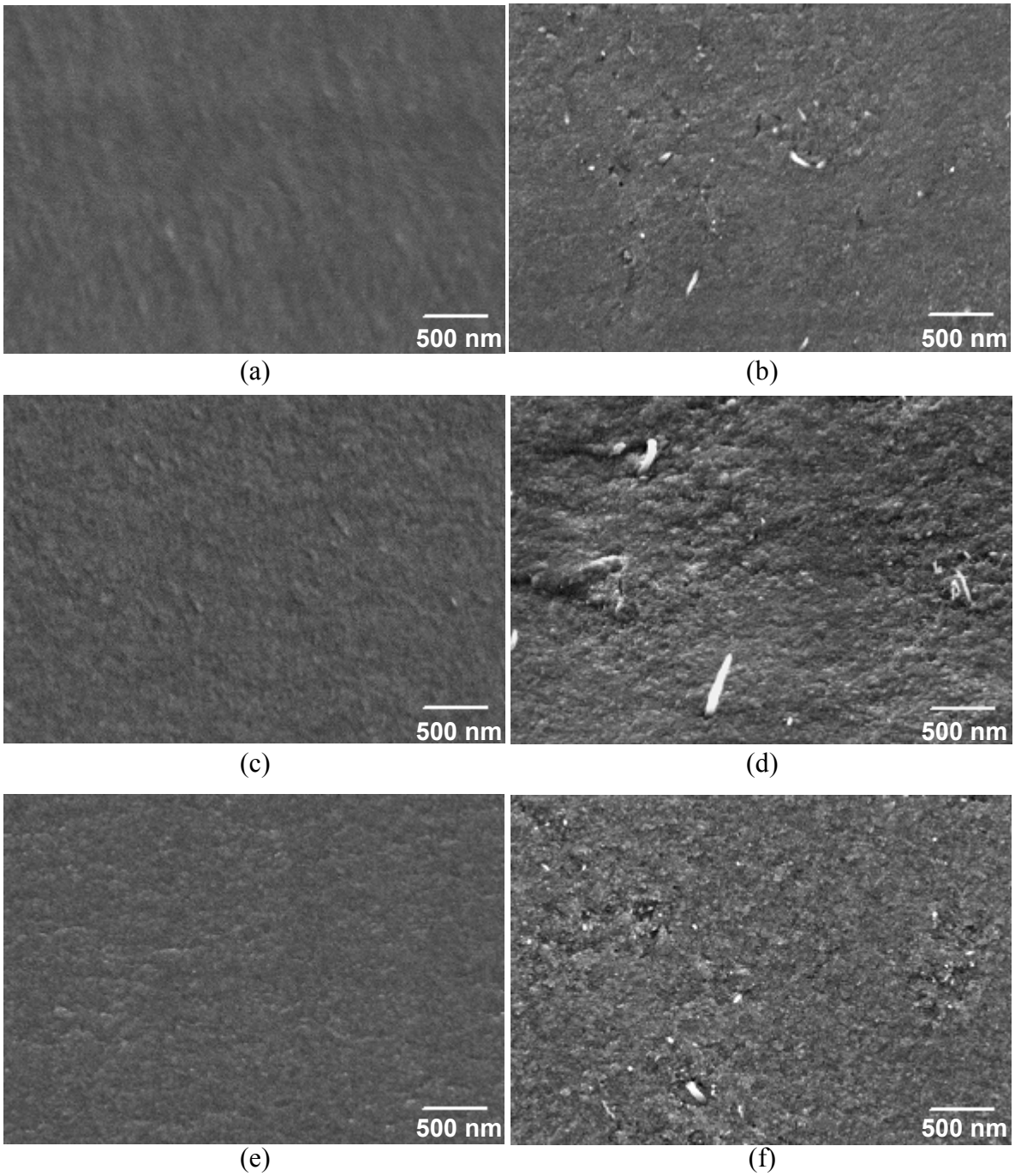


Fig. 4.45. SEM micrographs at the fracture surfaces of the pure Si-B-C-N material thermolyzed at (a) 1200 °C, (c) 1300 °C and (e) 1400 °C, and the Si-B-C-N/CNT nanocomposites (2 mass %) thermolyzed at (b) 1200 °C, (d) 1300 °C and (f) 1400 °C.

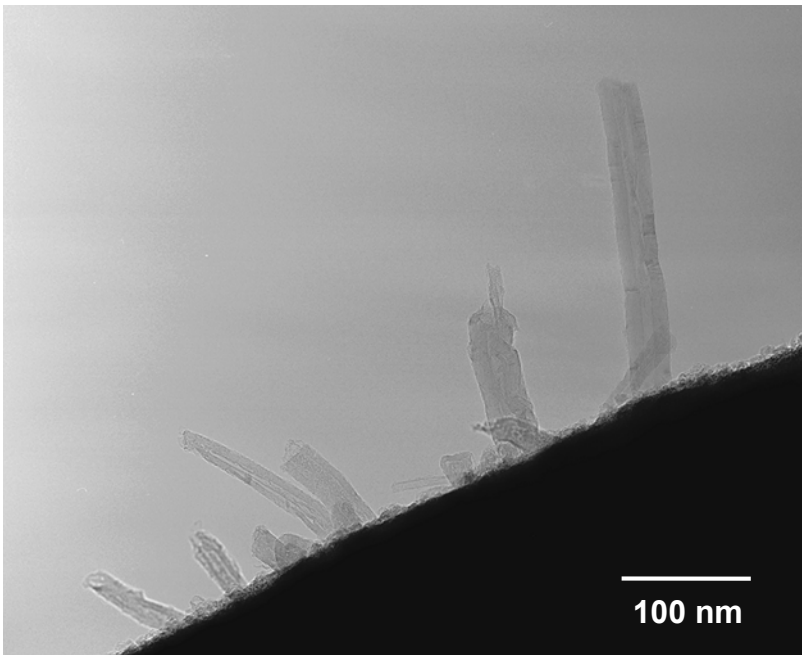


(a)

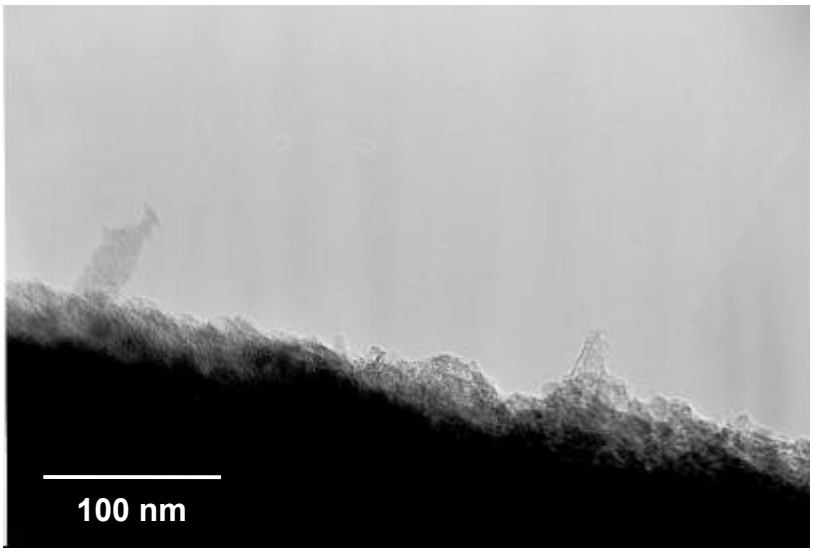


(b)

Fig. 4.46. TEM micrographs at the fracture surfaces of the Si-B-C-N/CNT nanocomposites (2 mass %) thermolyzed at (a) 1000 °C and (b) 1400 °C.

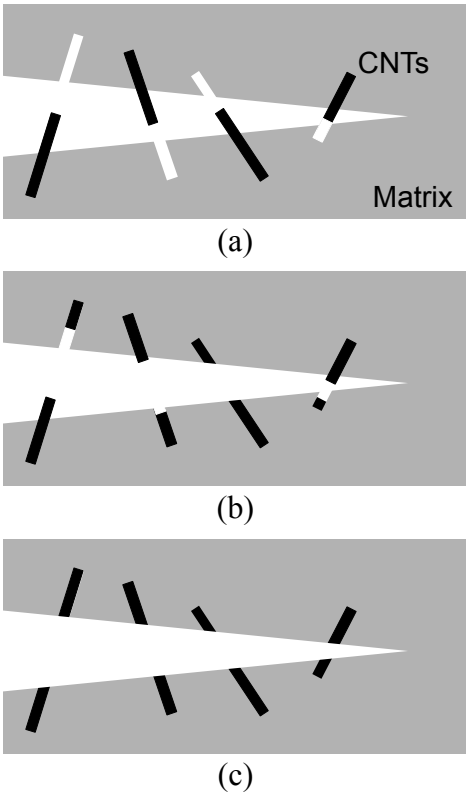


Fig. 4.47. Schematic fracture behaviors of the embedded CNTs in the matrix showing the majority of (a) pulled out CNT, (b) pulled out and broken CNT and (c) broken CNT structure.

### 4.4.7 Young's modulus and hardness

The Young's modulus of the Si-B-C-N materials determined by nanoindentation is shown in Fig 4.48 as a function of the penetration depth of the indent. The pure Si-B-C-N materials with different thermolysis temperatures of 1000 - 1400 °C have Young's modulus of 110 - 130 GPa. In these materials, the difference in the modulus among the inter- and intra-materials is observed to be very small. On the other hand, the modulus of the Si-B-C-N/CNT nanocomposites containing 2 mass % CNTs is between 80 – 105 GPa in all materials which reveals a lowering of the modulus compared to the pure materials. Furthermore, an increase of the deviation as well as a decreasing tendency of the modulus is observed with increasing the thermolysis temperature. Similar tendencies among the materials are observed on the behavior of hardness shown in Fig. 4.49. That is, the hardness of the

Si-B-C-N/CNT nanocomposites (9 – 15 GPa) is smaller than that of the pure materials (16 – 18 GPa), and the hardness decrease with increasing the deviation is also observed with increasing thermolysis temperature. Fig. 4.50 shows the typical SPM images of the indents for the pure Si-B-C-N (a) and the CNTs nanocomposite (b) both thermolyzed at 1000 °C. The corresponding image for the CNTs nanocomposites thermolyzed at 1400 °C is also shown in Fig. 4.51 (a). There can be seen no significant difference between the materials thermolyzed at 1000 °C (Fig. 4.49a and b). However, comparing both CNT incorporated nanocomposites with different thermolysis temperatures (Fig. 4.50b and Fig. 4.51a), the appearance of the domain-like morphology becomes obvious in the nanocomposite thermolyzed at 1400 °C. Fig. 4.51b is the hardness behaviors of these different morphology areas (# 1 and # 2) by the nanoindentation revealing the lower hardness of the dark are (# 2) than the bright one (# 1). From these results, it is clarified that the hardness decrease with increasing thermolysis temperature is caused by the generation of the domain morphology in the matrix. To connect this morphology with the local crystallization behavior observed by TEM analysis (Fig. 4.39), the domain areas are considered to be the crystallized matrix areas of the Si-B-C-N/CNT nanocomposites, where the embedded CNTs accelerate matrix crystallization. It may be that the lowering of the Young's modulus and hardness is caused by the generation of microcracking in the domain areas which is induced by the stress due to the local crystallization effect of CNTs on the matrix. Consequently, to make the best use of CNTs as the reinforcement of Si-B-C-N materials, the crystallization of the Si-B-C-N matrix by CNTs must be avoided.

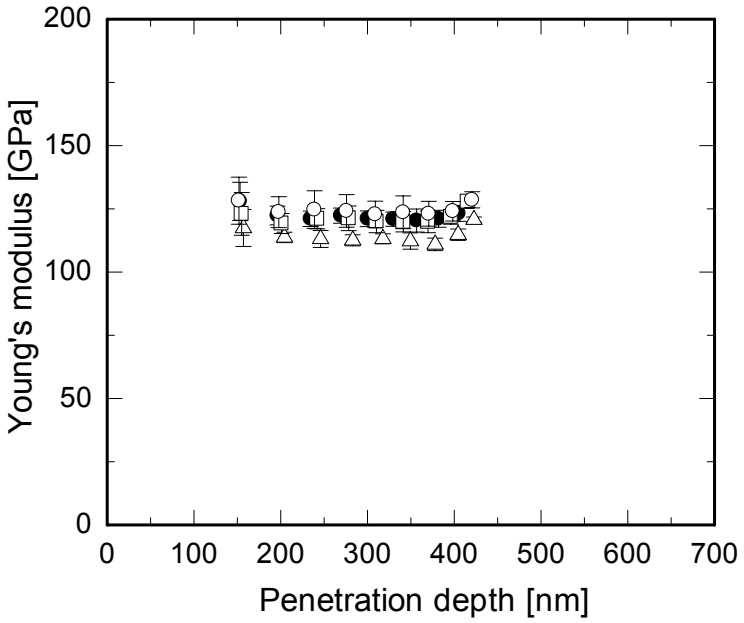


(a)

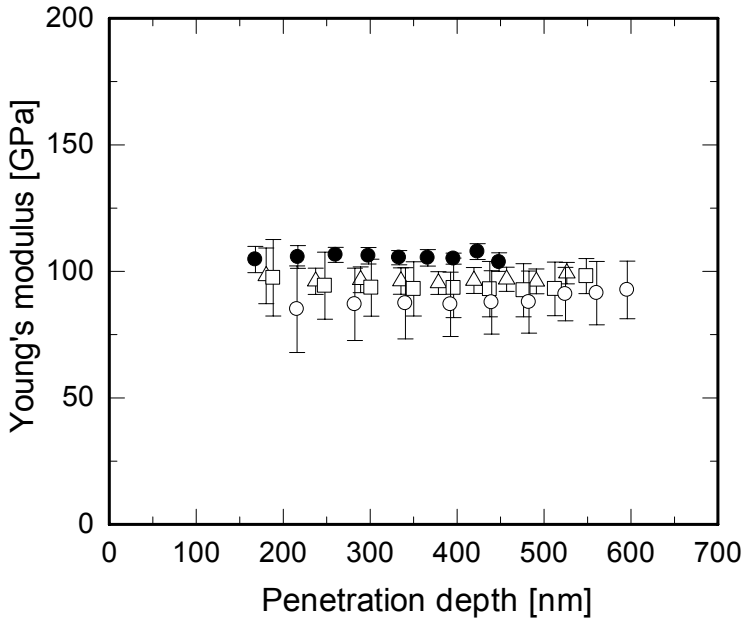


(b)

Fig. 4.48. Young's modulus of the pure Si-B-C-N materials (a) and the Si-B-C-N/CNT nanocomposites (2 mass %) (b) as a function of penetration depth. The thermolysis temperatures are 1000 °C (●), 1200 °C (Δ), 1300 °C (□) and 1400 °C (○).

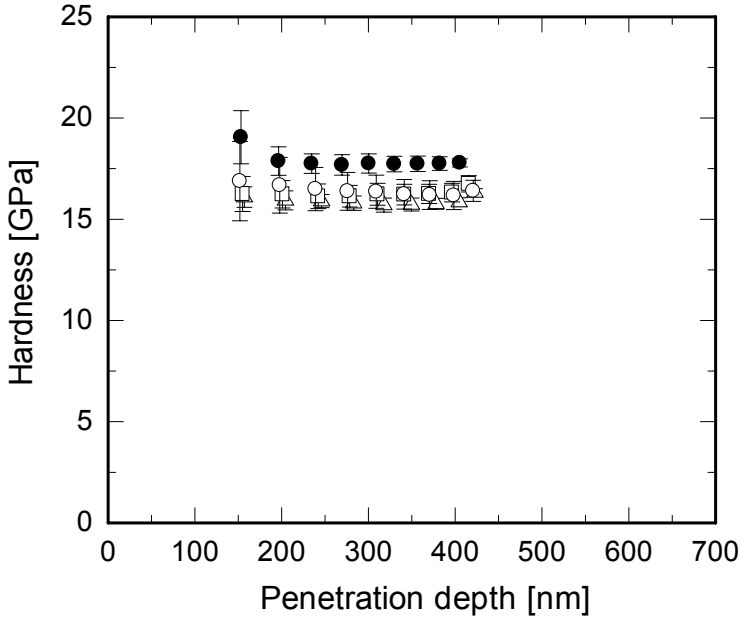


(a)

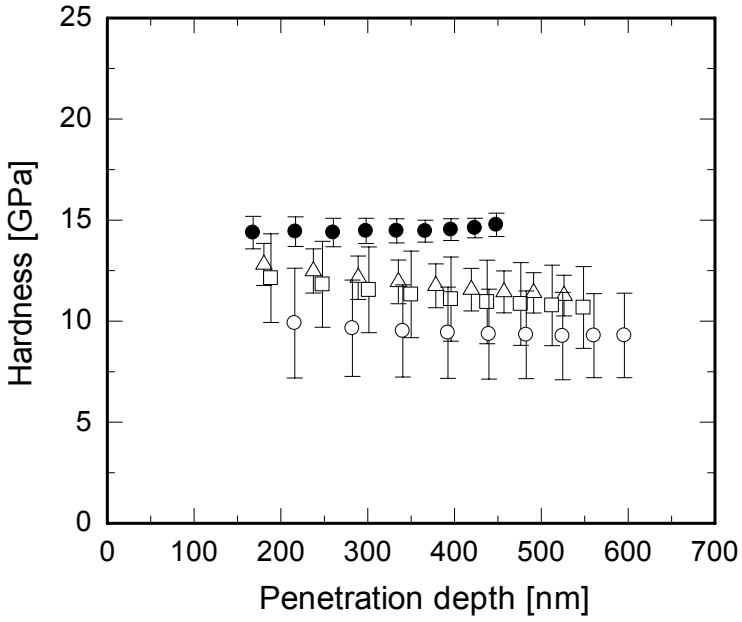


(b)

Fig. 4.49. Hardness of the pure Si-B-C-N materials (a) and the Si-B-C-N/CNT nanocomposites (2 mass %) (b) as a function of penetration depth. The thermolysis temperatures are 1000 °C (●), 1200 °C (Δ), 1300 °C (□) and 1400 °C (○).

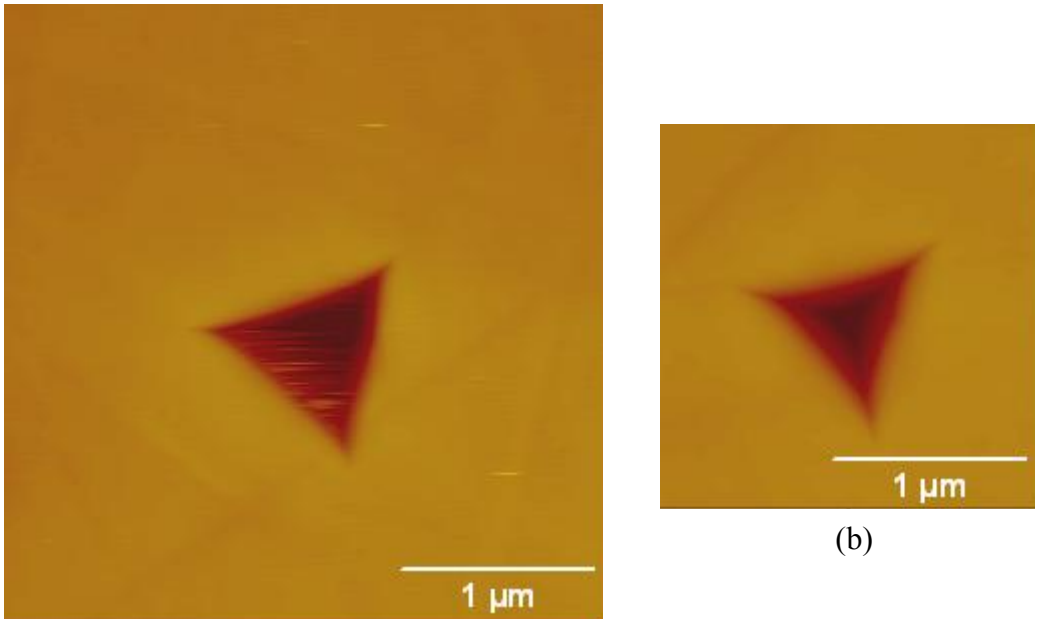


(a) (b)

Fig. 4.50. SPM images of the indent for the pure Si-B-C-N materials (a) and the Si-B-C-N/CNT nanocomposites (2 mass %) both thermolyzed at 1000 °C.

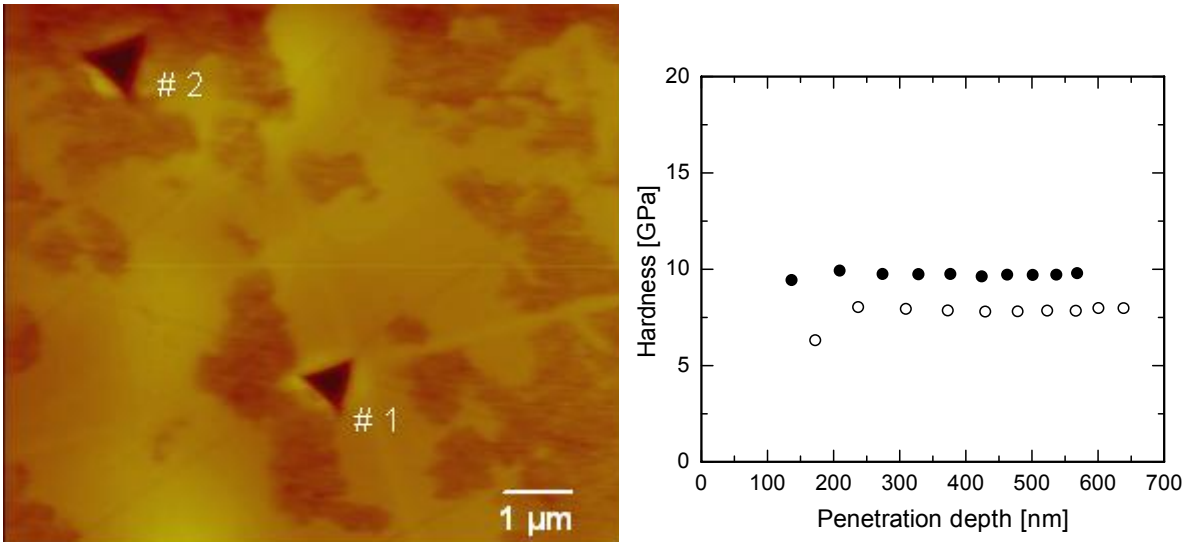


(a) (b)

Fig. 4.51. SPM image of the Si-B-C-N/CNT nanocomposites (2 mass %) thermolyzed at 1400 °C (a), and the corresponding hardness (b) at the positions noted # 1 (●) and # 2 (○).

## 5. Summary and conclusions

Incorporation of CNTs into the precursor derived Si-C-N and Si-B-C-N ceramics and their material properties have been investigated.

Dense Si-C-N/CNT nanocomposites containing different types of CNTs were successfully prepared by casting of a mixture of CNTs and a liquid precursor polymer followed by cross-linking and thermolysis. The mechanical studies by a thermal loading technique reveal remarkable increase in the fracture toughness of the nanocomposites containing one type of MWCNTs, where pulling out, bridging up and breaking of CNTs have been observed at the fracture surfaces. The TEM analyses have demonstrated the preservation of MWCNTs structure in the Si-C-N matrix as well as the existence of well-bonded interface between CNTs and the matrix. On the other hand, the MWCNTs with an amorphous nature provide no effect on the mechanical properties and microstructural view points of the nanocomposites. It is concluded that the CNTs can effectively function as the reinforcement of Si-C-N ceramics, where the thermal stress induced in the nanocomposites is effectively transferred to the CNTs via the matrix/CNT interface. In these architectures, the fracture energy increase leading to the toughening can be generated by the interfacial debonding, CNT pulling out, bridging and breaking as well as the crack deflection and pinning effect at CNTs. The strength and integrity of the CNTs in the matrix and the interfacial bonding between CNTs and the matrix are shown to be critical parameters for the reinforcement.

The incorporation of CNTs into the Si-B-C-N ceramics also induces the pulling out and breaking CNTs at the fracture surfaces, which indicates the toughening effect of CNTs on the Si-B-C-N ceramics similar to Si-C-N/CNT nanocomposites. The enlargement of the interaction between CNTs and the matrix has appeared with increasing thermolysis temperature, where the CNT features are transformed from pulling out to breaking structure at the fracture surfaces. However, on the other side, crystallization of the Si-B-C-N matrix and deterioration of the thermal stability have been disclosed in the Si-B-C-N/CNT nanocomposites. It is considered that CNTs act as templates for the crystallization of the amorphous Si-B-C-N matrix into silicon carbide, which interferes in the formation of characteristic stable structure for the Si-B-C-N ceramics.

## Appendix 1

### Program for calculation of the fracture toughness and stress intensity factor

The coefficients and crack lengths stated below are corresponding to the pure Si-C-N material as an example.

> **restart;**

Input the radius in meters: ***R***

> ***R:= 6e-3*:**

Temperature function, ***T* (*r*) at defined time (*c*=*a*)**, with the fourth order polynomial in Eq. 3.1.

> ***T:= c*$_0$ + *c*$_2$**r^2 + *c*$_4$**r^4;**

$$T := c0 + c2\,r^2 + c4\,r^4$$

Fill in the appropriate Young's modulus, ***E***, in MPa.

> ***E:= 138000*;**

$$E := 138000$$

Temperature dependence of the thermal expansion coefficient.

Fill in the appropriate coefficients, ***m*$_1$, *m*$_2$, *m*$_3$ and *m*$_4$**, of the alpha-Temperature function, **"*alpha* (*T*)"**, shown as in Eq. 4.8:

alpha = $m_1$ + $m_2$*T + $m_3$*T^2 + $m_4$*T^3

> ***m*$_1$:= *4.0653e-7*:**

> ***m*$_2$:= *1.4549e-8*:**

> ***m*$_3$:= *-1.9815e-11*:**

> ***m*$_4$:= *1.8058e-14*:**

Temperature function, ***T***, in Eq. 3.1 is inserted into the alpha function.

> ***alpha*:= *m*$_1$ + *m*$_2$**T + *m*$_3$**T^2 + *m*$_4$**T^3;**

$$\alpha := .40653\,10^{-6} + .14549\,10^{-7}\,c0 + .14549\,10^{-7}\,c2\,r^2 + .14549\,10^{-7}\,c4\,r^4 - .19815\,10^{-10}\,(c0 + c2\,r^2 + c4\,r^4)^2 + .18058\,10^{-13}\,(c0 + c2\,r^2 + c4\,r^4)^3$$

Calculation for the Weight function parameter.

***Beta*** and ***D*$_0$, *D*$_1$, *D*$_2$** parameters in Eq. 3.3 are calculated from Eq. 3.4..

> ***beta*:= *a*/(*2*R*):**

> ***D*$_0$:= (*1.5721 + 2.4109*beta - 0.8968*(beta^2) - 1.4311*(beta^3)*)/((*1 - beta*)^(*3/2*)):**

> ***D*$_1$:= (*0.4612 + 0.5972*beta + 0.7466*(beta^2) + 2.2131*(beta^3)*)/((*1 - beta*)^(*3/2*)):**

> ***D*$_2$:= (*-0.2537 + 0.4353*beta - 0.2851*(beta^2) - 0.5853*(beta^3)*)/((*1 - beta*)^(*3/2*)):**

Weight function, ***h* (*x, a*)**, in Eq. 3.3.

> ***h:= sqrt*(*2/*(*Pi*a*))**((*x/a*)/*sqrt*(*1 - x/a*) + *D*$_0$**sqrt*(*1 - x/a*) + *D*$_1$**(*1 - x/a*)^(*3/2*) + *D*$_2$**(*1 - x/a*)^(*5/2*)):**

Calculation for the stress intensity factor.

***Sigma* (*r*)** in Eq. 3.6 is transfered to ***"sigmar"***.

> ***sigmar:= E*(((1/R^2)*int(alpha*T*r, r=0..R)) + ((1/r^2)*int(alpha*T*r, r=0..r)) - alpha*T):***

Substitution of ***r*** by ***r=R-x*** in ***"sigmar"*** gives ***"sigmax" , Sigma (x),*** in Eq. 3.6.

> ***sigmax := subs(r=R-x, sigmar):***

Calculation of the fracture toughness, ***K***, at ***c=a*** in Eq. 3.6.

> ***K:= int(h*sigmax, x=0..a):***

Fill in the coefficients of the Temperature functions, $c_0$, $c_2$ **and** $c_4$ at each crack length, ***a***, in meters.

***K*** is the corresponding fracture toughness at ***a=c***.

> ***CL01:=subs ($c_0$=186.24245, $c_2$=-5243148.799, $c_4$=99962513507, a=4.275E-03, K);***
> ***CL02:= subs ($c_0$=189.19750, $c_2$=-5264353.060, $c_4$=99056510152, a=4.389E-03, K);***
> ***CL03:= subs ($c_0$=193.80251, $c_2$=-5297852.257, $c_4$=97681244394, a=4.552E-03, K);***
> ***CL04:= subs ($c_0$=199.50754, $c_2$=-5340128.683, $c_4$=96039695328, a=4.710E-03, K);***
> ***CL05:= subs ($c_0$=204.08771, $c_2$=-5374695.274, $c_4$=94772000341, a=4.823E-03, K);***
> ***CL06:= subs ($c_0$=213.04397, $c_2$=-5443915.575, $c_4$=92423424958, a=5.039E-03, K);***
> ***CL07:= subs ($c_0$=218.83854, $c_2$=-5489859.317, $c_4$=90996644012, a=5.216E-03, K);***
> ***CL08:= subs ($c_0$=231.28071, $c_2$=-5591632.436, $c_4$=88182263593, a=5.392E-03, K);***
> ***CL09:= subs ($c_0$=235.45924, $c_2$=-5626778.495, $c_4$=87314164005, a=5.488E-03, K);***
> ***CL10:= subs ($c_0$=246.73467, $c_2$=-5724079.213, $c_4$=85167498133, a=5.656E-03, K);***
> ***CL11:= subs ($c_0$=261.47737, $c_2$=-5856805.794, $c_4$=82797739472, a=5.840E-03, K);***

Followings are the calculated fracture toughness at each crack length.

***CL01 := 1.062828435***
***CL02 := 1.067565747***
***CL03 := 1.072667366***
***CL04 := 1.084075267***
***CL05 := 1.093227081***
***CL06 := 1.102980772***
***CL07 := 1.086979398***
***CL08 := 1.125486559***
***CL09 := 1.118293846***
***CL10 := 1.134585930***
***CL11 :=1.161170235***

## Appendix 2

### Coefficients of the temperature distribution at each voltage and time

(1) Pure Si-C-N material

| Lamp voltage (V) | Time (sec) | $T(r,t)=c_0(t)+c_2(t)r^2+c_4(t)r^4$ | | |
|---|---|---|---|---|
| | | $c_0$ | $c_2$ | $c_4$ |
| 2.2 | 260 | 147.4 | -4.395E+06 | 9.237E+10 |
| 2.4 | 286 | 186.4 | -4.648E+06 | 7.858E+10 |
| 2.6 | 312 | 222.9 | -4.920E+06 | 6.853E+10 |
| 2.8 | 338 | 257.2 | -5.210E+06 | 6.176E+10 |
| 3.0 | 364 | 289.7 | -5.515E+06 | 5.784E+10 |
| 3.2 | 390 | 320.5 | -5.834E+06 | 5.648E+10 |
| 3.4 | 416 | 349.9 | -6.167E+06 | 5.739E+10 |
| 3.6 | 442 | 378.0 | -6.512E+06 | 6.036E+10 |

(2) Si-C-N/MWCNT, type A-1 mass % nanocomposite

| Lamp voltage (V) | Time (sec) | $T(r,t)=c_0(t)+c_2(t)r^2+c_4(t)r^4$ | | |
|---|---|---|---|---|
| | | $c_0$ | $c_2$ | $c_4$ |
| 2.4 | 286 | 182.4 | -1.869E+07 | 3.137E+12 |
| 2.6 | 312 | 209.1 | -4.350E+06 | 4.060E+10 |
| 2.8 | 338 | 242.7 | -5.017E+06 | 5.255E+10 |
| 3.0 | 364 | 275.0 | -5.538E+06 | 5.693E+10 |
| 3.2 | 390 | 306.2 | -6.004E+06 | 5.955E+10 |
| 3.4 | 416 | 336.4 | -6.417E+06 | 6.053E+10 |
| 3.6 | 442 | 365.6 | -6.781E+06 | 6.000E+10 |

(3) Si-C-N/MWCNT, type A-2 mass % nanocomposite

| Lamp voltage (V) | Time (sec) | $T(r,t)=c_0(t)+c_2(t)r^2+c_4(t)r^4$ | | |
|---|---|---|---|---|
| | | $c_0$ | $c_2$ | $c_4$ |
| 2.2 | 260 | 138.8 | -6.232E+06 | 1.279E+11 |
| 2.4 | 286 | 172.3 | -4.844E+06 | 2.099E+10 |
| 2.6 | 312 | 206.7 | -4.740E+06 | 6.458E+10 |
| 2.8 | 338 | 242.7 | -5.040E+06 | 5.266E+10 |
| 3.0 | 364 | 279.0 | -5.595E+06 | 5.070E+10 |
| 3.2 | 390 | 315.7 | -6.381E+06 | 5.771E+10 |
| 3.4 | 416 | 352.7 | -7.377E+06 | 7.288E+10 |
| 3.6 | 442 | 390.1 | -8.569E+06 | 9.550E+10 |

(4) Si-C-N/MWCNT, type B-1 mass % nanocomposite

| Lamp voltage (V) | Time (sec) | $T(r,t)=c_0(t)+c_2(t)r^2+c_4(t)r^4$ | | |
|---|---|---|---|---|
| | | $c_0$ | $c_2$ | $c_4$ |
| 2.4 | 286 | 162.9 | -7.227E+06 | -3.854E+11 |
| 2.6 | 312 | 194.1 | -4.542E+06 | 1.125E+11 |
| 2.8 | 338 | 227.6 | -4.663E+06 | 6.810E+10 |
| 3.0 | 364 | 259.7 | -4.928E+06 | 6.105E+10 |
| 3.2 | 390 | 290.6 | -5.235E+06 | 5.555E+10 |
| 3.4 | 416 | 320.6 | -5.578E+06 | 5.136E+10 |
| 3.6 | 442 | 349.6 | -5.950E+06 | 4.830E+10 |

(5) Si-C-N/MWCNT, type B-2 mass % nanocomposite

| Lamp voltage (V) | Time (sec) | $T(r,t)=c_0(t)+c_2(t)r^2+c_4(t)r^4$ | | |
|---|---|---|---|---|
| | | $c_0$ | $c_2$ | $c_4$ |
| 2.2 | 260 | 126.9 | -3.597E+06 | 6.313E+10 |
| 2.4 | 286 | 167.3 | -4.421E+06 | 7.277E+10 |
| 2.6 | 312 | 205.4 | -5.084E+06 | 7.712E+10 |
| 2.8 | 338 | 241.6 | -5.609E+06 | 7.697E+10 |
| 3.0 | 364 | 276.0 | -6.013E+06 | 7.294E+10 |
| 3.2 | 390 | 308.9 | -6.312E+06 | 6.555E+10 |
| 3.4 | 416 | 340.3 | -6.517E+06 | 5.521E+10 |
| 3.6 | 442 | 370.6 | -6.640E+06 | 4.226E+10 |

(6) Si-C-N/SWCNT, 0.2 mass % nanocomposite

| Lamp voltage (V) | Time (sec) | $T(r,t)=c_0(t)+c_2(t)r^2+c_4(t)r^4$ | | |
|---|---|---|---|---|
| | | $c_0$ | $c_2$ | $c_4$ |
| 2.4 | 286 | 163.1 | -3.549E+06 | -3.628E+12 |
| 2.6 | 312 | 199.7 | -6.914E+06 | 1.714E+11 |
| 2.8 | 338 | 234.9 | -6.947E+06 | 1.128E+11 |
| 3.0 | 364 | 269.1 | -7.372E+06 | 1.014E+11 |
| 3.2 | 390 | 302.6 | -8.025E+06 | 1.093E+11 |
| 3.4 | 416 | 334.8 | -8.545E+06 | 1.123E+11 |
| 3.6 | 442 | 365.8 | -8.943E+06 | 1.108E+11 |

(7) Pure Si-B-C-N material

| Lamp voltage (V) | Time (sec) | $T(r,t) = c_0(t) + c_2(t)r^2 + c_4(t)r^4$ | | |
|---|---|---|---|---|
| | | $c_0$ | $c_2$ | $c_4$ |
| 2.2 | 260 | 174.8 | -1.702E+06 | -7.332E+11 |
| 2.4 | 286 | 220.2 | -7.352E+06 | 1.906E+11 |
| 2.6 | 312 | 259.6 | -7.308E+06 | 1.141E+11 |
| 2.8 | 338 | 297.3 | -7.708E+06 | 9.957E+10 |
| 3.0 | 364 | 333.8 | -8.456E+06 | 1.081E+11 |
| 3.2 | 390 | 369.0 | -9.251E+06 | 1.197E+11 |
| 3.4 | 416 | 402.8 | -1.008E+07 | 1.338E+11 |
| 3.6 | 442 | 435.4 | -1.095E+07 | 1.503E+11 |

(8) Si-B-C-N/MWCNT, type A-2 mass % nanocomposite

| Lamp voltage (V) | Time (sec) | $T(r,t) = c_0(t) + c_2(t)r^2 + c_4(t)r^4$ | | |
|---|---|---|---|---|
| | | $c_0$ | $c_2$ | $c_4$ |
| 2.2 | 260 | 158.9 | -7.932E+06 | 3.166E+12 |
| 2.4 | 286 | 202.1 | -6.470E+06 | 1.617E+11 |
| 2.6 | 312 | 242.0 | -6.692E+06 | 1.079E+11 |
| 2.8 | 338 | 279.8 | -7.076E+06 | 9.166E+10 |
| 3.0 | 364 | 316.1 | -7.760E+06 | 9.852E+10 |
| 3.2 | 390 | 350.8 | -8.424E+06 | 1.068E+11 |
| 3.4 | 416 | 383.9 | -9.067E+06 | 1.162E+11 |
| 3.6 | 442 | 415.7 | -9.692E+06 | 1.267E+11 |

## Appendix 3

### Coefficients of the thermal expansion curve and the *α-T function*

(1) Si-C-N/CNT nanocomposites

| Material CNT type | CNT mass % | $l(T)=h+iT^j$ | | | $\alpha(T)=m_1+m_2T+m_3T^2+m_4T^3$ | | | |
|---|---|---|---|---|---|---|---|---|
| | | $h$ | $i$ | $j$ | $m_1$ | $m_2$ | $m_3$ | $m_4$ |
| Pure | 0 | 10000.23 | 4.9E-04 | 1.659 | 4.065 E-07 | 1.455 E-08 | -1.982 E-11 | 1.806 E-14 |
| MW type A | 1.0 | 10000.24 | 4.3E-04 | 1.681 | 3.683 E-07 | 1.464 E-08 | -1.898 E-11 | 1.719 E-14 |
| MW type A | 2.0 | 10000.17 | 6.3E-04 | 1.620 | 4.873 E-07 | 1.473 E-08 | -2.174 E-11 | 2.008 E-14 |
| MW type B | 1.0 | 10000.41 | 4.3E-04 | 1.669 | 3.625 E-07 | 1.359 E-08 | -1.809 E-11 | 1.644 E-14 |
| MW type B | 2.0 | 10000.37 | 3.2E-04 | 1.726 | 2.879 E-07 | 1.422 E-08 | -1.642 E-11 | 1.465 E-14 |

(2) Si-B-C-N/CNT nanocomposites

| Material CNT type | CNT mass % | $l(T)=h+iT^j$ | | | $\alpha(T)=m_1+m_2T+m_3T^2+m_4T^3$ | | | |
|---|---|---|---|---|---|---|---|---|
| | | $h$ | $i$ | $j$ | $m_1$ | $m_2$ | $m_3$ | $m_4$ |
| Pure | 0 | 10000.21 | 2.8E-04 | 1.722 | 2.515 E-07 | 1.212 E-08 | -1.413 E-11 | 1.262 E-14 |
| MW type A | 2.0 | 10000.29 | 2.0E-04 | 1.769 | 1.837 E-07 | 1.137 E-08 | -1.146 E-11 | 1.007 E-14 |

## References


[Imc] ASTM C1259-98. Standard Test Method for Dynamic Young's Modulus, Shear Modulus and Poisson's Ratio for Advanced Ceramics by Impulse Excitation of Vibration.

[KiON] KiON, KiONTM VL20 and CERASETTM SN liquid polysilazanes. Technical bulletins, KiON cooperation. http://www.ceraset.com/bulletins/ceramic.html

[Roc] Rochefort, A., Nanotechnology now., http://www.nanotech-now.com/nanotube-buckyball-sites.htm

[Sma] Smalley, R. E., Image gallery of Smalley group at Rice University., http://cohesion.rice.edu/naturalsciences/smalley/emplibrary/ropes_5.jpg

[70Bru] Brueckner, H., A novel principle for the computation of stress intensity factors., ZAMM 1970, 50, 529-546

[73Roo] Rooke, D. P. and Tweed, J., The stress intensity factors of a radial crack in a finite rotation disc., Int. J. Engng. Sci., 1973, 11, 279-283

[76Kin] Kingery, W. D., Bowen, H. K. and Uhlmann, D. R., Introduction to Ceramics, 2nd Edition., John Wiley and Sons., 1976, 584

[85Bol] Boley, B. A. and Weiner, J. H., Theory of thermal stresses., R. E. Krieger, Malabar, FL, 1985, 288-291

[89Gre] Gregory, R. D., The spinning circular disc with a radial edge crack; an exact solution., Int. J. Fracture, 1989, 41, 39-50

[89Sch] Schneider G. A. and Danzer R., Calculation of the stress intensity factor of an edge crack in a finite elastic disc using the weight function method., Fracture Mechanics, 1989, 34, 547-552

[90Peu] Peuckert, M., Vaahs, T. and Brück, M., Ceramics from organometallic polymers., Adv. Mater., 1990, 2, 398-404

[91Iij] Iijima, S., Helical microtubules of graphitic carbon., Nature, 1991, 354, 56-58

[91Sch] Schneider, G. A. and Petzow G., Thermal shock testing of ceramics-A new testing method., J. Am. Ceram. Soc., 1991, 74, 98-102

[92Ham] Hamada, N., Sawada, S. and Oshima, A., New one-dimensional conductors: Graphite microtubules., Phys. Rev. Lett. 1992, 68, 1579-1581

[92Min] Mintmire, J.W., Dunlap, B. I. and White, C. T., Are fullerene tubules

metallic?, Phys. Rev. Lett. 1992, 68, 631-6341

[92Sai] Saito, R., Fujita, M., Dresselhaus, G. and Dresselhaus, M. S., Electric structure of chiral graphene tubules., Appl. Phys. Lett. 1992, 60, 2204-22061

[93Mar] Margerl, F., Schneider, G. A. and Petzow G., Crack initiation and crack groth in ceramics under thermal loading., Adv. Mater. 1993, I / A : Ceramics, powders, corrosion and advanced processing, 395-399

[93Yac] Yacaman, M.J., Yoshida, M.M., Rendon, L. and Santiesteban, J.G., Catalytic growth of carbon microtubules with fullerene structure., Appl. Phys. Lett., 1993, 62, 202

[95Bil] Bill J. and Aldinger, F., Precursor-derived cova1ent ceramics., Adv. Mater. 1995, 7, 775-787

[95Bir] Birot, M., Pilot, JP. and Dunogues, J., Comprehensive chemistry of polycarbosilanes, polysilazanes, and polycarbosilazanes as precursors of ceramics., Chem. Rev., 1995, 95, 1443-1477

[95Deh] Deheer W. A., Bacsa W. S., Chatelain, A., Gerfin, T., Humphreybaker, R., Forro, L. and Ugarte, D., Aligned carbon nanotube films-production and optical and electronic properties., Science, 1995, 268, 845-847

[95Rie] Riedel, R., Kleebe, H.-J., Schoenfelder, H. and Aldinger, F., A covalent micro/nano-comosite resistant to high-temperature oxidation., Nature, 1995, 374, 526-528

[96Bil] Bill, J. and Heimann, D., Polymer-derived ceramic coating on C/C-SiC composites., J. Euro. Ceram. Soc., 1996, 16, 1115-1120

[96Dre] Dresselhaus, M. S., Dresselhaus, G. and Eklund, P. C., Science of fullerenes and carbon nanotubes., Academic Press. New York., 1996

[96Jal] Jalowiecki, A., Bill, J., Aldinger, F. and Mayer, J., Interface characterization of nanosized b-doped $Si_3N_4$/SiC ceramics., Composites Part A., 1996, 27A, 717-721

[96Nar] Narula, C. K., Allison, J. E., Bauer, D. R.and Gandhi, H. S., Materials chemistry issues related to advanced materials applications in the automotive industry., Chem. Mater., 1996, 8, 984-1003

[96Rie] Rie, R., Kienzlem, A., Dressler, W., Ruwisch, L., Bill J. and Aldinger F., A silicoboron carbonitride ceramic stable to 2000 $^{o}$C., Nature, 1996, 382, 796-798

[96The] Thess, A., Lee, R., Nikolaev, P., Dai, H., Petit, P., Robert, J., Xu, C., Lee, Y. H., Kim, S. G., Rinzler, A. G., Colbert, D. T., Scuseria, G. E., Tomanek, D., Fischer, J. E. and Smalley, R. E., Crystalline Ropes of Metallic Carbon Nanotubes., Science, 1996, 273, 483-487

[96Tre] Treacy, M. M. J., Ebbesen, T. W. and Gibson, J. M., Exceptionally high Young's modulus observed for individual carbon nanotubes., Nature, 1996, 381, 678-683

[97Dil] Dillon, A. C., Jones, K.M., Bekkendahl, T. A., Kiang, C. H., Bethune, D. S. and Heben, M. J., Storage of hydrogen in singlewalled carbon nanotubes., Nature, 1997, 386, 377-379

[97Fet] Fett, T. and Munz, D., Stress intensity factors and weight functions., Computational Mechanics Publications, Southampton, 1997, pp. 149-153

[98Cha] Chawla, K. K., Composite materials., Springer-Verlag New York, Unc. 1998, 212-251

[98Gao] Gao, G., Cagin, T. and Goddard III, W. A., Energetics, structure, mechanical and vibrational properties of carbon nanotubes and nanofibers., Nanotechnology, 1998, 9, 184-191

[98Kam] Kamphowe, T. W., Weinmann, M., Bill, J. and Aldinger, F., Preparation of fibre-reinforced Si-B-C-N ceramics by polymer precursor infiltration., Silic. Ind. 1998, 63, 159-162

[98Kri] Krishnan, A., Dujardin, E., Ebbesen, T.W., Yianilos, P.N. and Treacy, M.M.J., Young's modulus of single-walled nanotubes., Phys. Rev. B 1998, 58, 14013-14019

[98Kuz] Kuzumaki, T., Miyazawa, K., Ichinose, H. and Ito, K., Processing carbon nanotube reinforced aluminum composite., J. Mater. Res., 1998, 13, 2445-2449

[98Lou] Lourie, O.and Wagner, H. D., Evaluation of Young's modulus of carbon nanotubes by micro-raman spectroscopy., J. Mater. Res., 1998, 13, 2418-2422

[98Lu] Lu, J. P. and Han, J., Carbon nanotubes and nanotubes-based nano devices., Int. J. High Speed Electron. Sys. 1998, 9, 101-123

[98Ma] Ma, R. Z., Wu, J., Wei, B. Q., Liang, J. and Wu, D. H., Processing and properties of carbon nanotubes-nano-SiC ceramic., J. Mater. Sci., 1998, 33, 5243-5246

[98Pei] Peigney, A., Laurent, Ch., Dumortier, O., and Rousset, A., Carbon nanotubes–Fe–alumina nanocomposites., Part I: influence of the Fe content on the synthesis of powders. J. Euro. Ceram. Soc., 1998, 18, 1995-2004

[98Wag] Wagner, H. D., Lourie, O., Feldman, Y. and Tenne, R., Stress-induced fragmentation of multiwall carbon nanotubes in a polymer matrix., Appl. Phys. Lett., 1998, 72, 188-190

[99Bal] Baldus, P., Jansen, M. and Sporn, D., Ceramic fiber for matrix composites in high-temperature engine applications., Science. 1999, 285, 699-703

[99Cho] Choi, W. B., Chung, D. S., Kang, J. H., Kim, H. Y., Jin, Y. W., Han, I. T., Lee, Y. H., Jung, J. E., Lee, N. S., Park, G. S. and Kim, J. M., Fully sealed, high-brightness carbon-nanotube field-emission display., Appl. Phys. Lett. 1999, 75, 3129-3131

[99Hon] Hone, J., Whitney, M. and Zettl, A., Thermal conductivity of single-walled carbon nanotubes., Synthetic Metals 1999, 103, 2498-2499

[99San] Sandler, J.K.W., Shaffer, M.S.P., Prasse, T., Bauhofer, W., Schulte, K. and Windle, A.H., Development of a dispersion process for carbon nanotubes in an epoxy matrix and the resulting electrical properties., Polymer 1999, 40, 5967-5971

[99Sei] Seifert, H. J., Reaction path simulations in multicomponent materials., Z metallkd., 1999, 90, 1016-1024

[99Thu] Thurn, G., Canel, J., Bill, J. and Aldinger, F., Compression creep behaviour of precursor-derived Si-C-N ceramics., J. Euro. Ceram. Soc., 1999, 19, 2317-2323

[99Yi] Yi, W., Lu, L.,Zhang, D.-L., Pan, Z. W.and Xie, S. S., Linear specific heat of carbon nanotubes., Phys. Rev., 1999, B 59, R9015–9018

[99Zie] Ziegler, G., Richter, I. and Suttor, D., Fiber-reinforrced composites with polymer-derived matrix: processing, matrix formation and properties., Composites Part A., 1999, 30, 411-417

[00Ber] Berber, S., Kwon, Y-K. and Tomanek, D., Unusually high thermal conductivity of carbon nanotubes., Phys. Rev. Lett. 2000, 84, 4613-4616

[00Fla] Flahaut, E., Peigny, A., Laurent, Ch., Marliere, Ch., Chastel, F. and Rousset, A., Cabon nanotube-metal-oxide nanocomposites: Microstructure, electrical conductivity and mechanical properties., Acta mater., 2000, 48,

3803-3812

[00Kon] Kong, J., Franklin, N. R., Zhou, C., Chapline, M. G., Peng, S., Cho, K. and Dai, H., Nanotube molecular wires as chemical sensors., Science, 2000, 287, 622-625

[00Kro] Kroke, E., Li, Y.-L., Konetschny, C., Lecome, F., Fasel, C. and Riedel, R., Silazane derived ceramics and related materials., Mater. Sci. Eng., 2000, 26, 97-199

[00Pei] Peigney, A., Laurent, Ch., Flahaut, E. and Rousset. A., Carbon nanotubes in novel ceramic matrix nanocomposites., Ceramics International, 2000, 26, 677-683

[00Qia] Qian, D., Dickey, E. C., Andrews, R. and Rantell, T., Load transfer and deformation mechanisms in carbon nanotube-polystyrene composites., Appl. Phys. Lett. 2000, 76, 2868-2870

[00Ril] Riley, F., Silicon nitride and related materials., J. Am. Ceram. Soc., 2000, 83, 245–65

[00Wei] Weinmann, M., Kamphowe, T. W., Schuhmacher, J., Mueller, K. and Aldinger, F., Design of polymeric Si-B-C-N ceramic precursors for application in fiber-reinforced composite materials., Chem. Mater., 2000, 12, 2112-2122

[00Yu1] Yu, M-F., Files, B.S., Arepalli, S. and Ruoff, R.S., Tensile loading of ropes of single wall carbon nanotubes and their mechanical properties., Phys. Rev. Lett. 2000, 84, 5552-5555

[00Yu2] Yu, M-F., Lourie, O., Dyer, M. J., Moloni, K., Kelly, T. F. and Ruoff. R. S., Strength and breaking mechanism of multiwalled carbon nanotubes under tensile load., Science, 2000, 287, 637-640

[01Bac] Bachtold, A., Hadley, P., Nakanishi, T.and Dekker, C., Logic circuits with carbon nanotube transistors., Science, 2001, 294, 1317-1320

[01Bil] Bill J., Kamphowe, T. W., Mueller, A., Wichmann, T., Zern, A., Jalowieki, A., Mayer, J., Weinmann, M., Schuhmacher, J., Mueller, K., Peng, J., Seifert, H. J. and Aldinger, F., Precursor-derived Si-(B-)C-N ceramics: thermolysis, amorphous state and crystallization., Appl. Organomet. Chem. 2001, 15, 777-793

[01But] Butchereit, E., Nickel, K. G. and Mueller, A., Precursor-derived Si-B-C-N ceramics: Oxidation kinetics., J. Am. Ceram. Soc., 2001, 84, 2184-2188

[01Cze] Czerw, R., Guo, Z., Ajayan, P. M., Sun, Y.-P., Carroll, D. L., Organization of polymers onto carbon nanotubes: A route to nanoscale assembly., Nano Lett., 2001, 1, 423-427.

[01Li] Li, Y-L., Kroke, E., Riedel, R., Fasel, C., Gervais, C. and Babonneau, F., Thermal cross-linking and pyrolytic conversion of poly(ureamethylvinyl)silazane to silicon-based ceramics., Appl. Organometal. Chem., 2001, 15, 820-832

[01Raj1] Raj, R., An, L. and Shah, S., Oxidation kinetics of an amorphous silicon carbonitride ceramics., J. Am. Ceram. Soc., 2001, 84, 1803-1810

[01Raj2] Raj, R. Ceramic MEMS. New materials, innovative processing and future applications., Am. Ceram. Soc. Bull., 2001, 80, 25-30

[01Sei] Seifert, H. J., Peng, J., Lukas, H. L.and Aldinger, F., Phase equilibria and thermal analysis of Si–C–N ceramics., J. Alloys and Compounds., 2001, 320, 251-261

[01Sha] Shah, S. R. and Raj, R., Nanoscale densification creep in polymer-derived silicon carbonitrides at 1350 °C., J. Am. Ceram. Soc., 2001, 84, 2208-2212

[01Sie] Siegel, R. W., Chang, S. K., Ash, B. J., Stone, J., Ajayan, P. M., Doremus, R. W. and Schadler, L. S., Mechanical behavior of polymer and ceramic matrix nanocomposites., Scripta mater., 2001, 44, 2061–2064

[02Bie] Biercuk, M. J., Llaguno, M. C., Radosavljevic, M., Hyun, J. K. and Johnson, A. T., Carbon nanotubecomposites for thermal management., Appl. Phys. Lett. 2002, 80, 2767-2769

[02Bie] Biercuk, M. J., Llaguno, M. C., Radosavljevic, M., Hyun, J. K., Johnson, A. T. and Fischer, J. E., Carbon nanotube composites for thermal management., Appl. Phys. Lett., 2002, 80, 2767-2769

[02Jan] Jansen, M., Jaeschke, B. and Jaeschke, T., Amorphous multinary ceramics in the Si-B-N-C system., Structure and Bonding, 2002, 101, 137-220

[02Jon] Jonge, N. D., Lamy, Y., Schoots, K. and Oosterkamp, T. H., High brightness electron beam from a multi-walled carbon nanotube., Nature, 2002, 420, 393-395

[02Kin] King, A. G., Ceramic technology and processing., Noyes Publications, New York. 2002, 406-410

[02Lau] Lau, K. T. and Hui, D., Effectiveness of using carbon nanotubes as nano-reinforcements for advanced composite structures., Carbon, 2002, 40,

1597-1617

[02Lie] Liew, L.-A., Liu, Y., Luo, R., Cross, T., An, L., Bright, V. M., Dunn, M. L., Daily, W. and Raj, R., Fabrication of SiCN MEMS by photopolymerization of pre-ceramic polymer., Sensors and Actuators. A., 2002, 95, 120-134

[02Pet] Petzow, G. and Herrmann, M., Silicon nitride ceramics., Structure and Bonding, 2002, 102, 47-167

[02See] Seeger, T., Köhler, T.H., Frauenheim, T. H., Grobert, N., Rühle, M., Terrones, M. and Seifert, G., Nanotube composites: novel $SiO_2$ coated carbon nanotubes., Chem. Commun., 2002, 34–35

[02Sei] Seifert, H. J. and Aldinger, F., Phase Equilibria in the Si-B-C-N System., Struct. Bond., 2002, 101, 1-58

[02Zim] Zimmermann, A., Bauer, A., Christ, M., Cai, Y. and Aldinger, F., High-temperature deformation of amorphous Si-C-N and Si-B-C-N ceramics derived from polymers., Acta. Meter., 2002, 50, 1187-1196

[03Che] Chen, W. X., Tu, J. P., Wang, L. Y., Gan, H. Y., Xu, Z. D. and Zhang, X. B., Tribological application of carbon nanotubes in a metal based composite coating and composites., Carbon, 2003, 41, 215-222

[03Cho] Choi, E. S., Brooks, J. S., Eaton, D. L., Al-Haik, M. S., Hussaini, M. Y., Garmestani, H., Li, D. and Dahmen, K., Enhancement of thermal and electrical properties of carbon nanotube polymer composites by magnetic field processing., J. Appl. Phys., 2003, 94, 6034-6039

[03Emm] Emmenegger, Ch., Mauron, Ph., Sudan, P., Wenger, P., Hermann, V., Gallay, R. and Zuettel, A., Investigation of electochamical double-layer (ECDL) capacitors electrodes based on carbon nanotubes and activated carbon materials., J. Power Sources, 2003, 124, 321-329

[03Lie] Liew, L.-A., Bright, V. M. and Raj, R., A novel micro glow plug fabricated from polymer-derived ceramics: in situ measurement of high-temperature properties and application to ultrahigh-temperature ignition., Sensors and Actuators A, 2003, 104, 246-262

[03Qi] Qi, P., Vermesh, O., Grecu, M., Javey, A., Wang, Q., Dai, H., Peng, S. and Cho, K., Toward large arrays of multiplex functionalized carbon nanotube sensors for highly sensitive and selective molecular detection., Nano Lett., 2003, 3, 347-351

[03San] Sandler, J.K.W., Kirk, J.E.,Kinloch, I.A., Shaffer, M.S.P. and Windle, A.H.,

Ultra-low electrical percolation threshold in carbon-nanotube-epoxy composites., Polymer, 2003, 44, 5893-5899

[03Val] Valentinia, L., Biagiottia, J., Kenny, J. M.and Santucci, S., Morphological characterization of single-walled carbon nanotubes-PP composites., Composites Science and Technology, 2003, 63, 1149–1153

[03Zha] Zhan, G. D., Kuntz, J. D., Wan, J., and Mukherjee, A. K., Single-wall carbon nanotubes as attractive toughening agents in alumina-based nanocomposites., Nature materials, 2003, 2, 38-42

[04An] An, L., Xu, W., Rajagopalan, S., Wang, C., Wang, H., Fan, Y., Zhang, L., Jiang, D., Kapat, J., Chow, L., Guo, B., Liang, J. and Vaidyanathan, R., Carbon-nanotube-reinforced polymer-derived ceramic composites., Adv. Mater., 2004, 16, 2036-2040

[04Bha] Bharadwaj, L., Fan, Y., Zhang, L., Jiang, D. and An, L., Oxidation behavior of a fully dense polymer-derived amorphous silicon carbide ceramic., J. Am. Ceram. Soc., 2004, 87, 483-486

[04Goj] Gojny, F. H., Wichmann, M. H. G., Koepke, U., Fieldler, B. and Schulte, K., Carbon nanotubes-reinforced epoxy-composites: enhanced stiffness and fracture toughness at low nanotubes content., Compos. Sci. Technol., 2004, 64, 2363-2371

[04Gra] Graham, A. P., Duesberg, G. S., Seidel, R., Liebau, M., Unger, E., Kreupl, F. and Hoenlein, W., Towards the integration of carbon nanotubes in microelectronics., Diamond Relat. Mater., 2004, 13, 1296-1300

[04Kum] Ravi Kumar, N. V., Mager, R., Cai, Y., Zimmermann, A. and Aldinger, F., High temperature deformation behaviour of crystallized Si-B-C-N ceramics obtained from a boron modified poly(vinyl)silazane polymeric precursor., Scripta Materialia., 2004, 51, 65-69

[04Kus] Kusunose T., Sung, R. J., Sekino, T., Sakaguchi, S. and Niihara, K., High-temperature properties of a silicon nitride/boron nitride nanocomposite., J. Mater. Res., 2004, 19, 1432-1438

[04Li1] Li, S.H., Li, Z. N., Yang, M. B., Hu, Z. Q., Xu, X. B. and Huang, R., Carbon nanotubes induced nonisothermal crystallization of ethylene–vinyl acetate copolymer., Materials Letters, 2004, 58, 3967-3970

[04Li2] Li, F., Wang, Y., Wang, D. and Wei, F., Characterization of single-wall carbon nanotubes by $N_2$ adsorption., Carbon, 2004, 42, 2375-2383

[04Lup] Lupo, F., Kamalakaran, R., Scheu, C., Grobert, N. and Ruehle, M., Microstructural investigations on zirconium oxide-carbon nanotube composites synthesized by hydrothermal crystallization., Carbon, 2004, 42, 1995-1999

[04Pro] Probst, O., Moore, E. M., Resasco D. E. and Grady B. P., Nucleation of polyvinyl alcohol crystallization by single-walled carbon nanotubes., Polymer, 2004, 45, 4437–4443

[04Sch] Schnurre, S. M., Groebner, J. and Schmid-Fetzer, R., Thermodynamics and phase stability in the Si-O system., J. Non-Cryst. Solids, 2004, 236, 1-25

[04Schm] Schmit, H., Borchardt, G., Mueller, A. and Bill, J., Formation kinetics of crystalline $Si_3N_4$/SiC composites from amorphous Si-C-N ceramics., J. Non-Crystal. Solids, 2004, 341, 133-140

[05Hua] Huang, Q., Gao, L., Liu, Y. Q. and Sun, J., Sintering and thermal properties of multiwalled carbon nanotube-$BaTiO_3$ composites., J. Mater. Chem., 2005, 15, 1995-2001

[05Nar] Narayanan, J., Deformation and fracture mechanical properties of precursor-derived Si-C-N ceramics., Ph.D. Thesis, University of Stuttgart, Stuttgart, 2005 (to be submitted)

[05Sun] Sun, Y., Miyasato, T., Kirimoto, K. and Kusunoki, M., Metallic-nonmetallic transition on the conductivity temperature dependence of multiwall carbon nanotubes., Appl. Phys. Lett., 2005, 86, 223108

## Zusammenfassung

Si-(B-)C-N-Keramiken, die durch die Thermolyse von präkeramischen Polymeren erzeugt werden, weisen eine bemerkenswerte Hochtemperatur-, Korrosions- und Kriechbeständigkeit auf. Die Beständigkeit dieser Precursorkeramiken basiert grundsätzlich auf deren kovalentem Charakter und der hohen Reinheit dieser Materialien, welche keine Sinteradditive enthalten. Der amorphe und dadurch bedingte spröde Charakter dieser Werkstoffe führt jedoch auch zu einer Verschlechterung der mechanischen Eigenschaften, insbesondere der Bruchzähigkeit. Ein Ansatz zur Verstärkung von spröden Keramiken ist die Einlagerung von zusätzlichen Phasen bzw. die Erzeugung von Verbundwerkstoffen. In diesem Zusammenhang bietet sich der Einbau von Kohlenstoff-Nanoröhrchen an, da diese eine enorme mechanische Festigkeit sowie ein hohes Länge/Durchmesser-Verhältnis besitzen.

In dieser Arbeit wurden Kohlenstoff-Nanoröhrchen (carbon nanotubes, CNTs) im Hinblick auf deren Eignung zur Verstärkung von Si-(B-)C-N-Precursorkeramiken untersucht. Eingesetzt wurden sowohl Nanoröhrchen vom Typ „multi-wall“ (MW) als auch „single-wall“ (SW). Dabei wurden insbesondere die mechanischen Eigenschaften in Verbindung mit den vorliegenden Gefügen der Si-(B-)C-N/CNT-Verbundmaterialien behandelt. Außerdem war die thermische Stabilität und das Kristallisationsverhalten Gegenstand der Arbeiten. Zur strukturellen Charakterisierung der Materialien wurden vor allem die Rasterelektronenmikroskopie (REM) und die Transmissionselektronenmikropie (TEM) herangezogen.

Dichte Si-C-N/CNT-Nanocomposite mit einem Gehalt von 0 – 2 Masse% an CNTs wurden erfolgreich durch Gießen einer Mischung aus Nanoröhrchen und dem Precursor Ceraset TM sowie anschließender Vernetzung (360 °C, 6h) und Thermolyse (1000 °C, 1h) erzeugt. Es zeigte sich, dass eine Ultraschallbehandlung der Nanoröhrchen in einem Lösungsmittel sowie eine niedrige Heizrate bei der anschließenden Thermolyse im Hinblick auf eine Erzeugung von dichten und rissfreien Verbunden mit einer homogenen Verteilung der Nanoröhrchen wesentliche Größen darstellen. Diese Prozesse ermöglichen prinzipiell eine endkonturnahe

Herstellung von Si-C-N/CNT-Formteilen mit kleinen und komplexen Geometrien. Die Untersuchung der mechanischen Eigenschaften dieser Nanocomposite mittels einer Thermoschockmethode zeigte, dass die Bruchzähigkeit von der Art der zur Verstärkung eingesetzten MWCNTs abhängt. So konnte die Bruchzähigkeit bereits bei einer Zugabe von lediglich 2 Masse% an Nanoröhrchen in einem Fall im Vergleich zur reinen Precursorkeramik um 70 % gesteigert werden. Dagegen zeigte ein zweiter eingesetzter MWCNT-Typ keinen Effekt dieser Art. Im Falle der Materialien mit verbesserten Eigenschaften ergibt sich aus rasterelektronenmikroskopische Aufnahmen, dass hierzu verschiedene Mechanismen („pull-out-Effekt“, Überbrückung sowie das Brechen der Röhrchen) beitragen. Weitere Untersuchungen mittels der Transmissionselektronenmikroskopie zeigen außerdem den Erhalt der typischen Struktur der Nanoröhrchen und das Vorliegen einer definierten CNT/Matrix-Grenzfläche. Im Falle der Nanoröhrchen, durch welche die mechanischen Eigenschaften nicht beeinflusst werden, liegt dagegen eine sehr starke CNT/Matrix-Wechselwirkung vor. Zudem weisen diese Röhrchen eine amorphe Struktur auf, so dass weder die oben beschriebenen Effekte noch verbesserte mechanische Eigenschaften beobachtet werden. Aus diesen Untersuchungen geht somit hervor, dass der Einbau der Nanoröhrchen in die Matrix und die CNT/Matrix-Wechselwirkung wesentliche Parameter in Bezug auf die mechanische Verstärkung der Materialien darstellen.

Im Falle der Herstellung von Si-B-C-N/CNT-Verbundmaterialien zeigte sich, dass deren Herstellung über den oben beschrieben Gießprozess nicht möglich ist. Es konnten aufgrund der Sprödigkeit der vernetzten Si-B-C-N-Precursoren sowie wegen deren starken Haftung an der Wand der Gießformen keine stabilen Formteile erhalten werden. Eine alternative Erzeugung über Warmpressen liefert jedoch Materialien, die Bruchflächen aufweisen, welche denen der oben beschriebenen Si-C-N/CNT-Verbundmaterialien mit verbesserten mechanischen Eigenschaften ähneln, was auf einen Verstärkungseffekt der Nanoröhrchen auch im Falle der Si-B-C-N-Precursorkeramiken hinweist. Die Verstärkung der Wechselwirkung zwischen den Nanoröhrchen und der Matrix mit steigender Auslagerungstemperatur die mit einem Übergang von pull-out-Strukturen zum Brechen der Nanoröhrchen verbunden ist, bietet prinzipiell die Möglichkeit, die für die Verstärkung erforderliche optimale Thermolysetemperatur zu bestimmen. Die Erhöhung der

Thermolysetemperatur geht jedoch mit einer zunehmenden thermischen Zersetzung sowie der Kristallisation der Materialien einher, was diese Möglichkeit zur Erhöhung der Zähigkeit wiederum eingeschränkt. Dabei ergibt sich aus Untersuchungen mittels der Röntgendiffraktometrie und der Transmissionselektronenmikroskopie, dass die Nanoröhrchen als Template für die Kristallisation unter Bildung von Siliciumcarbid wirken.

**Curriculum vitae**

Personal information

| | |
|---|---|
| Name: | Yuji KATSUDA |
| Date of Birth: | November 16, 1967 |
| Place of birth: | Kakamigahara, Japan |
| Nationality: | Japanese |
| Marital Status: | Married, two children |

Education

08.2002 - 10.2005:

Ph. D. work at the Max-Planck-Institut für Metallforschung and Institut für Nichtmetallische Anorganische Materialien, Pulvermetallurgisches Laboratorium, Universität Stuttgart

(Financed by NGK Insulators, Ltd., Japan)

04.1990 - 03.1992:

Master of Engineering, Mar. 1992 at Hokkaido University, Hokkaido, Japan

Major: Applied chemistry

Master thesis: Study on the phase transition of inorganic salts monitored by acoustic emission

04.1986 - 03.1990:

Bachelor of Engineering, Mar. 1990 at Hokkaido University, Hokkaido, Japan

Major: Applied chemistry

Work Experience

04.1992 - present:

Materials researcher,

Materials research laboratory, NGK Insulators, Ltd., JAPAN

R&D of the followings;

04.1996 - 08.2002: Aluminum nitride and silicon nitride ceramics for semiconductor producing equipments

04.1994 - 03.1996: Metal oxide semiconductor for gas sensors

04.1992 - 03.1994: Sodium-ß alumina for Na-S battery